

**Assessment of Linear Inverse Problems  
in Magnetocardiography and Lorentz Force  
Eddy Current Testing**

**Dissertation  
Zur Erlangung des akademischen Grades**

**Doktoringenieur  
(Dr.-Ing.)**

**vorgelegt der  
Fakultät für Informatik und Automatisierung der  
Technischen Universität Ilmenau**

**von Dipl.-Ing. Bojana Petković  
geboren am 27.08.1977 in Niš, Serbien**

**Gutachter:     1. Prof. Dr.-Ing. habil. Jens Haueisen  
                  2. Prof. Dr.-Ing. habil. Hannes Töpfer  
                  3. Prof. Dr. Luca Di Rienzo**

**Tag der Einreichung: 06.05.2013**

**Tag der wissenschaftlichen Aussprache: 26.11.2013**



---

## ABSTRACT

Linear inverse problems arise throughout a variety of branches of science and engineering. Efficient solution strategies for these inverse problems need to know whether a problem is ill-conditioned as well as its degree of ill-conditioning. In this thesis, a comprehensive theoretical analysis of known figures of merit has been done and finally two new figures of merit have been developed. Both can be applied in a large variety of linear inverse problems, including biomedical applications and nondestructive testing of materials.

Theoretical considerations of the conditioning of linear inverse problems are applied to two examples. The first one is magnetocardiography, where the optimization of magnetic sensors in a vest-like sensor array has been considered. When measuring magnetic flux density, usually mono-axial magnetic sensors are arranged in an array, perfectly in parallel. It has been shown that a random variation of their orientations can improve the condition of the corresponding linear inverse problem. Thus, in this thesis a theoretical definition of the case when random variations of mono-axial sensors orientations improve the condition of the kernel matrix with a probability equal to one is presented. This theoretical observation is valid in general.

Positions and orientations of magnetic sensors around the torso have been optimized minimizing three figures of merit given in the literature and a novel one presented in the thesis. Best results have been found for non-uniform sensors distribution on the whole torso surface. In comparison to previous findings can be concluded that quite different sensor sets can perform equally well.

The second application example is nondestructive testing of materials named Lorentz force eddy current testing, where the Lorentz force exerting on a permanent magnet, which is moving relative to the specimen, is determined. A novel approximation method for the calculation of the magnetic fields and Lorentz forces is proposed. Based on the new approximation method, a new inverse procedure for defect reconstruction is proposed. A successful reconstruction using data from finite elements method analysis and measurements is obtained.

---

## ZUSAMMENFASSUNG

Lineare inverse Probleme tauchen in vielen Bereichen von Wissenschaft und Technik auf. Effiziente Lösungsstrategien für diese inversen Probleme erfordern Informationen darüber, ob das Problem schlecht-gestellt und in welchem Ausmaß dies der Fall ist. In der vorliegenden Dissertation wird eine umfassende theoretische Analyse existierender Bewertungsmaße durchgeführt. Aus diesen Untersuchungen werden schließlich zwei neue Bewertungsmaße abgeleitet. Beide können bei einer Vielzahl linearer inverser Probleme angewendet werden, einschließlich biomedizinische Anwendungen oder der zerstörungsfreien Materialprüfung.

Die theoretischen Betrachtungen zur Behandlung linearer inverser Probleme werden auf zwei Beispiele angewendet. Das erste ist die Magnetkardiographie, wo die Optimierung magnetischer Sensoren in einem westenähnlichen Sensorfeld untersucht wird. Für die Messungen der magnetischen Flussdichte werden üblicherweise monoaxiale Sensoren in einem Feld perfekt parallel angeordnet. Eine zufällige Variation ihrer Ausrichtungen kann die Kondition des entsprechenden linearen inversen Problems verbessern. Eine theoretische Definition des Falls, in dem zufällige Variationen monoaxialer Sensoren den Zustand der Kernmatrix mit einer Wahrscheinlichkeit gleich Eins verbessern wird ebenfalls in der Dissertation vorgestellt. Diese theoretische Beobachtung ist allgemein gültig.

Positionen und Orientierungen der Magnetsensoren rund um den Oberkörper wurden mit drei aus der Literatur bekannten Bewertungsmaßen und einem neu in dieser Arbeit vorgeschlagenen Maß optimiert. Die besten Ergebnisse ergeben sich bei einer unregelmäßigen Verteilung der Sensoren auf der Oberfläche des Brustkorbes. Im Vergleich zu früheren Untersuchungsergebnissen kann daraus geschlossen werden, dass mit geringfügig abweichenden Sensoranordnungen ebenso gute Ergebnisse erzielt werden können.

Ein zweites Anwendungsbeispiel ist ein Verfahren der zerstörungsfreien Materialprüfung, das auch als Lorentzkraft-Wirbelstromprüfung bekannt geworden ist. In dieser Arbeit wird eine neue Methode für die kontaktlose, zerstörungsfreie Untersuchung leitfähiger Materialien vorgestellt. Dabei wird die Lorentzkraft gemessen, die auf einen Dauermagneten wirkt, der relativ zu einem Testkörper bewegt. Es wird eine neue Approximationsmethode für die Berechnung der magnetischen Felder und der Lorentzkräfte vorgeschlagen.

---

## ACKNOWLEDGEMENT

This PhD thesis would not have been possible without the help and encouragement of numerous people. First, I would like to thank to my PhD supervisor, Prof. Jens Haueisen, a brilliant scientist, mentor and a teacher. I appreciate his support, contributions of time and guidance whenever I needed. My appreciation also goes to project leader, Dr. Hartmut Brauer, for fruitful discussions and his valuable suggestions for the work presented in this thesis.

I take this opportunity to sincerely acknowledge Prof. Luca Di Rienzo, for numerous scientific discussions and advice necessary for me to proceed and successfully complete the dissertation. I also thank for his hospitality during my study staying at the Politecnico di Milano, during which a theoretical investigation on rotations of three dimensional sensors has been done and also included in this thesis.

It is a great privilege to work at the Institute of Biomedical Engineering and Informatics, at the Ilmenau University of Technology, Germany. The members of this Institute contributed to my work. My research has greatly benefited from constructive discussions and suggestions from Dr. Roland Eichardt. His experience in the area of inverse problems and constructive criticism were valuable especially at the beginning of my PhD studies. I thank Dr. Uwe Graichen, whose excellent knowledge of programming in Mathematica helped me in performing necessary simulations. For help in administrative tasks and for scientific discussions as well, I thank my colleagues Dr. Daniel Baumgarten, Alexander Dietzel and Sebastian Biller. I would like to express my thanks to the secretaries Gabriela Hey and Cindy Karcher, for their administrative assistance and help.

I wish to thank Stephan Lau, for a fruitful collaboration in the optimization of sensor arrangements in magnetocardiography. I thank for the initial optimization code that I have extended by implementing different goal functions.

Special thanks to Dr. Marek Ziolkowski, his advice in performing defect reconstructions using Lorentz force eddy current testing and his suggestions in presenting the obtained results. For measuring Lorentz forces I thank to Dr. Robert Uhlig and for performing simulations in Comsol to Dr. Mladen Zec. These data are used for reconstruction of defects presented in the thesis.

I thank Ana Miletić Ilić, a great mathematician and my best friend since childhood, for honesty, trust and listening over the last twenty-five years.

I would like to thank my family for the love and infinite support throughout everything. I thank my mother Stanislava for always repeating the sentence: “You can do that”. I thank to my sons, Luka and Filip, for being my inspiration to finish this research and my beloved husband Miljan, who supported me each step on this long way.



*To my children,  
Luka and Filip*





# Table of Contents

## 1 Introduction / 3

### 1.1 Motivations / 3

### 1.2 Thesis outline and contributions / 5

## 2 Figures of merit in linear inverse problems / 9

### 2.1 Existing figures of merit in liner inverse problems / 9

#### 2.1.1 Introduction / 9

#### 2.1.2 Condition number with respect to the $L_2$ norm / 11

#### 2.1.3 Skeel condition number / 14

#### 2.1.4 Figure of merit $\rho$ / 15

### 2.2 Newly developed figures of merit in liner inverse problems / 17

#### 2.2.1 Dependency between rows/columns of a kernel matrix $RD$ / 17

#### 2.2.2 Figure of merit $\xi$ / 19

### 2.3 Comparison of figures of merit in a simulation / 20

### 2.4 Discussion / 22

## 3 Perturbations of singular values of a kernel matrix / 25

### 3.1 Introduction / 25

### 3.2 Additive and multiplicative perturbations of a kernel matrix / 25

### 3.3 Perturbation bounds for singular values / 31

### 3.4 Perturbation expansion of singular values / 32

### 3.5 Mathematical definition of the case when random variations of single-axis sensor orientations increase the smallest singular value of a kernel matrix with the probability equal to one / 33

### 3.6 Improving bounds of one variable in perturbation expansion of singular values / 36

### 3.7 Perturbation of singular values due to deleting a column or a row of a kernel matrix / 40

#### 3.7.1 Introduction / 40

#### 3.7.2 Influence of excluding sources on $CN$ with respect to the $L_2$ norm in overdetermined linear inverse problems / 40

#### 3.7.3 Influence of excluding sensors on $CN$ with respect to the $L_2$ norm in underdetermined linear inverse problems / 41

3.7.4 Condition number with respect to the  $L_2$  norm of three components measurements when all three components of magnetic dipoles are unknown is always larger than the condition number with respect to the  $L_2$  norm of one component measurements and magnetic moments of known direction (one unknown per one dipole). This is valid for both under and overdetermined problems / 41

**3.8 Theoretical proof that the condition number with respect to the  $L_2$  norm of the kernel matrix remains the same after rotations of three-axial sensors at the same point for the same angle / 42**

## **4 Application example I: Optimization of sensor arrangements in magnetocardiography / 45**

### **4.1 Introduction / 45**

### **4.2 Methods / 47**

4.2.1 Experimental setup / 47

4.2.2 Goal functions / 49

4.2.3 Clustering procedure / 49

4.2.4 Determination of the cluster representative sensor position / 50

4.2.5 Determination of the cluster representative sensor orientation / 51

### **4.3 Results / 52**

4.3.1 Sensor clusters / 52

4.3.2 Cluster medoids / 56

4.3.3 Clusters and FOMs characteristics / 59

### **4.4 Discussion / 64**

## **5 Application example II: Lorentz force evaluation / 65**

### **5.1 Introduction / 65**

### **5.2 Methodology / 66**

5.2.1 Problem description / 66

5.2.2 Forward problem - approximation method / 67

5.2.3 Inverse problem - reconstruction algorithm / 69

5.2.4 Reference forward solution / 72

### **5.3 Experiment / 74**

### **5.4 Results / 75**

5.4.1 Comparison of the forward computed defect response signals / 75

5.4.2 Reconstruction of a simulated long subsurface defect / 79

5.4.3 Reconstruction of a simulated wide subsurface defect / 82

5.4.4 Reconstruction of a long subsurface defect using the measurement data / 83

### **5.5 Discussion / 86**

## **6 Conclusions and outlook / 87**

## **7 References / 91**

**List of figures / 99**

**List of tables / 103**

# 1 INTRODUCTION

## 1.1 Motivations

The first theories of inverse problems date back to the end of the nineteenth and the beginning of the twentieth century. One of the first inverse problems solved in the past was Newton's discovery of forces making planets move in accordance with the Kepler's laws. Determination of the body's position and shape using the values of its potential presents an inverse problem in potential theory. Research regarding the internal structure of the Earth's crust involved electromagnetic fields in the theory of the inverse problems. Nowadays, more and more applications deal with the inverse problems. One of them is computerized tomography [1]. It determines the function, which is, in most of the cases, density distribution, from the values of its line integrals, playing an important role in medical applications and nondestructive testing. Solving a heat equation backwards in time presents the class of inverse heat conduction problems. Reconstruction of an obstacle or an inhomogeneity from waves scattered by those presents inverse problem named an inverse scattering.

A special class of inverse problems are linear inverse problems. They can be written as  $L \cdot x = b$ , where  $L$  is a linear operator describing the explicit relationship between the Hilbert space  $x$  and the Hilbert space  $b$ . Minimizing the residual  $\|L \cdot x - b\|$  one could find the best approximate solution of the discrete linear inverse problem. In the case of less measurement data  $b$  than unknown parameters  $x$ , this solution presents minimum norm solution that minimizes  $\|x\|$  among all residual minimizers.

According to Hadamard [2, 3], a mathematical problem is well-posed if 1) a solution exists, 2) the solution is unique and 3) the solution depends continuously on the data. If only one of these requirements is violated, the problem is called ill-posed. The last requirement of continuity is related to the stability of the solution of the linear inverse problems [4]. Continuity is a necessary but not sufficient condition for stability. This means that even if the problem is well-posed it may be ill-conditioned. Ill-conditioned problem means that a small change in an initial data leads to large changes in the solution. Therefore, when solving linear inverse problems, it is very important to investigate the error propagation from the data to the solution.

Many different measures of conditioning exist, but some of them are not always numerically stable. Furthermore, they are usually indicators of the worst conditioned component of the solution and therefore overestimate the conditioning of all other solution components. Hence, a comprehensive theoretical consideration of measures of conditioning existing in a literature is needed and development of novel figures of merit as well. These methods should be applicable to linear inverse problems in various fields.

When measuring magnetic flux density at a number of points of a scanning plane, magnetic sensors are usually equidistantly arranged and oriented in parallel. But, numerical simulations show that random variations in the sensor directions can considerably improve the condition of the magnetostatic linear inverse problem [5]. This improvement is usually a characteristic of very ill-conditioned linear inverse problems, but it is not always the case. For a given source grid and magnetic sensor array, we attend to strictly mathematically define the cases when variations of sensor orientations lead to an improvement of the condition of the corresponding linear inverse problem. The improvement in condition leads consequently to more stable inverse solutions.

Magnetocardiography non-invasively provides information about the electrical activity of the heart and is used in Magnetocardiographic Field Imaging (MFI) for the early assessment of heart dysfunctions [6]. Although MFI basic research [7, 8] and clinical studies [9] are conducted at a number of centers worldwide, it is not yet widely in use. One of the major limitations of the MFI until now is that the cryostat restricts the possible location of the superconducting quantum interference devices (SQUIDS) based sensors. New room temperature magnetic sensors [10] allow for placement of sensors around the body in a vest-like setup. Consequently, the question arises of how to place the magnetic field sensors optimally around the torso. In a study [11], Lau et al. showed that the optimization of position and orientation of a set of magnetic sensors on a plane in front of the torso allows for a reduction of the condition number of the kernel matrix of two orders of magnitude compared to a regular grid of sensors placed in front of the torso. The objective of the work presented in this thesis is to compare the practical utility of different figures of merit in the optimization of vest-like sensor arrangements for magnetocardiography. Furthermore, similarities/dissimilarities between the optimized sensor setups have to be found and compared to the previous findings.

Biomedical applications require determination of electrical conductivity of human tissues. There are two strategies suitable for electrical conductivity measurements. The first one is invasive, making a direct contact with body tissue using electrodes. The second one uses an induction coil and induces electrical currents in the tissue. This results in changes of a coil impedance. These changes are used for obtaining of an information about the tissue conductivity. This is very important since the abnormal or diseased tissue has different electrical properties comparing to the normal one.

Determination of the conductivity and application of a dipole model like in magnetocardiography serves as a basic idea for proposing for the first time a new method for non-contact, non-destructive evaluation of solid conductive materials, termed Lorentz Force Evaluation. In contrast to the magnetocardiography where magnetic flux is measured at the points above the heart, here the Lorentz force acting on a permanent magnet moving relative to the specimen is measured. Employing a three-dimensional finite volume discretization of the specimen and approximating the crack signal with an electric dipole at each voxel, a novel fast forward calculation of the Lorentz Force is proposed. This novel forward method serves as a basis for proposing a procedure for reconstruction of defects in solid conductive materials.

### 1.2 Thesis outline and contributions

The subsequent Chapter 2 of the thesis contains theoretical consideration of three measures of conditioning of linear inverse problems: condition number with respect to the  $L_2$  norm, Skeel condition number and inverse average decay of singular values of a kernel matrix. In order to overcome some disadvantages of the well-known and the mostly used condition number with respect to the  $L_2$  norm, two new error measures are developed and theoretically considered. The first one is the dependency between rows of a kernel matrix in underdetermined linear inverse problems, i.e. between columns in overdetermined linear inverse problems. This figure of merit has a number of advantages comparing to well-known figures of merit existing in a literature. First, it does not require singular value decomposition of the kernel matrix which is usually time and memory consuming. Second, it does not essentially depend on the smallest singular value as the condition number with respect to the  $L_2$  norm does. Then, it enables comparison of sensor arrays consisting of different number of sensors, in contrast to the condition number with respect to the  $L_2$  norm, which depends on the dimensions of a sensor array and consequently dimensions of a matrix. Since the multiplication of all elements of a row by the same value influences only the norm of a row vector, but not the angles to other rows, this error measure is unaffected by row scalings. The second new figure of merit also explores the geometrical features of a kernel matrix: it measures the dependency between rows of a matrix and columns of its pseudoinverse calculating the mean value of the angles between them. This error measure does not tell the sensitivity of the worst conditioned component only, but the mean sensitivity of all solution components.

These figures of merit, existing and newly developed, could be applied for optimization of sensor arrangements in wide classes of applications, like medical imaging, Lorentz force eddy current testing, seismology, geosciences and many others.

When orientations of sensors in a planar sensor array are randomly varied, numerical simulations show that the condition of the corresponding linear inverse problem could be considerably improved [5]. This effect is due to the increment of the smallest singular value of a kernel matrix and is studied, as a part of the Chapter 3, through the perturbations of this matrix. The chapter contains a derivation of a precise mathematical definition of the cases when random variations of sensor orientations lead to an increment of the smallest singular value of a corresponding kernel matrix. Furthermore, using the two ways of studying perturbations, i.e. perturbations bounds and perturbation expansion, new and sharper bounds for singular values of perturbed kernel matrices are derived. The new bounds directly depend on the singular value which is perturbed and are defined separately for over- and underdetermined linear inverse problems. This could provide better predictions of improvements of the condition of linear inverse problems.

Exclusion of a number of sensors from a sensor array or a number of sources assumed in a grid of dipoles decreases the number of rows and columns of a kernel matrix, respectively. This change of dimensions of a kernel matrix influences the value of the condition number with respect to the  $L_2$  norm. However, this influence is not, according to the author's knowledge, clearly mathematically defined in the existing literature. First, it is found that the increment/decrement of the condition number with respect to the  $L_2$  norm is dependent on over- or underdetermination of the linear inverse problem. Chapter 3 contains strict mathematical conditions under which condition number is improved due to exclusion of a number of sensors in a sensor array or a number of sources in a grid of dipoles. These conditions are given through three corollaries.

The fact that the variations of single-axis sensors orientations could improve the condition number with respect to the  $L_2$  norm of the corresponding kernel matrix triggers the question whether the variations of orientations of three-axial sensors have the same effect on the condition of the linear inverse problem. The mathematical framework presented at the end of the Chapter 3 gives the answer: if three sensors measuring at one point three orthogonal directions change the directions so that they stay mutually orthogonal, then the condition number with respect to the  $L_2$  norm of the corresponding kernel matrix remains the same.

One of the applications where solving of the linear inverse problem is needed is magnetocardiography. Searching for optimal magnetic sensor setup for measuring of a magnetic field of the heart is a topic of a Chapter 4. Positions and orientations of 21 and 32 magnetic sensors around the torso in a vest-like design are optimized. Optimization is performed minimizing four figures of merit: condition number with respect to the  $L_2$  norm, Skeel condition number, inverse average decay of singular values of a kernel matrix and a novel figure of merit based on the angles between columns of a kernel matrix and rows of its pseudoinverse, presented in the Chapter 2. The optimization is done using a quasi-continuous constrained particle swarm optimization approach. Because the solution is not unique, the optimization is repeated 256 times for all goal functions. Determination of intrinsic grouping of all sensors positions obtained after repeated runs and for each figure of merit separately is done applying a partitional clustering procedure. A position of the medoid as the most centrally located object of the cluster is taken as a position of the representative sensor of that cluster. The most frequent orientation within each cluster is taken as the representative orientation.

Optimized sensor setups show non-uniform distribution of sensors on the whole torso surface. Improvement of the condition of the linear inverse problem is obtained by placing the sensors not only on the front of the torso but also on the back. The dominant orientations of the clusters for all four figures of merit and both 21 and 32 sensor setups exhibit a mainly radial pattern around the heart. Since quite different sensor setups can perform equally well, an optimal selection of magnetic sensors for measuring magnetic field of the heart is not unique.

Detection and localization of anomalies in solid conductive materials can be done using recently proposed method named Lorentz force eddy current testing [12]. But, identification and assessment of defects are very important aspects of quality assurance. Chapter 5 presents a method for reconstruction of defects using measurements of Lorentz forces exerting on a permanent magnet moving relative to the specimen.

A solution of the forward problem is an important component of any method for computing some activity of the sources of eddy currents. For the forward solution, a new approximation method is proposed. First, in order to simplify calculation of the effect that a crack produces in the profile of the Lorentz force, we use a subtraction of the signals of the crack free system and a system containing a crack and simulate that difference as a signal produced by a grid of point-like electric dipoles placed in the defect region. The forward problem involves computing the Lorentz forces at a finite set of sensor locations for a given source configuration. Forward solution is compared with the finite element computations and the average error is for a parallelepipedic subsurface crack smaller than 5%.

Based on this approximation method, we are able to establish a kernel matrix and to apply a linear inverse scheme to estimate the unknown conductivity distributions. Thus, for the first time, a method for the reconstruction of crack geometries based on Lorentz force measurements is developed, called Lorentz Force Evaluation. Finally, a successful reconstruction using finite elements data and measurement data is obtained.

This thesis contains a set of own contributions. Chapters 2 and 3 contribute to the theory of conditioning of linear inverse problems, providing the relation between linear algebra on one side and engineering on the other side. Chapters 4 and 5 contribute to two applications, magnetocardiography and Lorentz force eddy current testing, respectively. According to the author's best knowledge of the existing literature, a list of original contributions is presented below.

Contribution	Chapter	Page
1. New approximation method for a forward solution in Lorentz force evaluation	5.2.2	67-69
2. Development of a method for reconstruction of defect geometries in conductive solid materials based on Lorentz force measurement	5.2.3	69-70
3. Optimal vest-like sensor setups for magnetocardiography		
a) Array consisting of 21 sensors	4.3.2	56-57
b) Array consisting of 32 sensors	4.3.2	57-58
4. Introduction of novel figures of merit		
a) $RD$	2.2.1	17-19
c) $\xi$	2.2.2	19-20
5. Decomposition of a lead-field matrix when magnetic flux density is measured		
a) Single-axis devices	3.2	26-29
b) Three-axis devices	3.2	29-30
6. Mathematical definition of the case when random variations of single-axis sensor orientations increase the smallest singular value of a kernel matrix	3.5	33-36
7. Improvement of bounds of one variable in perturbation expansion of singular values	3.6	36-39
8. Influence of excluding sources on condition number with respect to $L_2$ norm in overdetermined linear inverse problems	3.7.2	40
9. Influence of excluding sensors on condition number with respect to $L_2$ norm in underdetermined linear inverse problems	3.7.3	41
10. Condition number with respect to $L_2$ norm of three components measurements when all three components of magnetic dipoles are unknown is always larger than the condition number with respect to $L_2$ norm of one component measurements and magnetic moments of known direction	3.7.4	41-42
11. Rotation of three-axial sensors at the same point for the same angle do not influence condition number with respect to $L_2$ norm	3.8	42-43

---



## 2 FIGURES OF MERIT IN LINEAR INVERSE PROBLEMS

### 2.1 Existing figures of merit in linear inverse problems

#### 2.1.1 Introduction

Matrix methods are very popular and useful for the numerical simulation of physical problems. Solving of systems of linear equations can be done by applying many different algorithms. It is not easy to select a proper algorithm for a given matrix method. For example, comparing to the slower algorithms, fast algorithms require more memory or are less robust. Furthermore, the efficiency of the algorithm very much depends on the hardware. For the users of matrix solvers, it would be good to know how accurately a solution vector is computed when all matrix elements are known with the provided precision. In other words, for anyone solving a system of linear equations, it is important to know whether or not the system is ill-conditioned and if it is, to know a degree of ill-conditioning. In the case of the extremely ill-conditioned system of equations, solution components will be very sensitive to small changes in the initial data and therefore it will not be of much practical usage.

A measure of the effect of small changes in the data on the solution presents a figure of merit of a corresponding linear inverse problem. There are lots of different figures of merit depending on the ways used in measuring perturbations on the solution. Figures of merit that measure perturbations globally using norms are referred to as norm-wise condition numbers. Usage of norms is a common practice in sensitivity analysis. These figures of merit usually give an information of the worst conditioned component without the information how the perturbation is distributed among the data. Therefore they usually overestimate sensitivity especially in cases of badly scaled problems. There may exist solution components that are much better conditioned than norm-wise condition number can predict. Chandrasekaran and Ipsen [13] have shown by numerical experiments that for many classes of matrices the ill-conditioning of the matrix is due to a few rows of the matrix inverse only. So, norm-wise condition numbers cannot predict the presence of well-conditioned components. Furthermore, they are not capable to accurately assess the errors in individual solution components. Norm-wise condition numbers will be discussed in details in the following sections.

Figures of merit that measure the sensitivity of each solution component to perturbations are called component-wise condition numbers [13]. Component-wise condition number for square matrices is proposed by Rohn [14]. Let the system matrix  $L$  be of dimensions  $n \times n$  and the perturbations of that matrix are chosen so that the elements of a matrix may vary in the way that the relative error of the elements cannot exceed a positive real number  $\alpha$ . This means that  $\left| \frac{l'_{i,j} - l_{i,j}}{l_{i,j}} \right| \leq \alpha$  for each  $i, j$ , where  $L'$  is the perturbed matrix. Rohn defined the maximum

relative error in the  $i, j$ -th element of  $L^{-1}$  as:

$$c_{i,j}^{\alpha}(A) = \max \left\{ \frac{|l'_{i,j} - l_{i,j}^{-1}|}{|l_{i,j}^{-1}|}; |l'_{i,j} - l_{i,j}| \leq \alpha |l_{i,j}| \right\}. \quad (2.1)$$

This value depends on the maximal element perturbation value  $\alpha$ . In the case of infinitesimally small perturbations,  $\alpha \rightarrow 0^+$ , the component-wise condition number (2.2)

$$c_{i,j}(L) = \lim_{\alpha \rightarrow 0^+} \frac{c_{i,j}^{\alpha}(L)}{\alpha} \quad (2.2)$$

is independent of the value  $\alpha$ . If  $\alpha$  is small then  $c_{i,j}^{\alpha}(L)$  is equal to about  $c_{i,j}(L)\alpha$ .

Rohn has shown [14] that in case of nonsingular matrix  $L$  with  $l_{i,j}^{-1} \neq 0$ , for each  $i, j$ ,  $c_{i,j}(L)$  can be easily computed as:

$$c_{i,j}(L) = \frac{\left( |L^{-1}| \cdot |L| \cdot |L^{-1}| \right)_{i,j}}{|l_{i,j}^{-1}|}. \quad (2.3)$$

So, the condition number proposed in [14] is:

$$c(L) = \max \left\{ \frac{\left( |L^{-1}| \cdot |L| \cdot |L^{-1}| \right)_{i,j}}{|l_{i,j}^{-1}|}; l_{i,j}^{-1} \neq 0 \right\}. \quad (2.4)$$

The larger the  $c(L)$ , the more ill-conditioned the matrix  $L$ .

If we have two matrices  $D_1$  and  $D_2$  with positive elements, then  $c(D_1 L D_2) = c(L)$ . This means that the condition number  $c(L)$  cannot be reduced by scaling.

Component-wise measures are particularly meaningful for problems with some structure [15, 16]. Appropriately chosen component-wise measures are insensitive to diagonal scaling, leading mostly to sharper error bounds [17].

Both norm-wise and component-wise condition numbers are usually defined for the system matrix before applying any type of regularization. But, the linear inverse problems are usually highly ill-conditioned or rank deficient, requiring some regularization technique. One of the most successful methods is Tikhonov regularization. Norm-wise, mixed and component-wise condition numbers and component-wise perturbation bounds for the Tikhonov regularization are given in [18].

When solving physical problems applying matrix methods, a matrix that contains the information about the geometry of the problem and connects measurement data and unknown sources, is called system matrix or a kernel matrix. When the measurements are magnetic or electric field and unknown sources magnetic or electric dipoles, this matrix is usually called lead field matrix. Moments of magnetic dipoles are vectors and they are traditionally defined by three orthogonal dipoles in each cell of a volume domain. Dipoles positions are generally located on an assumed grid covering the domain of interest. The formulation of a lead field matrix based on having a

dipole moment of a particular strength in each orthogonal element will be referred to as element-based lead field matrix [19]. In biomedical engineering, this matrix, for example, maps three components of each dipole to magnetic flux density values (magnetoencephalography) or to electric potentials at the scalp recording electrodes (electroencephalography).

On the other hand, when one unknown is associated with one node of a grid assumed in the domain of interest, the matrix will be referred to as a node-based lead field matrix. If the number of grid points in the reconstruction space is larger than the number of measurement points, then the problem with node-based lead field matrix would be much less underdetermined than with element-based. The node-based kernel matrix with an electrical conductivity value as unknown per one grid point is used in the procedure of crack identification in Lorentz force eddy current testing in the section 5.2.3.

The whole theoretical work presented in the sections 2 and 3 of this thesis can be applied to both element-based and node-based kernel matrices. This makes the theoretical findings applicable to wide classes of linear inverse problems.

In this thesis, the theoretical consideration and numerical comparison of five different figures of merit is made. Three of them already exist in the literature: the condition number with respect to the  $L_2$  norm  $CN$ , the Skeel condition number and the ratio of the largest and the mean singular value of the kernel matrix  $\rho$ . Two additional are newly developed: dependency between rows/columns of a kernel matrix  $RD$  and dependency between rows/columns of a kernel matrix and columns/rows of its pseudoinverse  $\xi$ .

### 2.1.2 Condition number with respect to the $L_2$ norm

The determination of the condition number with respect to the  $L_2$  norm  $CN$  of a kernel matrix relies on the calculation of its singular values. For a non-singular square matrix  $L$ , the condition number with respect to the  $L_2$  norm is defined as:

$$CN = \|L\| \cdot \|L^{-1}\| = \sigma_{\max} / \sigma_{\min}, \quad (2.5)$$

where  $\sigma_{\max}(L) = \sigma_1(L) \geq \sigma_2(L) \geq \dots \geq \sigma_n(L) = \sigma_{\min}$  are nonincreasingly ordered (real and positive) singular values of  $L$ . However, significant numerical errors can occur during the computation of  $CN$  and  $CN$  essentially depends on the smallest singular value  $\sigma_{\min}$ .

This figure of merit relates the relative error of  $L^{-1}$  to the relative error of  $L$  as it can be seen from the inequality

$$\frac{\|(L + \Delta L)^{-1} - L^{-1}\|}{\|L^{-1}\|} \leq \frac{CN \cdot r(L)}{1 - CN \cdot r(L)}, \quad (2.6)$$

where  $r(L) = \|\Delta L\| / \|L\|$ , [20].

This definition is generalized to rectangular matrices of full rank into:

$$CN = \|L\| \cdot \|L^+\|, \quad (2.7)$$

where  $L^+$  presents the pseudoinverse of the matrix  $L$ .

This figure of merit has been widely used as an indicator of conditioning of linear inverse problems. Estimation of solution accuracy from the kernel matrix in magnetoencephalography in [21] relies on the condition number with respect to the  $L_2$  norm. Lee et al. found that the condition number  $CN$  had a very close relationship with the reconstruction accuracy. Various simulation studies demonstrated that the condition number  $CN$  of a kernel matrix could be used as a useful a priori index to estimate the reconstruction accuracy before the source reconstruction. This method is advantageous because the location accuracy can be estimated without solving an inverse problem. It was verified that higher condition number  $CN$  relates to poorer localization performance.

The condition number with respect to the  $L_2$  norm was used as an indicator for the stability of the inversion process [22] or as a priori accuracy estimator for the inverse problem [23]. However, there exists an unexpected observation that it is extremely unlikely to find very accurate solutions with low condition numbers [24]. This would mean that there is a high risk that a technique that reduces the condition number with respect to the  $L_2$  norm also reduces the accuracy of the results. It is a rough measure of conditioning since it assumes that the perturbation is small and also does not take into account the perturbation structure [25].

### *Influence of scaling on the condition number with respect to the $L_2$ norm*

Let a measure of scaling be defined first. A measure of (ill)scaling of the system  $Lx = b$  is proposed in [26]:

$$\max_{i,j \in J_+} (|l_{i,j}|) / \min_{i,j \in J_+} (|l_{i,j}|), \quad (2.8)$$

where  $J_+ = \{i, j | l_{i,j} \neq 0\}$ . The larger is the magnitude between the largest and the smallest absolute values of non-zero entries  $l_{i,j}$ , the worse scaled is the system. Bajalinov and Rácz [26] say that a given system matrix  $L$  is poorly scaled or badly scaled if the magnitude defined in (2.8) is larger or equal to  $1E+5$ . The aim of scaling is to make a measure (2.8) as small as possible. Fulkerson and Wolfe [27] propose a method for finding such scale factors that minimize the value (2.8). They state that this number as a measure of scaling is a useful condition number. Based on the assumption that the original matrix can be scaled in such a way that all matrix elements are of comparable size, Curtis and Reid [28] present an algorithm for scaling.

The influence of scaling on the condition number with respect to the  $L_2$  norm has been studied by Golub and Varah [29], Bauer [30], Businger [31], Braatz and Morari [32], McCarthy and Strang [33], Watson [34] and Rump [35]. If the condition number of the scaled kernel matrix  $L_s$  can be made considerably smaller than the condition number of the original kernel matrix  $L$ , then we might expect a more accurate solution obtained by inverting the scaled matrix [36]. This is in fact the objective of scaling in [36]. A poor computed solution could be a consequence of the disparity in sizes of the elements of the kernel matrix  $L$  [37]. Stewart proposes scaling of rows and columns of  $L$  so that the matrix becomes balanced.

The reduction of condition number or normalization of magnitudes of the system matrix elements provides a satisfactory explanation of the influence of scaling on partial pivoting in the Gaussian elimination algorithm. Scaling can drive or control the selection of pivots for any strategy based on the magnitude of matrix elements [38]. This algorithm can also be used to calculate the determinant of a matrix, find the rank of a matrix or to calculate the inverse of an invertible square matrix. Applying elementary row operations are used in order to reduce a

system matrix to a triangular form. An extension of this algorithm, Gauss-Jordan elimination, reduces the matrix further in a diagonal form known as reduced row echelon form. The Gaussian elimination computes matrix decomposition. Three elementary row operations are used in Gaussian elimination: multiplying rows, switching rows and adding multiple of rows to other rows. The first part of the algorithm computes the LU decomposition while the second part writes the original matrix as the product of a uniquely determined invertible matrix and a uniquely determined reduced row-echelon matrix. Studying of positive and negative effects of scaling on the selection of pivots based on partial pivoting is done in [38]. Skeel also provides an important insight into the subject of scaling [39, 40], showing the effect of scaling on the stability of Gaussian elimination. Geometrical analysis of Gaussian elimination is presented in [41].

A motivation for scaling to make pivoting work well is presented by Forsythe and Moler [42]. For the system of linear equations  $Lx = b$ , a pair of nonsingular diagonal matrices  $(D, F)$  determine the scaling of the system through the following equations:  $D(LF)y = Db$ , and  $y = F^{-1}x$ . When the system of equations is solved by Gaussian elimination and the scaling is implemented along with partial pivoting, certain ordered pairs  $(D, F)$  produce better solutions than those obtained without scaling while some pairs produce worse solutions. There are two reasons for this: first,  $(D, F)$  influence the condition number with respect to the  $L_2$  norm of the kernel matrix and second,  $(D, F)$  modify the magnitudes of the elements of the matrix  $L$ .

In the case when scaling yields elements of a kernel matrix of approximately the same magnitude, this is called equilibration. When matrix  $F$  is the identity matrix, then scaling by a pair  $(D, I)$  is called a row scaling, while  $(I, F)$  denotes a column scaling.

However, a more satisfactory explanation of the positive and negative effects of scaling on partial pivoting lies in the orientation of hyperplanes corresponding to the linear system [39]. Numerical consequences of orientation of hyperplanes in Gaussian elimination are presented in [41]. In the case of a symmetric matrix  $L$  that contains no null rows, Bunch [43] presents an algorithm for finding a scaled matrix  $DLE$  which is equilibrated in the  $\infty$ -norm.

### *Sensitivity of the condition number with respect to the $L_2$ norm*

Computation of the condition number  $CN$  requires computation of the singular values of the kernel matrix of a corresponding linear inverse problem. The accurate computation of the singular values requires singular value decomposition (SVD) which is in case of very large matrices time and memory consuming. Due to the loss of accuracy already in the SVD algorithm, computation of the condition number with respect to the  $L_2$  norm is also inaccurate. This is especially true for very large condition numbers. Considering the definition of the condition number with respect to the  $L_2$  norm (2.5 and 2.7), its accuracy crucially depends on the smallest singular value  $\sigma_{\min}$ .

When computing the condition number with respect to the  $L_2$  norm, it is of high interest to know the accuracy of the computations. This problem was investigated by Demmel [44]. He showed that for certain fundamental problems in numerical analysis, including matrix inversion, “the condition number of the condition number is the condition number”. Higham [17] has shown that for the cases of matrix inversion and the solution of linear systems, the sensitivity of the condition number is given by the condition number itself. This condition number is called level-2 condition number.

Equivalent to the condition number with respect to the  $L_2$  norm, but not relying on the singular values of a kernel matrix and with a direct geometrical interpretation, Chehab and Raydan [45] define the Frobenius condition number. This number is related to the cosine of the angle between a given positive definite matrix and its inverse. In fact, bounds for the ratio between the angle that a matrix forms with the identity matrix and the angle that the inverse of a matrix forms with the identity matrix, are defined in [45].

Cosine of the angle between two matrices  $A$  and  $B$  is given in [46]

$$\cos(A, B) = \frac{\langle A, B \rangle_F}{\|A\|_F \|B\|_F}, \quad (2.9)$$

where the definition of the Frobenius inner product is given as

$$\langle A, B \rangle_F = \text{tr}(A^T B). \quad (2.10)$$

In the case of the cosine of the angle between the matrix and the identity matrix, we have:

$$\cos(A, I) = \frac{\text{tr}(A)}{\|A\|_F n^{1/2}}. \quad (2.11)$$

$\text{tr}(A)$  and  $\|A\|_F$  denote the trace and the Frobenius norm of the matrix  $A$ . Based on these bounds and requiring only the trace and the Frobenius norm of a matrix, new lower bounds for the condition number  $CN$  are established [45].

### 2.1.3 Skeel condition number

The Skeel condition number is first proposed for square matrices in [39] and then generalized to rectangular matrices in [47]. Let the matrix  $L$  be a kernel matrix of the system of linear equations. When the system is overdetermined (more rows than columns), the Skeel condition number is defined as

$$\text{Skeel}(L) = \left\| |L| \cdot |L^+| \right\| \quad (2.12)$$

and is invariant under column scaling, while for underdetermined system of linear equations (more columns than rows), it is defined as

$$\text{Skeel}(L) = \left\| |L^+| \cdot |L| \right\| \quad (2.13)$$

and is invariant under row scaling. Scaling here means left multiplication of a matrix by a nonsingular diagonal matrix, giving  $\text{Skeel}(DL) = \text{Skeel}(L)$ .

$| \cdot |$  in expressions (2.12) and (2.13) indicates that all elements of the matrices  $L$  and  $L^+$  are replaced by their absolute values and  $\| \cdot \|$  denotes the  $L_2$  norm.  $L^+$  is the pseudoinverse of matrix  $L$ .

The Skeel condition number is equal to one for any matrix where only the entries  $l_{i,i}$  are nonzero. Therefore, an overestimation of the ill conditioning using the condition number  $CN$  in the case of a matrix containing non-zero entries only on positions  $i, i$  is overcome using the Skeel condition number. This type of a matrix usually does not appear in solving of real physical problems.

The Skeel condition number cannot be much larger than  $CN$ , since [47]:

$$Skeel(L) \leq \left\| \begin{bmatrix} L^+ \\ |L| \end{bmatrix} \right\| \leq n \left\| L^+ \right\| \left\| L \right\| = m \cdot CN(L), \quad (2.14)$$

where  $L$  is a rectangular matrix of dimensions  $n \times m$  and  $rank(L) = n \leq m$ .

The Skeel condition number can be much smaller than the condition number with respect to the  $L_2$  norm.

Being independent of any row or column scaling, the Skeel condition number better reflects the inherent condition of the matrix. Any reordering of the linear equations in the system does not change the value of the Skeel condition number. But, reordering of the equations mostly influences the solution obtained by applying Gaussian elimination (see section 2.1.2). Furthermore, Skeel concluded that a proper way to scale a system matrix depends on the properties of the solution of the system [39, 40]. This information is unfortunately usually not available.

The fact that scaling does not influence the Skeel condition number and the observation of Arioli et al. [15] about overcoming bad row scaling with iterative refinement, suggest that scaling or equilibration may be unnecessary. Hamming [48] and Moler [49] support this position.

### 2.1.4 Figure of merit $\rho$

In order to increase the numerical stability of the evaluation of the condition number with respect to the  $L_2$  norm and to reduce its dependency on the smallest singular value of a kernel matrix  $\sigma_{\min}$ , a figure of merit  $\rho$  is proposed as a new condition measure [50]:

$$\rho(L) = \frac{\sigma_1(L)}{\frac{1}{n} \sum_{i=1}^n \sigma_i(L)} = \left( \frac{1}{n} \sum_{i=1}^n \frac{\sigma_i(L)}{\sigma_1(L)} \right)^{-1}. \quad (2.15)$$

$\rho$  represents the ratio between the largest and the mean singular values of the kernel matrix  $L$  as it can be seen from the first part of the expression (2.15). The second part of the expression (2.15) provides an equivalent interpretation of this measure as the inverse of the average decay of the singular values of the kernel matrix  $L$ .

Larger values of  $\rho$ , as of  $CN$ , indicate a worse condition of the kernel matrix  $L$  and therefore a worse conditioned linear inverse problem.

This figure of merit is related to the area under the curve representing the slope of singular values. The relation is derived below.

Let us observe the curve representing singular values of a kernel matrix normalized by the largest singular value. In order to approximate the total area underneath this curve, the method of Riemann sum is used. A left Riemann summation method is presented in the Fig. 2.1. This method makes an approximation using the left endpoint of each subinterval.

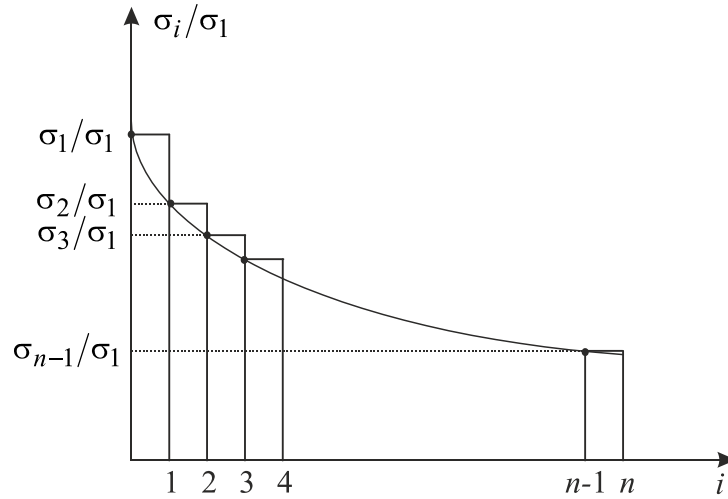


Fig. 2.1 – Left Riemann summation method in calculation the area under the curve of normalized singular values of a kernel matrix.

Let the interval  $(0, n)$  be divided into  $n$  subintervals, each of length  $\Delta = (n - 0)/n = 1$ . The points in the partition will then be  $0, 0 + \Delta, 0 + 2\Delta, \dots, (n - 2)\Delta, (n - 1)\Delta, n$ . The curve is approximated by the value at the left endpoint. This gives multiple rectangles of one side  $\Delta$  and the other side  $f(0 + i\Delta)$ . Doing this for  $i = 0, \dots, n - 1$  and summing up all the subareas, we get:  $\Delta(f(0) + f(0 + \Delta) + \dots + f(n - \Delta))$ , i.e.  $\Delta(\sigma_1/\sigma_1 + \sigma_2/\sigma_1 + \dots + \sigma_{n-1}/\sigma_1)$ . This is the area under the curve representing all singular values normalized by the largest singular value of a kernel matrix. Let it be denoted as *area*.

When the singular values are simple (there are no two equal singular values), the curve representing them is monotonically decreasing function. In that case the left Riemann sum amounts to an overestimation of the area under the curve. The right Riemann sum would in that case underestimate the area under the curve.

On the other hand, the inverse value of the figure of merit  $\rho$  (2.15) can be written as:

$$\frac{1}{\rho} = \frac{1/n \sum_{i=1}^n \sigma_i}{\sigma_1} = \frac{1}{n \sigma_1} (\sigma_1 + \sigma_2 + \dots + \sigma_{n-1} + \sigma_n). \quad (2.16)$$

In the case of very small the last singular value, the following holds:

$$\frac{1}{n \sigma_1} (\sigma_1 + \sigma_2 + \dots + \sigma_{n-1} + \sigma_n) \approx \frac{1}{n \sigma_1} (\sigma_1 + \sigma_2 + \dots + \sigma_{n-1}). \quad (2.17)$$

The expression (2.19) could be written as:

$$\frac{1}{n \sigma_1} (\sigma_1 + \sigma_2 + \dots + \sigma_{n-1}) = \frac{1}{n} \text{area}. \quad (2.18)$$

At the end, we have that the inverse of the figure of merit  $\rho$  is approximately equal to:

$$\frac{1}{\rho} \approx \frac{1}{n} \text{area}. \quad (2.19)$$



Since the changes of  $1/\rho$  are accompanied by changes in the *area* and the changes are always related by use of a constant, this means that  $1/\rho$  is directly proportional to the *area*. The coefficient of proportionality is equal to  $1/n$ , where  $n$  represents the number of singular values. When comparing two different sensor arrays, a direct comparison of areas under the curves makes sense only in the case of the same number of singular values of the kernel matrices. This means that in underdetermined problems, only the sensor arrays with the same number of sensors can be compared since in this case the number of singular values is equal to the number of sensors. Or, if truncation is applied, sensor arrays containing different number of sensors could be compared, but the truncation has to be the same, i.e. the number of singular values used for the inversion of both kernel matrices. In the case of overdetermined problems, the number of singular values is equal to the number of columns of kernel matrices (when matrices are of full column rank). This enables comparison of sensor arrays containing different number of sensors using the approach of the area under the curve of normalized singular values of a kernel matrix.

The figure of merit  $\rho$  represents the inverse of area under the curve of singular values of a kernel matrix. The larger is the area under the curve, the smaller is the  $\rho$  and consequently the better conditioned linear inverse problem.

A direct visual comparison of the areas under the curves representing the singular values of the corresponding kernel matrices makes sense only if the singular values are normalized by the largest singular value (in that case both curves start at the same point  $\sigma_1/\sigma_1 = 1$ ).

The larger area under the curve representing the singular values normalized by the largest one corresponds to the smaller steepness of this curve. Minimization of the steepness of the slope of singular values is used in optimizing the magnetic sensor arrangements in magnetocardiography [51]. In fact, they directly compared singular value decays as a measure of the information content of different sensor arrays. When the correlations among the matrix rows in underdetermined problems and matrix columns in overdetermined problems are small, then a kernel matrix exhibits a low decay of singular values. In this case the rows contain little redundant sensitivity information on the sources. So, the information content of measurements provided by the modeled sensor array on the considered source distribution is high.

## 2.2 Newly developed figures of merit in linear inverse problems

### 2.2.1 Dependency between rows/columns of a kernel matrix *RD*

One of the sources of instability of linear techniques arises from the linear dependency between rows of the matrix of a linear system [52]. Izquierdo and Guerra introduced an additional strategy to overcome this problem. Their strategy improves the stability and accuracy of the linear approach even further while reducing the computational cost. In fact, they proposed a method to automatically select the most linearly independent rows in the matrix and to perform estimation with these rows only. They show in simulations that the magnitude of the condition number with respect to the  $L_2$  norm of the matrix built with the  $q$  most independent rows, is minimal comparing to the condition number of the matrix formed by any combination of  $q$  different rows of the matrix (Fig. 2 in [52]). If one has a planar sensor array containing  $n$  sensors and wants to select  $q$  of them leading to a minimal condition number with respect to the  $L_2$  norm, he can explore the same idea of  $q$  the most independent rows.

Here arises a question of how to relate a linear dependency between rows of a kernel matrix and its condition number with respect to the  $L_2$  norm. A very convenient criterion to measure the

degree of linear dependency is given by the distance of the matrix  $L$  to the closest singular matrix [52]. The minimum distance between a given matrix  $L$  and a singular matrix is given by the smallest singular value of  $L$  (Lemma 2 in [52]). The proof of this result is given in [53, section 2.5.3]. This lemma allows to relate the linear dependency between rows of a matrix and the condition number with respect to the  $L_2$  norm. The higher is the linear dependency between rows of  $L$ , the smaller is its smallest singular value and therefore larger the condition number with respect to the  $L_2$  norm.

Geometrical interpretation of the linear dependency between a matrix row/column and a space spanned by the all other rows/columns have been used before. The angle between a row of a matrix and a space spanned by all other rows is employed to estimate the degree of information this particular row adds to the other rows of a matrix [54]. If many rows add little or no additional information, the matrix is ill-conditioned. An approximate expression for the condition number  $CN$  of a well-scaled matrix in terms of the minimum angle between a column vector of a matrix and a linear subspace spanned by the remaining columns is derived in [55]. An interesting inequality is given in [56], showing that either the columns of a matrix are nearly dependent or the kernel matrix is not well-scaled if the  $CN$  is high.

In order to overcome the same problem, Sabatier [54] suggested ordering the rows with respect to the value of the angle the row of a matrix has with the space spanned by all other rows. This is the angle describing the independence of each row relative to all other rows. A row with large angle contributes to the model. Rows having the small angle are largely responsible for ill conditioning of underdetermined linear inverse problems. Sabatier proposed improving the conditioning of the system matrix using in inversion only the rows for which this angle is larger than some noise-dependent threshold.

Let  $L = [\vec{l}_1, \vec{l}_2, \dots, \vec{l}_n]^T$  be a kernel matrix of an underdetermined problem, where  $\vec{l}_i$  is the  $i^{\text{th}}$  row vector of  $L$  and  $n$  corresponds to the number of sensors. By computing the mean value of the angles among all  $\vec{l}_i$ , we get a figure of merit of rows dependency,  $RD$ :

$$RD = \frac{\sum_{i=1}^{n-1} \sum_{j=i+1}^n \left| 90^\circ - \left| \cos^{-1} \left( \frac{\vec{l}_i \cdot \vec{l}_j}{\|\vec{l}_i\| \cdot \|\vec{l}_j\|} \right) \right| \right|}{\frac{n!}{2!(n-2)!}}. \quad (2.20)$$

In order to indicate a well-conditioned matrix by a small value, as in the figures of merit presented in the section 2.1, a subtraction of each obtained angle from  $90^\circ$  is imposed in expression 2.22.  $||$  indicates that the absolute values of the angles and of the differences are used.  $\|\cdot\|$  denotes the  $L_2$  norm.  $RD = 0^\circ$  corresponds to the set of linearly independent rows, while a set of parallel vectors is denoted by  $RD = 90^\circ$ . If the problem is overdetermined, i.e. a matrix contains more rows than columns, then the angles between columns are measured. In that case this figure of merit is referred to as columns dependency  $CD$ .

Calculation of the figure of merit  $RD$  has a few advantages in comparison to the condition number with respect to the  $L_2$  norm. First, computation of  $RD$  does not require singular value decomposition of a matrix. Second, it enables the comparison of lead field matrices of different sizes. Furthermore, condition number with respect to the  $L_2$  norm is dependent on row scaling

in the case of underdetermined problems and on column scaling in the case of overdetermined problems. We do know that the multiplication of all elements of a row by the same value influences only the norm of a row vector, but not the angles to other rows. Thus,  $RD$  is independent of row scaling. In the same way,  $CD$  is independent on column scaling. These features of the proposed  $RD$  for underdetermined problems and  $CD$  for overdetermined problems are promising for further applications.

### 2.2.2 Figure of merit $\xi$

Let us consider a matrix  $L$  of dimensions  $n \times m$ ,  $n > m$ . Columns of a matrix  $L$  are denoted by  $a_i$  and the rows of its pseudoinverse  $L^+$  by  $r_i$ . Since the norm-wise condition numbers cannot predict the well-conditioned components in the solution vector, Chandrasekaran and Ipsen [57] proposed component-wise condition number

$$\|L\| \cdot \|r_i\|, \quad i = 1, \dots, m, \quad (2.21)$$

where  $\|L\|$  represents the  $L_2$  norm of the matrix  $L$  and  $\|r_i\|$  the length of the vector  $r_i$ ,  $i = 1, \dots, m$ . This condition number measures the sensitivity to perturbation of each solution component separately.

In the case of matrix  $L$  of full column rank (Theorem 5 in [57])

$$\|r_i\| = 1/(\|a_i\| \cdot \cos(\alpha_i)), \quad -\pi/2 < \alpha_i < \pi/2, \quad i = 1, \dots, m. \quad (2.22)$$

Now, (2.21) becomes

$$\frac{\|L\|}{\|a_i\| \cdot \cos(\alpha_i)}, \quad i = 1, \dots, m. \quad (2.23)$$

Values  $\|a_i\| \cdot \|r_i\|$  are known as collinearity indices [58]. According to (2.22) these indices are equal to  $1/\cos(\alpha_i)$ . They represent in fact a scaling invariant version of (2.23) [57].

Based on the component-wise condition number of Chandrasekaran and Ipsen, a novel figure of merit,  $\xi$ , is proposed:

$$\xi = \frac{\|L\|}{\text{Mean}(\|a_i\| \cdot \cos(\alpha_i))}. \quad (2.24)$$

In contrast to the condition number with respect to the  $L_2$  norm, this figure of merit does not predict the sensitivity on perturbations of the worst conditioned solution component. Similar to  $\rho$ , where the largest singular value is divided by the mean of all singular values, a denominator in  $\xi$  is equal to the mean of the products of the lengths of the column vectors of the kernel matrix  $L$  and cosines of the angles between those vectors and corresponding rows of the pseudoinverse  $L^+$ .

Figure of merit  $\xi$  is directly proportional to the largest singular value of a system matrix  $L$  and inversely proportional to the mean value of products of lengths of the vectors representing the columns of the system matrix  $L$  and cosines of the angles between the columns of  $L$  and the corresponding rows of its pseudoinverse  $L^+$ . The smaller are these products, the smaller is the mean and therefore the larger value of  $\xi$ .

When a linear inverse problem is underdetermined with a kernel matrix  $L$  of dimensions  $n \times m$ ,  $m > n$ , then  $a_i$ ,  $i = 1, \dots, m$ , represent the rows of  $L$ ,  $r_i$ ,  $i = 1, \dots, m$ , are the columns of  $L^+$ , while  $\alpha_i$  are the angles between rows  $a_i$  and corresponding columns  $r_i$ ,  $i = 1, \dots, m$ .

In contrast to the another proposed novel figure of merit, i.e. the dependency between rows/columns of a kernel matrix which can be computed using the data in the matrix only, calculation of the figure of merit  $\xi$  requires determination of the pseudoinverse of the kernel matrix.

### 2.3 Comparison of figures of merit in a simulation

In order to study features of three figures of merit already existing in literature and presented in section 2.1 and two newly proposed figures of merit described in the section 2.2, and to make a comparison between them, numerical simulation has been done. Here, the influence of the number of sensors in an array in the case of underdetermined linear inverse problem has been investigated. A  $15 \times 15$  grid of three component magnetic dipoles are kept constant. The number of sensors are changed from 100 to 144. Dipoles are placed in the area  $(x_{\min}, x_{\max}) = (-0.02 \text{ m}, 0.22 \text{ m})$ ,  $(y_{\min}, y_{\max}) = (-0.02 \text{ m}, 0.22 \text{ m})$ , 0.05 m underneath a sensor array. All the sensors are uniformly oriented along the  $z$ -direction and placed in the area  $(x_{\min}, x_{\max}) = (0 \text{ m}, 0.2 \text{ m})$ ,  $(y_{\min}, y_{\max}) = (0 \text{ m}, 0.2 \text{ m})$ .

The dependencies of the condition number with respect to the  $L_2$  norm  $CN$ , Skeel condition number, inverse average decay of the singular values of a kernel matrix  $\rho$  and two newly proposed  $RD$  and  $\xi$ , normalized by their values when 124 sensors are used, are presented in the Fig. 2.2.

$CN$  changes from 2661.52 to 2934.69,  $Skeel$  from 3786.06 to 4695.11,  $\rho$  from 7.11 to 7.26,  $RD$  from  $8.05^\circ$  to  $7.32^\circ$  and  $\xi$  from 25832.2 to 40170.3. All the figures of merit are increasing with increasing the number of sensors, except only the  $RD$ .

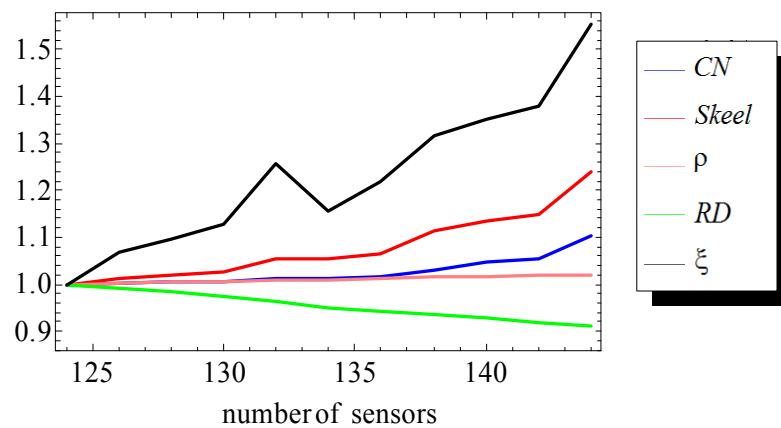


Fig. 2.2 – Dependence of normalized measures of conditioning of a kernel matrix.

A theoretical proof that the  $CN$  in the case of underdetermined linear inverse problem increases with increasing number of sensors (adding sensors) is done in the section 3.7.3 and therefore is expected.  $Skeel$ ,  $\rho$  and  $\xi$  behave in the same way. The only different figure of merit is  $RD$ . In the case of less number of sensors than the number of unknown sources, it is natural that further

decreasing of the number of sensors would lead to a worse conditioned linear inverse problem, as indicated by  $RD$ . This could be very promising for further investigations and application of  $RD$ .

Usually, all these figures of merit behave in the same way [59, 60]. In the case of underdetermined linear inverse problem, decrement of the number of sensors leads to a decrement of all mentioned error measures, but only when keeping the area of sensor array constant. When sensors belonging to one sensor array are being excluded one after the other, meaning also that the area of sensor array becomes smaller, then figure of merit  $RD$  increases while  $CN$ ,  $Skeel$ ,  $\rho$  and  $\xi$  decreases (Fig. 2.2).

In order to verify that the lower condition number  $CN$  could relate to poorer localization performance, a reconstruction of magnetic dipole is performed. A magnetic dipole of the magnetic moment  $\vec{m} = 1 \text{ nAm}^2 \hat{z}$  is placed at point  $(0.12 \text{ m}, 0.12 \text{ m})$ ,  $0.05 \text{ m}$  underneath a sensor array. The first reconstruction is performed using a sensor array containing  $n = 144$  uniformly  $z$ -oriented sensors placed in the area  $(x_{\min}, x_{\max}) = (0 \text{ m}, 0.2 \text{ m})$ ,  $(y_{\min}, y_{\max}) = (0 \text{ m}, 0.2 \text{ m})$ . The second reconstruction is performed using a sensor array containing  $n = 75$  sensors, obtained after exclusion of 69 sensors from the array. An assumed grid of dipoles described in the first paragraph of this section is kept the same in both cases. The results of the reconstruction procedure applying singular value decomposition of a kernel matrix are presented in Fig. 2.3a and 2.3b. Obtained magnetic moments of dipoles are normalized by the largest one and presented using a color scale shown in Fig. 2.3c. In the case when  $n = 144$  sensors are used, the simulated magnetic dipole is reconstructed (red point exactly at the position of simulated dipole). On the other hand, reconstruction using an array of  $n = 75$  sensors performs well with respect to  $x$  coordinate, while  $y$  coordinate is determined within an inaccuracy of  $0.02 \text{ m}$ .

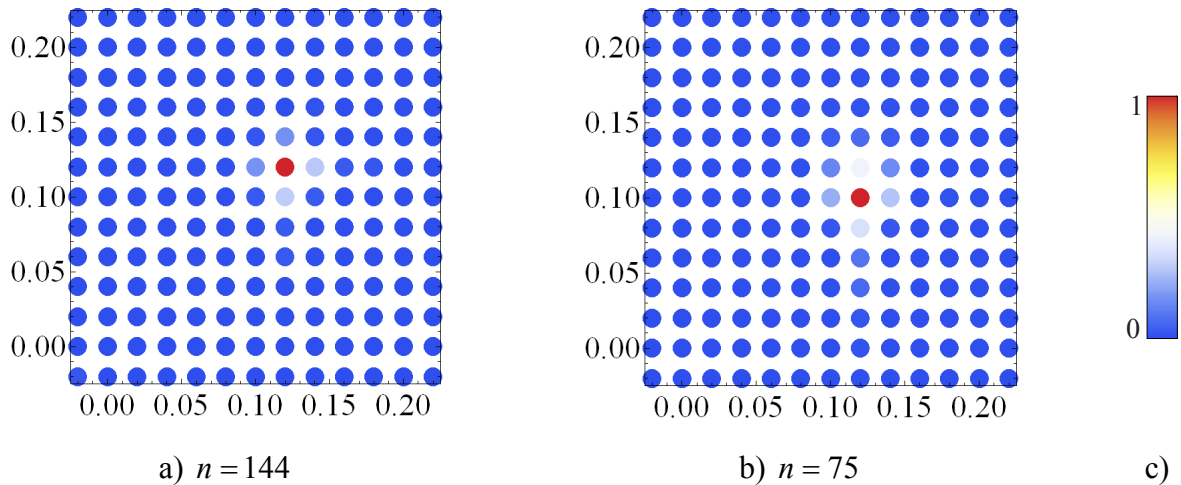


Fig. 2.3 – Representation of normalized magnetic moments of dipoles in an assumed dipole grid, obtained by using an array of  $n = 144$  sensors (a) and  $n = 75$  sensors (b), color-coded using the color scale (c). Simulated dipole is placed at point  $(0.12 \text{ m}, 0.12 \text{ m})$ .

This reconstruction result confirms well the predicted conditioning of the linear inverse problem and a good reconstruction accuracy using the figure of merit  $RD$ . It also shows that the lower value of the condition number with respect to the  $L_2$  norm is not a priori indicator of a lower error in the inverse solution. Or, at least, results confirm once more that a comparison of sensor arrays containing different number of sensors cannot be done using the condition number with respect to the  $L_2$  norm.

### 2.4 Discussion

Depending on the way the figures of merit measure the errors in a solution with respect to perturbations in the input data, they can be divided into three main groups. The first group are norm-wise condition numbers. This kind of condition number measures the size of both input perturbations and output errors using some norms. Condition number with respect to the  $L_2$  norm belongs to this group. As a norm-wise condition measure, it gives the error bound of the worst conditioned component in the solution vector and therefore overestimates a condition of a kernel matrix.

A second group of figures of merit can predict the errors in each component of the solution vector. These figures of merit are referred to as component-wise error measures. This is important when we are interested in one solution component particularly and there is no risk of overestimation of the error. Condition numbers presented by Rohn (formula 2.3) and Chandrasekaran and Ipsen (formula 2.21) belong to the group of component-wise condition numbers.

Skeel condition number,  $\rho$  and  $\xi$  are of the mixed type. Mixed type means that the error measure takes into account perturbations in all input elements, but at the end uses some norm to predict the error.  $\rho$  for example takes into account all the singular values of the system matrix, while  $\xi$  depends on the cosines of the angles between all the columns (rows) of a system matrix and rows (columns) of its pseudoinverse. Since they do not calculate the worst conditioned component of the solution vector, a system matrix can be better conditioned in a mixed sense than in norm-wise sense. The classification of figures of merit is presented by scheme in Fig. 2.4. As not using any of norms, the figure of merit  $RD$  is presented as a separate, not belonging to any group.

While calculation of the condition number with respect to the  $L_2$  norm and the inverse average decay of singular values requires performing the singular value decomposition, and the *Skeel* and  $\xi$  determination of the pseudoinverse of a kernel matrix, it is not required for condition determination using  $RD$ . Calculation of  $RD$  relies only on values of kernel matrix elements. Furthermore, computed singular values deviate from the true values. In fact, only singular values close to the largest one, can be computed with a high relative accuracy. When computing the condition number with respect to the  $L_2$  norm, we perform a division by the smallest singular value, which is numerically instable [61].

Figures of merit differ also with respect to the sensitivity on scaling. Generally speaking, one system of linear equations should not be affected by bad scaling of a kernel matrix. In that sense, using of the *Skeel* condition number or dependency between rows/columns  $RD$  should be of advantage. But, in real applications, when for example in optimization of sensor positions one wants to exclude sensors far away from the source (the signal to noise ratio would be bad assuming approximately uniform distribution of the noise at all sensors positions), then one should use condition number with respect to the  $L_2$  norm,  $\rho$  or  $\xi$ . These figures of merit are influenced by scaling.

Reordering of rows/columns within a kernel matrix does not influence any of figures of merit mentioned in sections 2.1 and 2.2. On the other hand, reordering in the most cases influences a solution obtained by Gaussian elimination. With respect to the reordering of rows/columns and when applying Gaussian elimination, none of these measures is of advantage.

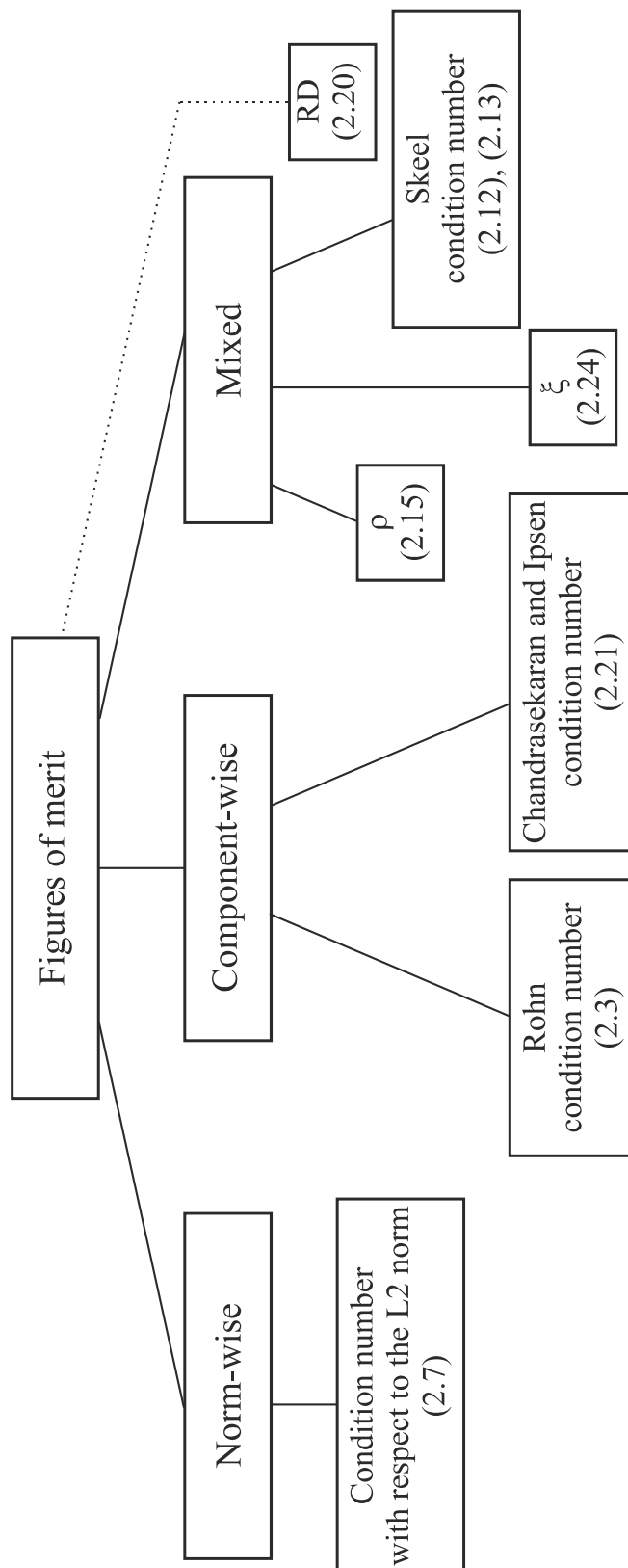


Fig. 2.4 – Classification of figures of merit.

---



## 3 PERTURBATIONS OF SINGULAR VALUES OF A KERNEL MATRIX

### 3.1 Introduction

Measuring of magnetic field has a very diverse range of applications, including locating objects such as submarines, hazards in coal mines, heart beat monitoring, anti-locking brakes, archaeology, mineral exploration, in spacecrafts or eddy current testing of materials. The magnetic field is characterized by the magnetic flux density, measured in  $\text{Wb/m}^2$ . Magnetometers can be, depending on what they measure, divided into two basic groups. The first one are so called scalar magnetometers that measure the total strength of the magnetic flux density, but not its direction. The second group consists of magnetometers that have a capability to measure the component of the magnetic flux density in a particular direction. They are referred to as vector magnetometers. If the vector magnetometers measure only one component of the magnetic flux density, they will be referred to as single axis devices. On the other hand, it is possible to combine three axis sensors to get three flux density measurements at one point. These sensors are referred to as three-axis devices.

When an array of single component vector magnetometers is used, sensors are usually uniformly oriented i.e. they measure the same component of magnetic flux density at all the points of an array. But, numerical simulations have shown that random sensor variations of single component vector magnetometers could lead to a better conditioned linear inverse problem [5]. The effect of sensor orientations variations on the condition of corresponding linear inverse problem will be studied through the perturbations of kernel matrix.

### 3.2 Additive and multiplicative perturbations of a kernel matrix

Let a kernel matrix of dimensions  $m \times n$  be denoted as  $L$ . In the theory of perturbations, there are two different perturbation models:

- *Additive* perturbations that represent perturbed matrix as  $L + E$ , where matrix  $E$  has same dimensions as  $L$ ; and
- *Multiplicative* perturbations that represent perturbed matrix as  $DL$ ; matrix  $D$  can be a square matrix leading in that case to the perturbed matrix of the same dimensions as  $L$  or a rectangular matrix increasing/decreasing the number of rows of the resulting perturbed matrix with respect to the number of rows of original matrix  $L$ .

In case of linear inverse problems, where matrix  $L$  represents a kernel matrix, variations of sensor orientations will be represented as additive and multiplicative perturbations of a kernel matrix, separately defined for single axis and three-axis devices. Theoretical considerations will be done for three component magnetic dipoles as unknown sources and single axis and three-axis devices measuring the magnetic flux density. Nevertheless, the theory is general and holds for any kind of single axis or three-axis measurements and any kind of unknown sources.

#### Single axis devices

Let the number of single axis sensors be  $n$  and the number of magnetic dipoles  $m$ . There is no assumption about the orientation of magnetic dipoles: there are three unknown magnetic moments per each dipole.

Position and direction of the  $i^{\text{th}}$  single axis sensor are expressed as:

$$\vec{d}_i = d_{ix}\hat{x} + d_{iy}\hat{y} + d_{iz}\hat{z}, \quad i = 1, \dots, n, \quad (3.1)$$

$$\vec{r}_i = r_{ix}\hat{x} + r_{iy}\hat{y} + r_{iz}\hat{z}, \quad i = 1, \dots, n, \quad (3.2)$$

Position vector of the  $j^{\text{th}}$  magnetic dipole is:

$$\vec{R}_j = \vec{R}_{jx}\hat{x} + \vec{R}_{jy}\hat{y} + \vec{R}_{jz}\hat{z}, \quad j = 1, \dots, m, \quad (3.3)$$

having a magnetic moment:

$$\vec{m}_j = m_{jx}\hat{x} + m_{jy}\hat{y} + m_{jz}\hat{z}, \quad j = 1, \dots, m. \quad (3.4)$$

Magnetic flux density  $\vec{b}$  at the position of the  $i^{\text{th}}$  single axis sensor produced by the  $j^{\text{th}}$  magnetic dipole is described by the well-known formula (3.5):

$$\vec{b}_{ij} = \frac{\mu_0}{4\pi} \left[ \frac{3\vec{m}_j(\vec{r}_i - \vec{R}_j)}{|\vec{r}_i - \vec{R}_j|^5} (\vec{r}_i - \vec{R}_j) - \frac{\vec{m}_j}{|\vec{r}_i - \vec{R}_j|^3} \right], \quad i = 1, \dots, n, \quad j = 1, \dots, m. \quad (3.5)$$

Magnetic flux density  $\vec{b}_{ij}$  is then decomposed into three components corresponding to projections of vector  $\vec{b}_{ij}$  on three mutually orthogonal axes of Cartesian coordinate system:

$$\vec{b}_{ij} = b_{ijx}\hat{x} + b_{ijy}\hat{y} + b_{ijz}\hat{z}, \quad i = 1, \dots, n, \quad j = 1, \dots, m, \quad (3.6)$$

where

$$b_{ijx} = \frac{\mu_0}{4\pi} [3p_{ij}(r_{ix} - R_{jx}) - q_{ij}m_{jx}], \quad (3.7)$$

$$b_{ijy} = \frac{\mu_0}{4\pi} [3p_{ij}(r_{iy} - R_{jy}) - q_{ij}m_{jy}], \quad (3.8)$$

$$b_{ijz} = \frac{\mu_0}{4\pi} [3p_{ij}(r_{iz} - R_{jz}) - q_{ij}m_{jz}], \quad (3.9)$$

$$p_{ij} = \frac{m_{jx}(r_{ix} - R_{jx}) + m_{jy}(r_{iy} - R_{jy}) + m_{jz}(r_{iz} - R_{jz})}{((r_{ix} - R_{jx})^2 + (r_{iy} - R_{jy})^2 + (r_{iz} - R_{jz})^2)^{5/2}}, \quad (3.10)$$

### 3. Perturbations of singular values of a kernel matrix

$$q_{ij} = \frac{1}{((r_{ix} - R_{jx})^2 + (r_{iy} - R_{jy})^2 + (r_{iz} - R_{jz})^2)^{3/2}}. \quad (3.11)$$

In other words, each component of the magnetic flux density depends on all three components of the magnetic moment of the magnetic dipole. Dependence of  $x$  component is represented by formula (3.12):

$$b_{ijx} = B_{ijxx}m_{jx} + B_{ijxy}m_{jy} + B_{ijxz}m_{jz}, \quad i = 1, \dots, n, \quad j = 1, \dots, m, \quad (3.12)$$

where

$$B_{ijxx} = \frac{\mu_0}{4\pi} \left[ 3 \frac{(r_{ix} - R_{jx})^2}{|\vec{r}_i - \vec{R}_j|^5} - \frac{1}{|\vec{r}_i - \vec{R}_j|^3} \right], \quad (3.13)$$

$$B_{ijxy} = \frac{\mu_0}{4\pi} \left[ 3 \frac{(r_{ix} - R_{jx})(r_{iy} - R_{jy})}{|\vec{r}_i - \vec{R}_j|^5} \right], \quad (3.14)$$

$$B_{ijxz} = \frac{\mu_0}{4\pi} \left[ 3 \frac{(r_{ix} - R_{jx})(r_{iz} - R_{jz})}{|\vec{r}_i - \vec{R}_j|^5} \right], \quad (3.15)$$

represent  $x$  component of magnetic flux density vector depending on  $x$ ,  $y$  and  $z$  component of magnetic dipole moment respectively.

Dependence of  $y$  component is presented by formula (3.16):

$$b_{ijy} = B_{ijyx}m_{jx} + B_{ijyy}m_{jy} + B_{ijyz}m_{jz}, \quad i = 1, \dots, n, \quad j = 1, \dots, m, \quad (3.16)$$

where

$$B_{ijyx} = \frac{\mu_0}{4\pi} \left[ 3 \frac{(r_{ix} - R_{jx})(r_{iy} - R_{jy})}{|\vec{r}_i - \vec{R}_j|^5} \right], \quad (3.17)$$

$$B_{ijyy} = \frac{\mu_0}{4\pi} \left[ 3 \frac{(r_{iy} - R_{jy})^2}{|\vec{r}_i - \vec{R}_j|^5} - \frac{1}{|\vec{r}_i - \vec{R}_j|^3} \right], \quad (3.18)$$

$$B_{ijyz} = \frac{\mu_0}{4\pi} \left[ 3 \frac{(r_{iy} - R_{jy})(r_{iz} - R_{jz})}{|\vec{r}_i - \vec{R}_j|^5} \right], \quad (3.19)$$

represent  $y$  component of the magnetic flux density vector depending on  $x$ ,  $y$  and  $z$  component of the magnetic dipole moment respectively.

In a similar way, the dependence of the  $z$  component of the magnetic flux density can be written using the expression (3.20):

$$b_{ijz} = B_{ijzx}m_{jx} + B_{ijzy}m_{jy} + B_{ijzz}m_{jz}, \quad i = 1, \dots, n, \quad j = 1, \dots, m, \quad (3.20)$$

where

$$B_{ijzx} = \frac{\mu_0}{4\pi} \left[ 3 \frac{(r_{ix} - R_{jx})(r_{iz} - R_{jz})}{|\vec{r}_i - \vec{R}_j|^5} \right], \quad (3.21)$$

$$B_{ijzy} = \frac{\mu_0}{4\pi} \left[ 3 \frac{(r_{iy} - R_{jy})(r_{iz} - R_{jz})}{|\vec{r}_i - \vec{R}_j|^5} \right], \quad (3.22)$$

$$B_{ijzz} = \frac{\mu_0}{4\pi} \left[ 3 \frac{(r_{iz} - R_{jz})^2}{|\vec{r}_i - \vec{R}_j|^5} - \frac{1}{|\vec{r}_i - \vec{R}_j|^3} \right], \quad (3.23)$$

represent  $z$  component of the magnetic flux density vector depending on  $x$ ,  $y$  and  $z$  component of the magnetic dipole moment respectively.

Note that a component  $g$ ,  $g \in \{x, y, z\}$ , of the magnetic flux density vector depends on a component  $h$ ,  $h \in \{x, y, z\}$ , of magnetic dipole moment in the same way as the the component  $h$  of the magnetic flux density vector depends on component  $g$  of the magnetic dipole moment.

Separation of information on orientations of single component magnetometers is done by placement of that information into one matrix. This is achieved through the factorization of kernel matrix  $L$  into the product of matrix  $B$  that contains information on positions of both magnetometers and magnetic dipoles and matrix  $D$  that models sensor orientations.

Based on these notations, kernel matrix  $L_{n \times 3m}$  can be written as a product of two matrices,  $D$  and  $B$ , where matrix  $D$  contains information only on sensors orientations and matrix  $B$  contains information on dipoles and sensors positions:

$$[L]_{n \times 3m} = [D]_{n \times 3n} \cdot [B]_{3n \times 3m}, \quad (3.24)$$

where

$$[D] = \begin{bmatrix} d_{1x} & d_{1y} & d_{1z} & 0 & 0 & 0 & 0 & 0 & 0 & 0 & 0 & 0 \\ 0 & 0 & 0 & d_{2x} & d_{2y} & d_{2z} & 0 & 0 & 0 & 0 & 0 & 0 \\ 0 & 0 & 0 & 0 & 0 & 0 & . & . & . & 0 & 0 & 0 \\ 0 & 0 & 0 & 0 & 0 & 0 & 0 & 0 & 0 & d_{nx} & d_{ny} & d_{nz} \end{bmatrix}_{n \times 3n}, \quad (3.25)$$

$$[B] = \begin{bmatrix} B_{11xx} & B_{11xy} & B_{11xz} & . & . & . & B_{1mxx} & B_{1mxy} & B_{1mxz} \\ B_{11yx} & B_{11yy} & B_{11yz} & . & . & . & B_{1myx} & B_{1myy} & B_{1myz} \\ B_{11zx} & B_{11zy} & B_{11zz} & . & . & . & B_{1mzx} & B_{1mzy} & B_{1mzz} \\ . & . & . & & & & & & \\ . & . & . & & & & & & \\ . & . & . & & & & & & \\ B_{n1xx} & B_{n1xy} & B_{n1xz} & . & . & . & B_{nmxx} & B_{nmxy} & B_{nmxz} \\ B_{n1yx} & B_{n1yy} & B_{n1yz} & . & . & . & B_{nmyx} & B_{nmyy} & B_{nmyz} \\ B_{n1zx} & B_{n1zy} & B_{n1zz} & . & . & . & B_{nmzx} & B_{nmzy} & B_{nmzz} \end{bmatrix}_{3n \times 3m}. \quad (3.26)$$

Elements of matrix  $B$  are defined in formulas (3.13)-(3.15), (3.17)-(3.19) and (3.21)-(3.23). Note that matrix  $B$  in decomposition (3.24) corresponds to the kernel matrix of the linear inverse problem using three-component measurements performed at the same points as single component measurements.

Besides multiplicative, perturbations of a kernel matrix in case of single component measurements could also be studied as additive. Kernel matrix could be according to (3.24) written as  $L = D \cdot B$ . After variations of sensors orientations, kernel matrix becomes  $L' = D' \cdot B$ , clearly showing the source of perturbations already in a notation. Perturbation matrix  $\Delta L$  in this case is  $\Delta L = L' - L = D' \cdot B - D \cdot B = (D' - D) \cdot B = \Delta D \cdot B$ .

#### Three-axis devices

When measuring three orthogonal components  $x$ ,  $y$  and  $z$  of magnetic flux density  $\vec{b}$ , produced by magnetic dipoles of no assumed orientation (three unknowns per one dipole), the kernel matrix corresponding to this linear inverse problem can be decomposed in the following way:

$$[L]_{3n \times 3m} = [D]_{3n \times 3n} \cdot [B]_{3n \times 3m}, \quad (3.27)$$

where matrix  $B$  is defined in (3.26) and matrix  $D$  is of the diagonal form:

$$[D] = \begin{bmatrix} d_{1x} & 0 & 0 & 0 & 0 & 0 & 0 & 0 & 0 \\ 0 & d_{1y} & 0 & 0 & 0 & 0 & 0 & 0 & 0 \\ 0 & 0 & d_{1z} & 0 & 0 & 0 & 0 & 0 & 0 \\ 0 & 0 & 0 & . & 0 & 0 & 0 & 0 & 0 \\ 0 & 0 & 0 & 0 & . & 0 & 0 & 0 & 0 \\ 0 & 0 & 0 & 0 & 0 & . & 0 & 0 & 0 \\ 0 & 0 & 0 & 0 & 0 & 0 & d_{nx} & 0 & 0 \\ 0 & 0 & 0 & 0 & 0 & 0 & 0 & d_{ny} & 0 \\ 0 & 0 & 0 & 0 & 0 & 0 & 0 & 0 & d_{nz} \end{bmatrix}_{3n \times 3n}, \quad (3.28)$$

and  $d_{1x} = d_{1y} = d_{1z} = \dots = d_{nx} = d_{ny} = d_{nz} = 1$ . Matrix  $D$  is an identity matrix and the expression (3.27) becomes  $[L]_{3n \times 3m} = [B]_{3n \times 3m}$ . Lack of measurement of a certain component results in placing a zero in an appropriate place in the matrix  $D$ , further producing a zero row in kernel matrix and thus excluding of this row from the matrix.

Let us observe counterclockwise rotations of sensors directions by an angle  $\theta_x$ ,  $\theta_y$  and  $\theta_z$ , respectively around  $x$ ,  $y$  and  $z$  axis of the right Cartesian coordinate system. One directional vector  $\vec{d} = d_x \hat{x} + d_y \hat{y} + d_z \hat{z}$  becomes after rotations  $\vec{d}' = d'_x \hat{x} + d'_y \hat{y} + d'_z \hat{z}$ , where

$$d'_x = d_x \cos \theta_y \cos \theta_z + d_y (\sin \theta_x \sin \theta_y \cos \theta_z - \cos \theta_x \sin \theta_z) + d_z (\cos \theta_x \sin \theta_y \cos \theta_z + \sin \theta_x \sin \theta_z),$$

$$d'_y = d_x \cos \theta_y \sin \theta_z + d_y (\cos \theta_x \cos \theta_z + \sin \theta_x \sin \theta_y \sin \theta_z) + d_z (-\sin \theta_x \cos \theta_z + \cos \theta_x \sin \theta_y \sin \theta_z)$$

and

$$d'_z = -d_{1x} \sin \theta_y + d_y \sin \theta_x \cos \theta_y + d_z \cos \theta_x \cos \theta_y.$$

We might choose a differently oriented set of mutually perpendicular sensors. For that purpose, we rotate three component sensors at one point for the angles  $\theta_x$ ,  $\theta_y$  and  $\theta_z$ , respectively around  $x$ ,  $y$  and  $z$  axis of the right Cartesian coordinate system. This rotation can be simply written as a left preconditioner of a kernel matrix in form of a rotational matrix  $R$  of dimensions  $3n \times 3n$  and of the form:

$$[R] = \begin{bmatrix} r_{11}^1 & r_{12}^1 & r_{13}^1 & 0 & 0 & 0 & 0 & 0 & 0 \\ r_{21}^1 & r_{22}^1 & r_{23}^1 & 0 & 0 & 0 & 0 & 0 & 0 \\ r_{31}^1 & r_{32}^1 & r_{33}^1 & 0 & 0 & 0 & 0 & 0 & 0 \\ 0 & 0 & 0 & . & . & . & 0 & 0 & 0 \\ 0 & 0 & 0 & . & . & . & 0 & 0 & 0 \\ 0 & 0 & 0 & . & . & . & 0 & 0 & 0 \\ 0 & 0 & 0 & 0 & 0 & 0 & r_{11}^n & r_{12}^n & r_{13}^n \\ 0 & 0 & 0 & 0 & 0 & 0 & r_{21}^n & r_{22}^n & r_{23}^n \\ 0 & 0 & 0 & 0 & 0 & 0 & r_{31}^n & r_{32}^n & r_{33}^n \end{bmatrix}_{3n \times 3n}, \quad (3.29)$$

where

$$\begin{aligned} r_{11}^i &= \cos\theta_y^i \cos\theta_z^i, \quad r_{12}^i = \cos\theta_y^i \sin\theta_z^i, \quad r_{13}^i = -\sin\theta_y^i, \quad r_{21}^i = \sin\theta_x^i \sin\theta_y^i \cos\theta_z^i - \cos\theta_x^i \sin\theta_z^i, \\ r_{22}^i &= \cos\theta_x^i \cos\theta_z^i + \sin\theta_x^i \sin\theta_y^i \sin\theta_z^i, \quad r_{23}^i = \sin\theta_x^i \cos\theta_y^i, \\ r_{31}^i &= \cos\theta_x^i \sin\theta_y^i \cos\theta_z^i + \sin\theta_x^i \sin\theta_z^i, \quad r_{32}^i = -\sin\theta_x^i \cos\theta_z^i + \cos\theta_x^i \sin\theta_y^i \sin\theta_z^i, \\ r_{33}^i &= \cos\theta_x^i \cos\theta_y^i. \end{aligned}$$

Now, the kernel matrix becomes  $[L']_{3n \times 3m} = [R]_{3n \times 3n} \cdot [D]_{3n \times 3n} \cdot [B]_{3n \times 3m}$ , and taking into account that matrix  $D$  is an identity matrix, the kernel matrix after rotations is simplified to:

$$[L']_{3n \times 3m} = [R]_{3n \times 3n} \cdot [L]_{3n \times 3m}, \quad (3.30)$$

allowing rotations to be directly used as preconditioners. Matrix  $R$  defined by (3.29) is a unitary matrix.

Additive perturbations are in this case defined through the matrix  $\Delta L$  and can be written in the following form:  $\Delta L = L' - L = R \cdot L - L = (R - I) \cdot L$ .

Representation of a kernel matrix as a product of two matrices enables to apply special algorithms for computing the singular value decomposition of a product of two matrices without explicitly forming the product [62]. The algorithm produces results which are similar in accuracy to those obtained by explicitly forming the product of matrices and applying the standard algorithm. With respect to the accuracy of computing very small singular values, the algorithm presented in [62] shows the superiority comparing to the standard procedure. As a useful alternative for computing the SVD of a product of two matrices, it is to be preferred when explicit formation of the product would cause a serious loss of information in finite precision arithmetic. The algorithm is based on the Jacobi-like method according to Kogbetliantz [63] and uses plane rotations applied to two matrices separately. A proof of the product singular value decomposition is provided in [64].

Furthermore, influencing the sensitivity of linear inverse problems solution can be done through the scaling and equilibration (see section 2.1.2). Scaling can be done by simple preconditioning of a kernel matrix. Decomposition of a kernel matrix in case of single component devices given by formula (3.24) enables the left preconditioning relying just on the orientations of single component measurements. However, a very specific structure of matrix  $D$  (at most three elements in a row are nonzero (formula 3.25)) has to be taken into account when performing preconditioning in case of single component measurements.

The concept of preconditioning using orientations of single component measuring devices can also be used to achieve diagonal dominance in a system of linear equations. Strictly diagonally dominant matrices are usually well-conditioned and the solution of linear systems with such matrices as kernel matrices is stable [36]. If a matrix is strictly row diagonally dominant, then that matrix is nonsingular (Lévy-Desplanques Theorem). Furthermore, Gaussian elimination is stable for the inverse of diagonally dominant matrix [65]. Also computation of singular values of diagonally dominant matrices, including zero ones if any, can be performed with high relative accuracy [66]. Besides the diagonally dominant matrix, using the orientations of single component measurements, a block diagonal dominance property can be achieved. The features of these matrices are described in [67].

In all the cases, orientations of single component measuring devices are directly used as left preconditioners.

### 3.3 Perturbation bounds for singular values

Variations of single axis or three-axis measurement devices do not affect dimensions of a kernel matrix, but only its elements. Therefore, it is possible to view variations in sensors orientations as kernel matrix perturbations. These perturbations cause the perturbations in singular values of a kernel matrix. It is therefore important to be able to assess the effects of matrix perturbations on singular values and singular vectors.

One way of studying perturbations of singular values of a matrix includes perturbation bounds. A perturbation bound gives an upper bound on the difference between the perturbed singular value  $\sigma'_i$  and its original  $\sigma_i$  in terms of a norm of a perturbation matrix.

Let  $L$  be an  $n \times m$  matrix of full column rank,  $n \geq m$ . Its singular values are

$$\sigma_1 \geq \sigma_2 \geq \dots \geq \sigma_m. \quad (3.31)$$

If matrix  $L$  is perturbed, its singular values are

$$\sigma'_1 \geq \sigma'_2 \geq \dots \geq \sigma'_m, \quad (3.32)$$

and according to Weyl's theorem [68]

$$|\sigma_i - \sigma'_i| \leq \|E\|_2, \quad i = 1, \dots, m. \quad (3.33)$$

In this theorem, there is no restriction for the error size. The theorem is true for any perturbation matrix  $E$ . According to this theorem, no singular value can change more than the  $L_2$  norm of its perturbation matrix.

This theorem has one disadvantage: the same bound holds for all singular values. This means that this bound could be very broad and imprecise for very small singular values.

Starting from this theorem and using the inequalities of singular values of product of matrices [69], Di Lena et al. derive a general theorem of relative perturbation bounds [70].

If  $\text{rank}(L) = n$  (Theorem 1.1 in [70]), then

$$|\sigma_i - \sigma'_i| \leq \sigma_i \|L^+ \cdot E\|, \quad i = 1, \dots, m, \quad (3.34)$$

and if  $\text{rank}(L) = m$ , then

$$|\sigma_i - \sigma'_i| \leq \sigma_i \|E \cdot L^+\|, \quad i = 1, \dots, m. \quad (3.35)$$

In contrast to Weyl (3.33), Di Lena et al. give two different definitions of perturbation bounds for under and overdetermined linear inverse problems. As being dependent on the singular value that is being perturbed, the bounds (3.34) and (3.35) are defined for each singular value individually. Furthermore, they depend not only on the perturbation matrix, but also on the pseudoinverse of the original matrix, too.

Another theorem that holds for the sum of perturbations of all singular values of a matrix is Mirsky's theorem [71]:

$$\sqrt{\sum_i (\sigma_i - \sigma'_i)^2} \leq \|E\|_F, \quad i = 1, \dots, m, \quad (3.36)$$

where index F denotes the Frobenius norm of a perturbation matrix  $E$ . Like the Weyl's theorem, this theorem has also no restrictions for the perturbation matrix  $E$ . It is less precise than Weyl's theorem, but is very useful since the Frobenius norm is easy to calculate.

### 3.4 Perturbation expansion of singular values

Besides the perturbation bounds, perturbation expansion is another way of studying the perturbations of singular values. A perturbation expansion provides an approximation of the perturbed singular value and is proposed in [72]. Let  $L$  be an  $n \times m$  matrix of full column rank,  $n \geq m$ . Its singular values are as in (3.31). If  $L' = L + E$  is a perturbed matrix then its singular values are as in (3.32).

A perturbed singular value can be represented using the following expansion:

$$\sigma_i'^2 = (\sigma_i + \varepsilon_i)^2 + \eta_i^2, \quad i = 1, \dots, m, \quad (3.37)$$

where

$$|\varepsilon_i| \leq \|P \cdot E\|, \quad (3.38)$$

$$\inf[(I - P) \cdot E] \leq \eta_i \leq \|(I - P) \cdot E\|, \quad (3.39)$$

and  $P$  denotes the orthogonal projection onto the column space of  $L$ ;  $\inf[(I - P) \cdot E]$  is the smallest singular value of the matrix  $(I - P) \cdot E$ . Projection matrix  $P$  is equal to  $P = L \cdot L^+$ . In the case of linearly independent columns projection matrix becomes  $P = L \cdot (L^T \cdot L)^+ \cdot L^T$ , where  $T$  denotes the transpose of a matrix. Projection matrix  $P$  satisfies two properties: it is idempotent ( $P^2 = P$ ) and symmetric ( $P^T = P$ ). Difference of the identity matrix and the projection matrix,  $I - P$ , projects onto the left nullspace of  $L$  (space perpendicular to the column space of  $L$ ).



If we suppose that  $\sigma_i$  is very small approaching zero, then the perturbed singular value will be  $\sigma'_i = \varepsilon_i^2 + \eta_i^2$ . As  $m$  grows,  $\varepsilon_i^2$  will on the average be of order unity, while  $\eta_i^2$  will be of order  $m$ . Instead of a zero singular value, we will have a nonzero singular value that tends to grow as  $\sqrt{m}$ . So, small singular values tend to increase under perturbation and the increment is proportional to  $\sqrt{m}$  [72].

In case of kernel matrix  $L$  of dimensions  $n \times m$  and full row rank,  $m \geq n$ ,  $P \cdot E$  in (3.38) and (3.39) is replaced by  $E \cdot R$ , where  $R$  is the orthogonal projection onto the row space of  $L$ .

#### 3.5 Mathematical definition of the case when random variations of single-axis sensor orientations increase the smallest singular value of a kernel matrix with the probability equal to one

Random variations of sensor orientations can provide a better condition for the linear inverse problem and, consequently, more stable inverse solutions [5]. Sensor arrays with varied sensor directions are compared with arrays using perfectly in parallel aligned sensors. Let a sensor array consist of  $12 \times 12$  equidistantly placed single-axis sensors in the area  $(x_{\min}, x_{\max}) = (0, 0.2\text{m})$  and  $(y_{\min}, y_{\max}) = (0, 0.2\text{m})$ . The source grid consists of  $10 \times 10$  dipole sources of no predefined direction, in the area  $(x_{\min}, x_{\max}) = (-0.02, 0.22\text{m})$  and  $(y_{\min}, y_{\max}) = (-0.02, 0.22\text{m})$ , 9mm below the sensor array as in [5]. When sensor directions are randomly varied, relative changes of the condition number with respect to  $L_2$  norm are denoted by  $\Delta CN = CN(L')/CN(L)$ , where  $CN(L)$  is the condition number for the default sensor directions without variations and  $CN(L')$  is the condition number of a lead field matrix with randomly varied sensor directions. Random variations are done for the angles of  $0.05^\circ$ ,  $0.5^\circ$ ,  $1^\circ$ ,  $2.5^\circ$ ,  $5^\circ$ ,  $10^\circ$ ,  $15^\circ$ ,  $20^\circ$  and  $25^\circ$  away from the  $z$  axis in any direction with respect to the projection in  $xy$  plane. Mean values of  $\Delta CN$  obtained in 100 runs for different angles of variations are presented in Fig. 3.1a. Fig. 3.1b presents the behavior of  $\Delta \sigma_{\max} = \sigma_{\max}(L')/\sigma_{\max}(L)$  and  $\Delta \sigma_{\min} = \sigma_{\min}(L')/\sigma_{\min}(L)$  in blue and red respectively. This figure shows that that the decrement of the condition number with respect to the  $L_2$  norm is mostly due to the increment of the smallest singular value, while the largest singular value has negligible variations and practically no influence on changes of the condition number with respect to the  $L_2$  norm.

Besides the variations in orientations, small variations of sensors  $z$  positions of planar mono-axial arrays lead to a better condition of a linear inverse problem [5]. Any change in a position or orientation of single-axis sensors in sensor arrays can be considered as perturbation in a kernel matrix of the corresponding linear inverse problem.

It is not always the case that the perturbations in sensor orientations increase the smallest singular value and therefore lead to a better conditioned linear inverse problem. Therefore, it is needed to strictly mathematically define the case when random variations of single-axis sensor orientations increase the smallest singular value of a kernel matrix with the probability equal to one.

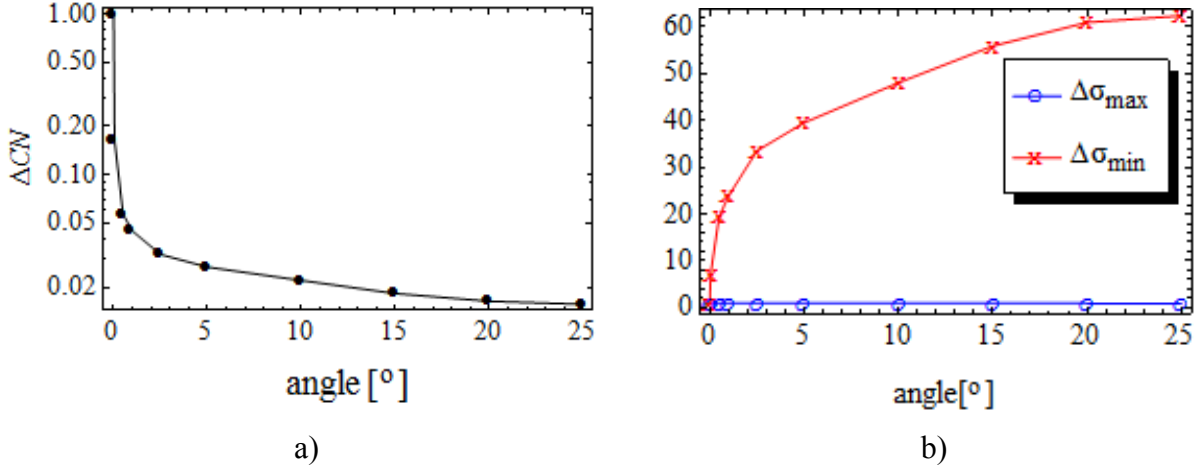


Fig. 3.1 – Mean values of  $\Delta CN$  in logarithmic representation obtained in 100 runs (a) and  $\Delta \sigma_{\max}$  and  $\Delta \sigma_{\min}$  in blue and red respectively (b) for different angles of single-axis sensor directions variations about the  $z$  axis.

When applying perturbation expansion (3.37) to the smallest singular value of a matrix, then a perturbed minimal singular value can be represented using the following expansion:

$$\sigma'_{\min}{}^2 = (\sigma_{\min} + \varepsilon)^2 + \eta^2, \quad (3.40)$$

where  $|\varepsilon| \leq \|P \cdot E\|$  and  $\inf[(I - P) \cdot E] \leq \eta \leq \|(I - P) \cdot E\|$ . Matrix  $E$  denotes a perturbation matrix defined as  $E = L' - L$ , where  $L$  denotes a kernel matrix when all the sensors are aligned perfectly in parallel and  $L'$  a kernel matrix when orientations of sensors are randomly varied. Matrices  $L$ ,  $L'$  and  $E$  are of dimensions  $n \times m$ ,  $n \geq m$ . Projection matrix  $P$  is equal to  $P = L \cdot L^+$  and satisfies conditions of idempotence and symmetry. A difference  $I - P$  projects onto the space perpendicular to the column space of  $L$ .

Expansion (3.40) represents a circle in  $\varepsilon$ – $\eta$  coordinate system characterized by a radius  $\sigma'_{\min}$  and a center at  $(0, -\sigma_{\min})$ . Assuming that  $\sigma_{\min} > 0$ , center of a circle belongs to the negative part of  $\varepsilon$ –axis. The absence of changes in a singular value after perturbations is presented by the circle of the radius  $\sigma_{\min}$  (see Fig. 3.2). Since  $\varepsilon$  could be either positive or negative and  $\eta$  only positive (assuming that singular values of the matrix  $(I - P) \cdot E$  are larger or equal to zero), then only the first and second quadrant are considered, Fig. 3.2.

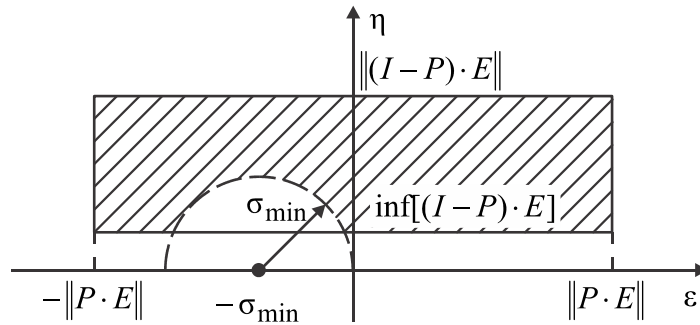


Fig. 3.2 – Representation of perturbation expansion (3.40) in the  $\varepsilon$ – $\eta$  coordinate system. The area where we can expect the increment of the smallest singular value is hatched.

### 3. Perturbations of singular values of a kernel matrix

With respect to the formula (3.40) and Fig. 3.2, the increment of the minimal singular value after perturbations corresponds to the area outside the circle  $\sigma_{\min}^2 = (\sigma_{\min} + \varepsilon)^2 + \eta^2$  (hatched area). The perturbed minimal singular value will be smaller than the corresponding singular value before perturbations in the area inside the circle  $\sigma_{\min}^2 = (\sigma_{\min} + \varepsilon)^2 + \eta^2$ .

There are two possible cases:

$$\text{Case I: } \inf((I - P) \cdot E) \leq \|P \cdot E\|$$

In this case, in order to get the increment of the smallest singular value with the probability equal to one, the minimal singular value of unperturbed matrix has to satisfy the following condition:

$$\sigma_{\min} \leq \inf((I - P) \cdot E). \quad (3.41)$$

A very small minimal singular value of kernel matrix corresponds to the case of very ill conditioned linear inverse problem. It is expected that in these cases random variations of sensor orientations always improve the condition of linear inverse problems.

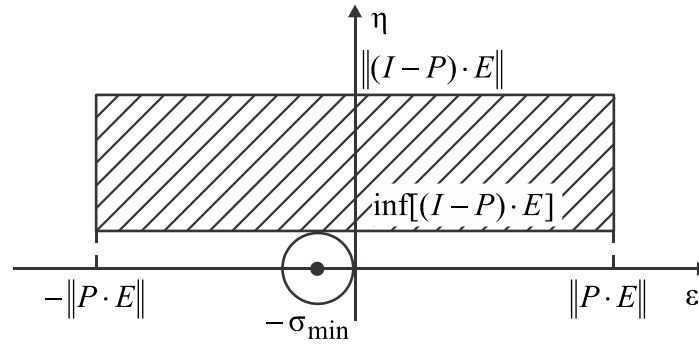


Fig. 3.3 – The case of increasing the smallest singular value with the probability equal to one, when  $\inf((I - P) \cdot E) \leq \|P \cdot E\|$ .

$$\text{Case II: } \inf((I - P) \cdot E) \geq \|P \cdot E\|$$

In order to get the probability of increasing the smallest singular value equal to one, the minimal singular value has in this case to satisfy the following condition (triangle ABC in Fig. 3.4):

$$\sigma_{\min}^2 \leq (\sigma_{\min} - \|P \cdot E\|)^2 + \inf^2((I - P) \cdot E). \quad (3.42)$$

After simple mathematical calculations, this condition becomes

$$\sigma_{\min} \leq \frac{\|P \cdot E\|}{2} + \frac{\inf^2((I - P) \cdot E)}{2\|P \cdot E\|}. \quad (3.43)$$

When kernel matrix  $L$  is of dimensions  $n \times m$ ,  $m \geq n$ , then the perturbation expansion (3.40) is valid for the bounds (3.38) and (3.39), where matrix product  $P \cdot E$  is replaced by  $E \cdot R$ .  $R$  denotes an orthogonal projection onto the row space of  $L$ .

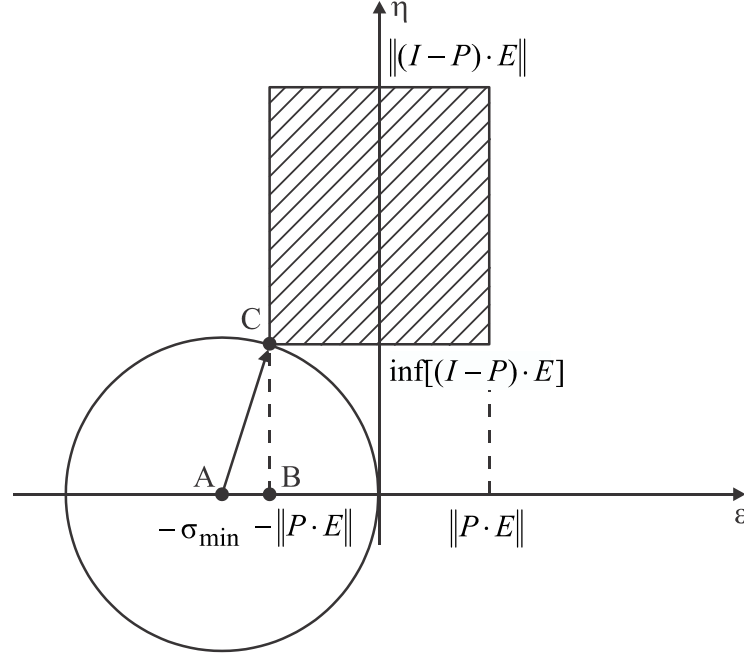


Fig. 3.4 – Case of increasing the smallest singular value with the probability equal to one, in case of  $\inf((I-P) \cdot E) \geq \|P \cdot E\|$ .

### 3.6 Improving bounds of one variable in perturbation expansion of singular values

As mentioned, there are two ways of studying perturbations of the smallest singular value, including use of perturbation bounds and perturbation expansion. Perturbation bounds give lower and upper bounds for the singular value after perturbation, without information about its structure. The perturbation expansion yields an approximation of the perturbed singular values of the matrix. Perturbation bounds can be used for improving the accuracy of perturbation expansion. Derivation of sharper perturbation bounds in perturbation expansion enables more precise calculation of the probability of obtaining increments or decrements in the smallest singular value after random perturbations in elements of a kernel matrix.

Let  $L$  be an  $n \times m$  matrix of full column rank,  $n \geq m$ . Its singular values are  $\sigma_1 \geq \sigma_2 \geq \dots \geq \sigma_m$ . Matrix  $L$  is additively perturbed to a matrix  $L'$ ,  $L' = L + E$ . Singular values of the perturbed matrix are  $\sigma'_1 \geq \sigma'_2 \geq \dots \geq \sigma'_m$ . The absolute perturbation bound is given by Weyl's theorem [68],  $|\sigma_i - \sigma'_i| \leq \|E\|_2$ ,  $i = 1, 2, \dots, m$ . This inequality is valid for any matrix  $E$ . Relative perturbation bounds are given by Di Lena et al. [70]: if  $\text{rank}(L) = n$ , then (3.34) and if  $\text{rank}(L) = m$  by (3.35).

Studying perturbations of singular values using perturbation expansion is proposed in [72]. A perturbed minimal singular value can be represented using the expansion (3.40), where  $\epsilon$  and  $\eta$  satisfy the conditions (3.38) and (3.39) respectively and  $P$  denotes the orthogonal projection onto the column space of  $L$ ;  $\inf[(I-P) \cdot E]$  is the smallest singular value of the matrix  $(I-P) \cdot E$ .

Expansion (3.40) represents a circle in  $\varepsilon$ – $\eta$  coordinate system characterized by a radius  $\sigma'_{\min}$  and with its center at  $(0, -\sigma_{\min})$  (see Fig. 3.5).

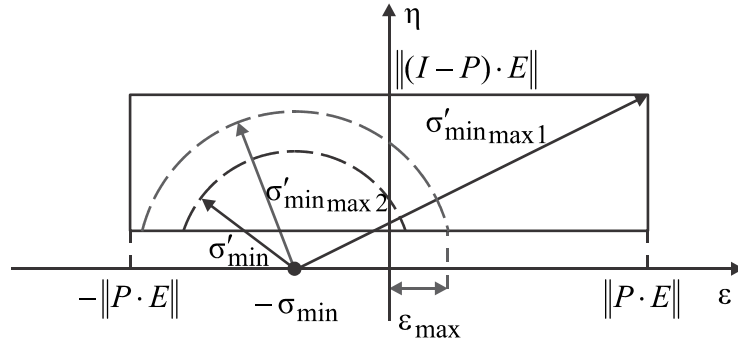


Fig. 3.5 – Representation of perturbation expansion (3.40) in the  $\varepsilon$ – $\eta$  coordinate system.

According to [72], the maximal perturbation of the singular value  $\sigma_{\min}$  is

$$\sigma'_{\min_{\max 1}} = \sqrt{(\sigma_{\min} + \|P \cdot E\|)^2 + \|(I - P) \cdot E\|^2}, \quad (3.44)$$

corresponding to the upper right-hand corner of the rectangle in Fig. 3.5. According to the relative perturbation bound (3.35), the maximum of the perturbed minimal singular value is

$$\sigma'_{\min_{\max 2}} = \sigma_{\min} (1 + \|E \cdot L^+\|). \quad (3.45)$$

Maximal perturbation corresponds to the right-hand side of the  $\varepsilon$ – $\eta$  coordinate system (see Fig. 3.5), where values of  $\varepsilon$  are positive. Therefore, and with respect to (3.45), the upper bound of  $\varepsilon$ ,  $\varepsilon_{\max}$ , has to satisfy

$$\varepsilon_{\max} \leq \sigma_{\min} \cdot \|E \cdot L^+\|. \quad (3.46)$$

The upper bound (3.46) is smaller or equal to the upper bound given in [72] if the perturbation matrix satisfies

$$\|E \cdot L^+\| \leq \|L^+ \cdot E\|. \quad (3.47)$$

**Proof.** Perturbation matrix satisfies condition (3.47). Multiplication of both sides by  $\sigma_{\min}(L) > 0$  yields

$$\sigma_{\min}(L) \cdot \sigma_{\max}(E \cdot L^+) \leq \sigma_{\min}(L) \cdot \sigma_{\max}(L^+ \cdot E). \quad (3.48)$$

Let us now consider two matrices  $A$  and  $B$  of dimensions  $n \times m$  and  $m \times l$ , respectively. If  $n \geq m$ , then the minimal singular value of matrix  $A$ , the maximal singular value of matrix  $B$  and the maximal singular value of the product  $A \cdot B$  satisfy the inequality [73, their page 616]

$$\sigma_{\min}(A) \cdot \sigma_{\max}(B) \leq \sigma_{\max}(A \cdot B).$$

Since the matrix  $L$  satisfies the condition  $n \geq m$ , the same inequality holds for  $A = L$  and  $B = L^+ \cdot E$ . Therefore, we obtain

$$\sigma_{\min}(L) \cdot \sigma_{\max}(L^+ \cdot E) \leq \sigma_{\max}(L \cdot (L^+ \cdot E)). \quad (3.49)$$

Since the matrix product is associative,  $L \cdot (L^+ \cdot E) = (L \cdot L^+) \cdot E$ , inequality (3.47) becomes

$\sigma_{\min}(L) \cdot \sigma_{\max}(L^+ \cdot E) \leq \sigma_{\max}((L \cdot L^+) \cdot E)$ . Since  $L \cdot L^+$  is a projection matrix onto a column space of  $L$ ,  $P = L \cdot L^+$ , we obtain

$$\sigma_{\min}(L) \cdot \sigma_{\max}(L^+ \cdot E) \leq \sigma_{\max}(P \cdot E). \quad (3.50)$$

Combining inequalities (3.48), (3.49) and (3.50), we obtain  $\varepsilon_{\max} \leq \|P \cdot E\|$ . This ends the proof.

For a matrix  $L$  of dimensions  $n \times m$ ,  $m \geq n$ , the perturbation expansion (3.40) is valid for the bounds (3.38) and (3.39), where matrix product  $P \cdot E$  is replaced by  $E \cdot R$  and  $R$  is the orthogonal projection onto the row space of  $L$ .

According to the relative perturbation bound (3.34), the perturbed singular value is maximal in this case,

$$\sigma'_{\min_{\max} 3} = \sigma_{\min}(1 + \|L^+ \cdot E\|), \quad (3.51)$$

allowing the value of  $\varepsilon_{\max}$  to reach

$$\varepsilon_{\max} \leq \sigma_{\min} \cdot \|L^+ \cdot E\|. \quad (3.52)$$

The upper bound (3.52) is smaller or equal to the upper bound given in [72] if the perturbation matrix satisfies

$$\|L^+ \cdot E\| \leq \|E \cdot L^+\|. \quad (3.53)$$

**Proof.** Perturbation matrix satisfies condition (3.53). Multiplication of both sides by  $\sigma_{\min}(L) > 0$  yields

$$\sigma_{\min}(L) \cdot \sigma_{\max}(L^+ \cdot E) \leq \sigma_{\min}(L) \cdot \sigma_{\max}(E \cdot L^+). \quad (3.54)$$

Let us observe two matrices,  $A$  and  $B$ , of dimensions  $n \times m$  and  $m \times l$ , respectively. If  $m \leq l$ , the maximal singular value of matrix  $A$ , the minimal singular value of matrix  $B$  and the maximal singular value of the product  $A \cdot B$  satisfy the inequality [73, their page 616]

$$\sigma_{\max}(A) \cdot \sigma_{\min}(B) \leq \sigma_{\max}(A \cdot B).$$

Matrix  $L$  has a larger number of columns than rows, so the same inequality holds for  $A = E \cdot L^+$ ,  $B = L$ . As a consequence, we obtain

$$\sigma_{\max}(E \cdot L^+) \cdot \sigma_{\min}(L) \leq \sigma_{\max}((E \cdot L^+) \cdot L). \quad (3.55)$$

Since the matrix product is associative,  $(E \cdot L^+) \cdot L = E \cdot (L^+ \cdot L)$ , inequality (3.55) becomes

$\sigma_{\max}(E \cdot L^+) \cdot \sigma_{\min}(L) \leq \sigma_{\max}(E \cdot (L^+ \cdot L))$ . Since  $L^+ \cdot L$  is a projection matrix onto a row space of  $L$ ,  $R = L^+ \cdot L$ , we obtain

$$\sigma_{\max}(E \cdot L^+) \cdot \sigma_{\min}(L) \leq \sigma_{\max}(E \cdot R). \quad (3.56)$$

Inequalities (3.60), (3.61) and (3.62) result in  $\varepsilon_{\max} \leq \|E \cdot R\|$ . This ends the proof.

Since random variations of sensor orientations produce random perturbations in elements of a kernel matrix, and therefore perturbations in its singular values, they can improve or worse the

condition of corresponding linear inverse problem. Changes in the condition number with respect to  $L_2$  norm are usually due to the changes in the smallest singular value. Therefore, calculation of probability of obtaining increments or decrements in the smallest singular value after random perturbations in elements of a kernel matrix becomes crucial. It can be done by means of geometric probability. The area where we expect an increment belongs to the rectangle but outside a circle (hatched area in Fig. 3.2). This area directly depends on the bound of  $\varepsilon$ . Hence, a derived sharper perturbation bounds contributes to the more precise calculation of probability of increasing the smallest singular value after random perturbations in elements of a kernel matrix.

In case of non-uniform distribution of variables  $\varepsilon$  and  $\eta$ , parameters of their distribution functions can be determined after equalizing probabilities obtained by means of geometrical probability taking into account assumed distribution functions and probabilities obtained using the numerical simulations.

### 3.7 Perturbation of singular values due to deleting a column or a row of a kernel matrix

#### 3.7.1 Introduction

Changing dimensions of a kernel matrix influences its condition number with respect to the  $L_2$  norm. When performing numerical simulations, one can see that a change in one dimension (number of rows or columns) of a kernel matrix can sometimes increase and sometimes decrease the condition number with respect to the  $L_2$  norm. Furthermore, this increment/decrement of the condition number is dependent on over- or underdetermination of the linear inverse problem. It is therefore worth strictly deriving the conditions under which the condition number is improved. The following three corollaries define these conditions.

#### 3.7.2 Influence of excluding sources on $CN$ with respect to the $L_2$ norm in overdetermined linear inverse problems

Source grid parameters are adapted to improve the condition of the magnetostatic linear inverse problem of estimating nanoparticle distributions [50]. Numerical simulations show that if a sparse source grid with equal or fewer sources can be practically applied, then the condition can be considerably improved by further reducing the number of sources. A relevance of this finding for various linear inverse problems in magnetic and other applications is derived in this corollary.

Let us observe a lead field matrix  $L_{n \times m}$ ,  $n > m$ . Its singular values are ordered as

$$\sigma_1 \geq \sigma_2 \geq \dots \geq \sigma_m. \quad (3.57)$$

A matrix  $L'$  resulting from the deletion of a column  $k$ ,  $1 \leq k \leq m$ , have singular values  $\sigma'_1 \geq \sigma'_2 \geq \dots \geq \sigma'_{m-1}$ .

These values interlace with those of  $L$ , Theorem 5.12, [74]:

$$\sigma_1 \geq \sigma'_1 \geq \sigma_2 \geq \sigma'_2 \dots \geq \sigma'_{m-1} \geq \sigma_m. \quad (3.58)$$

Condition number with respect to the  $L_2$  norm of a lead field matrix  $L$  is  $CN = \sigma_1/\sigma_m$ . The condition number of a matrix  $L'$  is  $CN' = \sigma'_1/\sigma'_{m-1}$ . According to (3.58)  $\sigma'_1/\sigma'_{m-1} \leq \sigma_1/\sigma'_{m-1}$  and  $\sigma_1/\sigma'_{m-1} \leq \sigma_1/\sigma_m = CN$ , we derive that the condition number with respect to the  $L_2$  norm of the lead field matrix  $L'$  resulting from the deletion of column  $k$  of matrix  $L$  is always smaller or equal to the original condition number:

$$CN' \leq CN. \quad (3.59)$$

*Corollary 1:* In overdetermined linear inverse problems, decreasing number of sources leads to a smaller condition number with respect to the  $L_2$  norm. In the limiting case, this condition number can remain the same.

The same effect on the inverse average decay of singular values of a kernel matrix is shown in the results of numerical simulations in [50].



### 3.7.3 Influence of excluding sensors on $CN$ with respect to the $L_2$ norm in underdetermined linear inverse problems

Let a lead field matrix  $L$  be of dimensions  $n \times m$ ,  $n < m$ . Let a matrix  $L'$  be obtained from  $L$  by deleting  $\tilde{n}$  rows of  $L$ . Now matrix  $L'$  has  $n' = n - \tilde{n}$  rows and  $m' = m$  columns. Define  $k$  as a rank of a matrix  $L'$ ,  $k = n'$ . Let  $\sigma'_1 \geq \sigma'_2 \dots \geq \sigma'_k \geq 0$  denote the singular values of a matrix  $L'$ . According to the rectangular Cauchy interlacing theorem (Theorem 23 in [75]), we have:

$$\sigma_j \geq \sigma'_j \text{ for } j = 1, \dots, k. \quad (3.60)$$

Furthermore, the number of positive singular values of  $L'$  is bounded from below by:

$$l = r - (\tilde{m} + \tilde{n}) = r - \tilde{n}, \quad (3.61)$$

where  $r$  is a rank of  $L$ ,  $r = n$ . Consequently,  $l \leq k$ , and if  $l \geq 1$ , the first  $l$  singular values of  $L'$  satisfy the lower bounds:

$$\sigma'_{l+1-i} \geq \sigma_{r+1-i} \text{ for } i = 1, \dots, l. \quad (3.62)$$

The condition number with respect to the  $L_2$  norm of the original matrix  $L$  is  $CN = \sigma_1 / \sigma_n$ . The condition number of a matrix  $L'$  is  $CN' = \sigma'_1 / \sigma'_{n-\tilde{n}} = \sigma'_1 / \sigma'_{n'}$ . Taking into account (3.60) one could write

$$\sigma'_1 / \sigma'_{n'} \leq \sigma_1 / \sigma_n. \quad (3.63)$$

Using  $i = 1$  in (3.62) we have  $\sigma'_l \geq \sigma_r$  and taking  $l = r - \tilde{n} = n - \tilde{n} = n'$  from (3.61) and  $r = n$  we derive the following inequality

$$\sigma'_{n'} \geq \sigma_n. \quad (3.64)$$

Now, (3.63) becomes  $\sigma'_1 / \sigma'_{n'} \leq \sigma_1 / \sigma'_{n'} \leq \sigma_1 / \sigma_n$ . This ends the proof that  $CN' \leq CN$ .

*Corollary 2:* In underdetermined linear inverse problems, decreasing number of sensors leads to a smaller condition number with respect to  $L_2$  norm. In the case of overdetermined problem, a general statement cannot be derived: it depends on the singular values of matrices  $L$  and  $L'$ .

### 3.7.4 Condition number with respect to the $L_2$ norm of three components measurements when all three components of magnetic dipoles are unknown is always larger than the condition number with respect to the $L_2$ norm of one component measurements and magnetic moments of known direction (one unknown per one dipole). This is valid for both under and overdetermined problems.

Let a lead field matrix  $L$  be of dimensions  $n \times m$ . Let a matrix  $L'$  be obtained from  $L$  by deleting  $\tilde{n}$  rows and  $\tilde{m}$  columns of  $L$ , while  $\tilde{n} = \tilde{m}$ . Now matrix  $L'$  has  $n' = n - \tilde{n}$  rows and  $m' = m - \tilde{m}$  columns. Define  $k$  as a rank of a matrix  $L'$ :  $k = n'$  if  $n < m$  and  $k = m'$  if  $n > m$ . Let  $\sigma'_1 \geq \sigma'_2 \dots \geq \sigma'_k \geq 0$  denote the singular values of a matrix  $L'$ . According to the rectangular Cauchy interlacing theorem (Theorem 23 in [75]), we have:

$$\sigma_j \geq \sigma'_j \text{ for } j = 1, \dots, k. \quad (3.65)$$

Furthermore, the number of positive singular values of  $L'$  is bounded from below by:

$$l = r - (\tilde{m} + \tilde{n}) = r - 2\tilde{n}, \quad (3.66)$$

where  $r$  is a rank of  $L$ ,  $r = n$  if  $n < m$  and  $r = m$  if  $n > m$ . Consequently,  $l \leq k$ , and if  $l \geq 1$ , the first  $l$  singular values of  $L'$  satisfy the lower bounds:

$$\sigma'_{l+1-i} \geq \sigma_{r+1-i} \text{ for } i = 1, \dots, l. \quad (3.67)$$

The condition number with respect to  $L_2$  norm of the original matrix  $L$  is  $CN = \sigma_1/\sigma_n$  for  $n < m$  and  $CN = \sigma_1/\sigma_m$  if  $n > m$ . The condition number of a matrix  $L'$  is  $CN' = \sigma'_1/\sigma'_{n-\tilde{n}} = \sigma'_1/\sigma'_{n'}$  when  $n < m$  and  $CN' = \sigma'_1/\sigma'_{m-\tilde{m}} = \sigma'_1/\sigma'_{m'}$  when  $n > m$ . Taking into account (3.65) for  $j = 1$  one can write

$$\sigma'_1/\sigma'_{n'} \leq \sigma_1/\sigma'_{n'}, \quad n < m \text{ and} \quad (3.68)$$

$$\sigma'_1/\sigma'_{m'} \leq \sigma_1/\sigma'_{m'}, \quad n > m. \quad (3.69)$$

Using  $i = 1$  in (3.67) we have  $\sigma'_l \geq \sigma_r$  and taking  $l = r - 2\tilde{n} = n'$  for  $n < m$  or  $l = r - 2\tilde{n} = m'$  for  $n > m$ , we derive the following inequalities

$$\sigma'_{n'} \geq \sigma_n, \quad n < m \text{ and} \quad (3.70)$$

$$\sigma'_{m'} \geq \sigma_m, \quad n > m. \quad (3.71)$$

Now, (3.68) becomes  $\sigma'_1/\sigma'_{n'} \leq \sigma_1/\sigma'_{n'} \leq \sigma_1/\sigma_n$  for  $n < m$  and (3.69) becomes  $\sigma'_1/\sigma'_{m'} \leq \sigma_1/\sigma'_{m'} \leq \sigma_1/\sigma_m$  for  $n > m$ . This ends the proof that  $CN' \leq CN$  for both under and overdetermined linear inverse problems.

*Corollary 3:* In both under and overdetermined linear inverse problems, the condition number with respect to the  $L_2$  norm of three components measurements, when all three components of magnetic dipoles moments are unknown, is always larger than the condition number with respect to the  $L_2$  norm of one component measurements and magnetic moments of known direction (one unknown per one dipole).

### 3.8 Theoretical proof that the condition number with respect to the $L_2$ norm of the kernel matrix remains the same after rotations of three-axial sensors at the same point for the same angle

It is already discussed from both numerical and theoretical aspects that variations of single-axis sensors orientations could improve the condition number with respect to the  $L_2$  norm of the corresponding kernel matrix. This triggers the question if the variations of orientations of three-axial sensors have the same effect on the condition of the linear inverse problem.

Let the lead field matrix of vectorial measurements be  $[L]_{3n \times 3m}$  defined by (3.27). After performing rotations of vectorial sensors for the angles  $\theta_x$ ,  $\theta_y$  and  $\theta_z$ , respectively around  $x$ ,  $y$  and  $z$  axis of the right Cartesian coordinate system, while the sensors at one point remain mutually perpendicular, and denoting rotations by the rotation matrix (3.29), then a lead field matrix can be written in the form  $[L']_{3n \times 3m} = [R]_{3n \times 3n} \cdot [D]_{3n \times 3n} \cdot [B]_{3n \times 3m}$ . Taking into account that the matrix  $D$  is an identity matrix, the lead field matrix after rotations is simplified to the form (3.30),  $[L']_{3n \times 3m} = [R]_{3n \times 3n} \cdot [L]_{3n \times 3m}$ .

### 3. Perturbations of singular values of a kernel matrix

---

Matrix  $R$  defined by (3.29) is a unitary matrix, so  $R \cdot R^T = I$  what gives  $(R \cdot R^T)^{-1} = I^{-1} = I$  i.e.

$$(R^T)^{-1} \cdot R^{-1} = I. \quad (3.72)$$

Matrix  $R$  is invertible, so  $(R^T)^{-1} = (R^{-1})^T$ . Putting this into (3.72), we get

$$(R^T)^{-1} \cdot R^{-1} = (R^{-1})^T \cdot R^{-1} = I. \quad (3.73)$$

From (3.73) follows that  $R^{-1}$  is also unitary matrix.

Applying the Theorem (3.1) from [76] and the statement that this identity also holds for multiplication by the unitary matrix on the right, we get

$$\|L^+ \cdot R^{-1}\|_2 = \|L^+\|_2. \quad (3.74)$$

Since matrix  $R$  is invertible, (3.74) could be written in the form

$$\|L^+ \cdot R^+\|_2 = \|L^+\|_2. \quad (3.75)$$

Let us now consider two matrices  $A \in M(m, n; K)$  and  $B \in M(n, p; K)$ . If

- $A$  has orthonormal columns ( $A^T A = I_n$ ) or
- $B$  has orthonormal rows ( $B B^T = I_n$ ) or
- $A$  is of full column rank and  $B$  is of full column rank, then

$$(A \cdot B)^+ = B^+ \cdot A^+. \quad (3.76)$$

In our case matrix  $R$  has orthonormal columns, i.e.  $R^T R = I$ , we can write  $(R \cdot L)^+ = L^+ \cdot R^+$ . Now, (3.75) becomes

$$\|(RL)^+\|_2 = \|L^+\|_2. \quad (3.77)$$

If we multiply the equality (3.77) by the  $L_2$  norm of a lead field matrix  $L$ ,  $\|L\|_2$ , we have

$$\|L\|_2 \cdot \|(RL)^+\|_2 = \|L\|_2 \cdot \|L^+\|_2. \quad (3.78)$$

According to the Theorem 3.1 from [76],  $\|R \cdot L\|_2 = \|L\|_2$ , (3.78) becomes

$$\|RL\|_2 \cdot \|(RL)^+\|_2 = \|L\|_2 \cdot \|L^+\|_2. \quad (3.79)$$

Since  $L' = RL$ , expression (3.79) can be written as

$$\|L'\|_2 \cdot \|(L')^+\|_2 = \|L\|_2 \cdot \|L^+\|_2, \quad (3.80)$$

or in a compact form

$$CN(L') = CN(L). \quad (3.81)$$

This completes the proof.

Hence, if three sensors measuring at one point three orthogonal directions change the directions so that they stay mutually orthogonal, then the condition number with respect to the  $L_2$  norm of the corresponding kernel matrix remains the same.

---

## 4 APPLICATION EXAMPLE I: OPTIMIZATION OF SENSOR ARRANGEMENTS IN MAGNETOCARDIOGRAPHY

### 4.1 Introduction

Biomagnetometers based on superconducting quantum interface device (SQUID) magnetic sensors are at this moment the most sensitive and the most widely used devices for magnetocardiography (MCG) [77, 78, 79]. SQUID is in fact used for measurements of magnetic flux density. There are two types of SQUIDs: RF SQUID that has one Josephson junction and the DC SQUID containing two Josephson junctions in parallel. There are two phenomena that occur when the material of SQUID becomes superconducting: flux quantization and the Josephson effect. Operation of SQUID sensors is based on these phenomena. Flux inside the SQUID ring cannot change continuously but only in multiples of flux quantum  $\phi_0$ ,  $\phi_0 = h/2e = 2.07 \times 10^{-15} \text{ Tm}^2$ . But, superconductivity shows up only at a very low temperature, and therefore the SQUID detector must be cooled for proper operation. Liquid helium is used as cooling fluid to reach a temperature of 4.2K. A critical part of every instrument is a cryostat enclosing a probe. It has to satisfy severe requirements: first, the material used for fabrication has to be nonmagnetic, second, the magnetic noise has to be less than the noise of the sensors and third, the distance of the detection coils from the subject must be as small as possible.

Besides the SQUID sensors, an optical spectroscopy of controlled atomic ensembles confined in vapor cells enables very precise measurement of magnetic fields [10, 80]. These sensors have a big advantage compared to SQUID sensors: they do not need to be cooled to cryogenic temperatures. Therefore, their operation costs less. Furthermore, when used in magnetocardiography application, these room temperature sensors allow for their placement around the body in a vest-like setup. Consequently, the question arises of how to place the magnetic field sensors optimally around the torso.

Optimal selection of leads in estimation of body surface potential maps in electrocardiography has been done already in the 1970's. Relying on data obtained from 132 human subjects including some with the normal electrocardiograms (ECG) as well as some with abnormal ECG's, Lux et al. [81] developed an algorithm for optimal selection of a limited number of leads. Estimation of body surface potentials from limited leads is based on three criteria: root mean square error, mean correlation coefficient between limited and total lead maps and error to signal power ratio. They concluded that 30-35 selected leads yield low enough error values. Furthermore, they found that the unique optimal sensor setup does not exist, i.e. different sensor sets can perform equally well.

Selection of the number and positions of measuring locations for electrocardiography is done in [82] as well. Applying principal component analysis followed by a minimum root mean square

estimation method, Bar et al. found that 24 out of 150 leads are sufficient for consistently acceptable accuracy. Studying of body surface potential maps is also done in [83], where the authors conclude with 32 leads being sufficient to provide an acceptable level of reconstruction performance.

Optimization of magnetic sensors arrangements has been done more recently. In order to determine an optimized MCG sensor arrangement, Nalbach and Dössel [51] use an initial configuration of 990 magnetometers on a grid of 15 elliptical layers with 66 magnetometers each and on the basis of information content they reduce the number of sensors. The information content is based on the slope of singular values. They found that the dense package of sensors right above the heart and the placement of some channels on the back of the patient would already lead to an increase of the information content.

Jazbinšek et al. studied the influence of limited lead selection on source localization in magnetocardiography and encephalography in [84]. Their results show that optimally selected limited lead system always performs better than random ones. Furthermore, the localization accuracy is not significantly improved if more than 20 optimal leads are selected.

An optimal arrangement of sensors for a 52-channel MCG system measuring tangential components of the cardiac magnetic fields is discussed in [85]. Using the confidence region method, they verified that their design of the sensor array is enough to obtain adequate information from the heart. They concluded that the tangential component MCG measurements are more suitable to an MCG system than the normal component measurements since they can localize deep current dipoles better than normal component MCG system. The main finding is that for tangential sensors 99% of the spatial spectral power at distance  $z$  from the source in  $z$ -direction is below  $1/2z$ . This means that the sampling width of  $z$  is sufficient. Since the heart lies at least 3 cm from the torso surface and the cryostat requires another 1 cm, they approximate  $z$  with 4 cm. Their resulting sensor setup is a regular grid with 4 cm width.

Assessing given sensor setups is proposed in a number of studies. The gain in reconstruction robustness by considering all three vectorial components of the field instead of just one is proposed in [86] and [87]. Di Rienzo et al. used the root mean square error, the mean correlation coefficient and lower error bounds as evaluation criteria. A theoretical lower error bound for comparative evaluation of sensor arrays in magnetostatic linear inverse problems is proposed in [86]. Rouve et al. propose a more theoretic optimization of sensor positions [22]. They use spherical harmonic representation to identify the magnetic multipolar sources associated to a given item, by measuring the near field around it. A genetic algorithm is used to find the optimum location for five sensors by minimizing the condition number with respect to the  $L_2$  norm of a kernel matrix. The sensor search space is a sphere around the source.

We aim to optimize a distribution of 21 and 32 magnetic sensors around the torso in a vest-like design by minimizing four figures of merit. A solution of optimization is not unique; therefore we sample the solution space of optimized sensor setups by optimizing repeatedly with random initialization and then clustering the sensor positions to elicit generalizable patterns. We determine the representative sensor of each cluster and obtain the orientation as the most frequent orientation among the orientations of sensors belonging to that cluster. Optimized sensor setups obtained by minimizing different goal functions are then compared and a behavior of minimization functions is assessed as well.

Some results of optimized sensors setups and analysis of behavior of different figures of merit are presented in [88-91].

### 4.2 Methods

#### 4.2.1 Experimental setup

A 72 years old male person serves as a test person. He had coronary artery disease with a 50% stenosis of the R. interventricularis anterior and a 70% stenosis of the R. circumflexus. An MCG of five minutes duration is made with the Argos200 System (Advanced Technologies Biomagnetics, Pescara, Italy). An MRI (T1) of the complete torso is made (resolution 1 mm). A patient positioning unit consisting of three coils arranged in a right-angle triangle on a non-magnetic base is placed on the test person. These landmarks can be identified in the MCG and MRI and both data sets can be mapped geometrically.

Segmentation of both lungs, blood volume inside the heart and the aortic arch is done using Curry Version 4.6 (NeuroScan Compumedics, El Paso, USA). The surfaces were triangulated with a triangle side length of 6 mm for the blood mass (1413 nodes), 10 mm for the both lungs (889+843 nodes) and 14 mm for the torso (2600 nodes). This resolution is found to be a good compromise between computational speed and reconstruction accuracy [92]. A homogeneous conductivity of 0.2 S/m is assumed for a torso including the heart muscle, 0.04 S/m for lungs and 0.6 S/m for the blood mass [92].

The source model of the cardiac field consists of 13 dipoles, Fig. 4.1. Dipole orientations are determined by performing a rotating dipole fit: a minimum norm with L-curve regularization and sLORETA [93, 94] noise normalization using Curry 4.6 over the averaged heart beat (PQRST) using all three components of the magnetic flux density. The resulting dipole orientations (Fig. 4.1) are mostly tangential, but they also have radial components. Dipole amplitudes at the first R-peak are shown in Fig. 4.2. Septal and posterior regions contain dipoles of the strongest amplitudes.

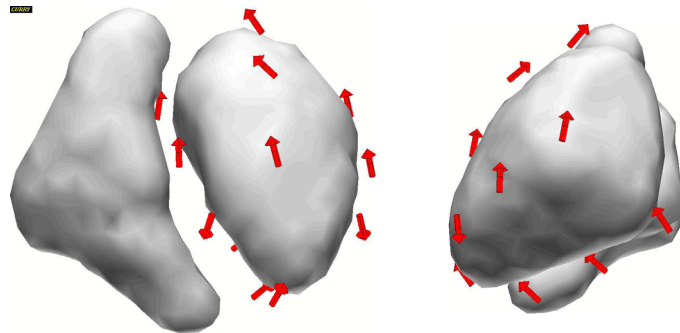


Fig. 4.1 – Dipole model consisting of 13 dipoles around the left ventricle. Orientations are fitted with minimum norm, L-curve regularization and sLORETA noise normalization. The figure is taken from [95].

In our optimizations we assume a sensor with a spherical outer bound of diameter 1 cm. This is about the size of optical magnetometers [96] and approximately the size of current integrate SQUIDS (8×8 mm in the Argos200 system). The sensor is assumed to pick up the field component in normal direction to the coil area.

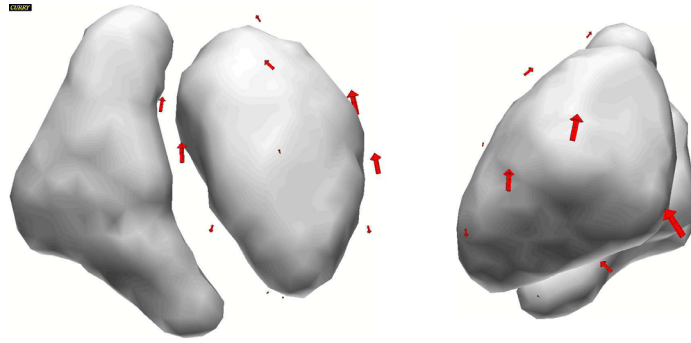


Fig. 4.2 – Current density distribution at the R-peak using the 13 dipoles model presented in Fig. 4.1 The figure is taken from [95].

The search volume is derived from the torso surface and it looks like a vest [95], Fig. 4.3. There are 19759 possible positions which are in fact the nodes of triangulation (side length 4 mm) of the dilated torso surface (triangle side length of the torso triangulation is 14 mm). Directions are discretized with  $30^\circ$ , allowing 62 orientations per position. One has to be aware that these are 31 different orientations since the two of opposite direction ( $180^\circ$  angle between them) are in fact the same.

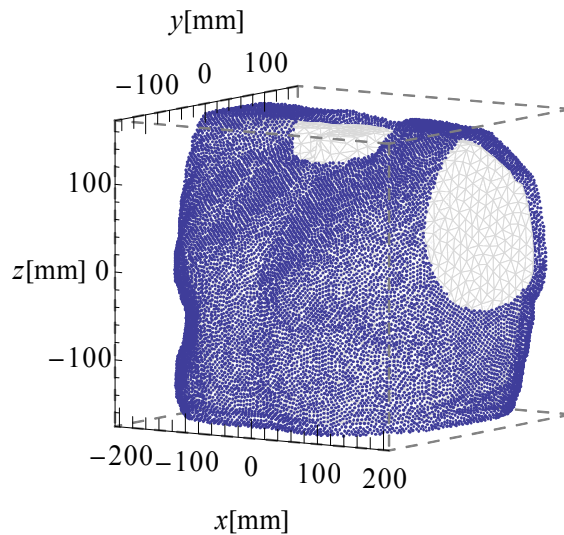


Fig. 4.3 – Search sensor space containing 19759 positions on the vest. Connections to arms, neck and lower body are omitted.

An optimization of positions and orientations of 21 and 32 sensors using a quasi-continuous constrained particle swarm optimization approach [97, 98] is done. Five parameters are optimized for each sensor: three Cartesian coordinates for the position and two spherical angles for the orientation. This technique optimizes a problem by having a population of candidate solutions (particles) and moving these particles in the search space according to the simple formula over the particle's position and velocity. Movement of each particle is influenced by its local best known position. This technique is much more robust against local minima or disturbances in a goal function. The algorithm is implemented as an extension of the software toolbox SimBio [99].



Because the calculation of the lead field matrix in every iteration is computationally too expensive, the sensor space is finely discretized and the kernel matrix for all possible sensor positions and orientations is pre-computed.

Two constraints are imposed in this optimization process: first, sensor positions are restricted to the outside of the body, i.e. to the vest surface and second, the sensors have a certain physical size, which implies a minimum distant constraint to the sensor positions. The magnetic sensors are modeled as coils with a single turn and a diameter of 1cm. This implies a minimum distance of 1cm between them.

### 4.2.2 Goal functions

In our optimization procedure, we minimize four goal functions: condition number with respect to the  $L_2$  norm  $CN$ , Skeel condition number  $Skeel$ , inverse average decay of singular values of a kernel matrix  $\rho$  and a figure of merit based on the angles between columns of a lead field matrix and rows of its pseudoinverse  $\xi$ , described respectively in sections 2.1.2, 2.1.3, 2.1.4 and 2.2.2 of this thesis. The goal functions are implemented as an extension of the software [95]. Because the solution of this problem is not unique, we repeat the optimization for all four goal functions 256 times using random initial sensor configurations. This allows sampling of solution space and eliciting generalizable patterns.

### 4.2.3 Clustering procedure

The optimization procedure run 256 times gives as a result a set of 5376 and 8192 sensors for the 21 and 32 sensors setup respectively. A determination of the intrinsic grouping of these sensors into 21 and 32 groups is done applying a clustering procedure.

Cluster analysis divides data into groups (clusters) that are meaningful and useful. It plays an important role in a wide variety of fields: psychology and other social sciences, biology, statistics, pattern recognition, information retrieval, machine learning and data mining. The most commonly discussed distinction among different types of clustering is whether the set of clusters is nested or nonnested, or hierarchical or partitional. A partitional clustering is a division of a set of data objects into non-overlapping subsets (clusters) such that each data object is in exactly one subset. If it is permitted that clusters have subclusters, then the clustering is hierarchical, which is, in fact, a set of nested clusters that are organized as a tree. Each cluster in the tree is the union of its subclusters and the root of the tree is the cluster containing all the objects. In our clustering procedure, separation of sensors into non-overlapping clusters provides clear optimized sensor setups.

In the case of non-constrained optimization, sensors belonging to the edge of the vest would be outside of the vest surface and inside the body. Therefore, before performing the clustering, sensors positioned at the edge of the vest i.e. at the lower part of the torso, around neck and around left and right shoulder are rejected, Fig. 4.4. Rejected positions of the lower part of the torso satisfy the condition  $z < -150\text{mm}$ , around the left arm they belong to the volume of the sphere of the center (258mm, 20mm, 55mm) and radius 140mm, around the right arm they belong to the volume of the sphere of the center (-258mm, 20mm, 55mm) and radius 140mm, and around the neck to the volume of the sphere of the center (-1.56mm, 10.94mm, 165.6mm) and radius 95mm.

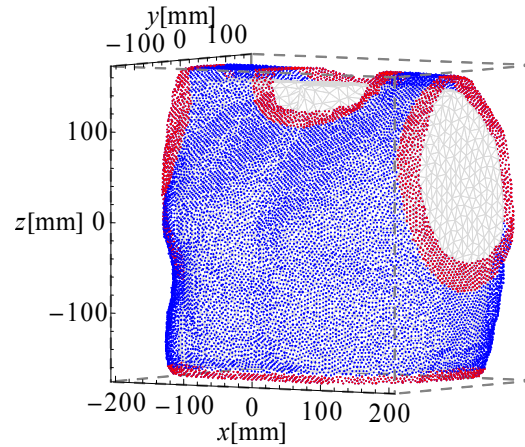


Fig. 4.4 – Rejected sensors positions: at the lower part of the torso, around neck and around left and right shoulder. These positions are marked in red.

The remaining sensors are then partitioned into 21 or 32 clusters depending on the number of sensors in a sensor setup that is being optimized. In the clustering process, variables for clustering have to be selected. For this application, the three position variables obtained for each sensor using particle swarm optimization, have been chosen as variables which the partitioning clustering will rely on. Partitioning is done using the Partitioning Around Medoids (PAM) algorithm implemented in Mathematica 8.0. The medoid of the cluster is the sensor with the smallest average distance to all other sensors in that cluster.

The PAM algorithm is developed by Kaufman and Rousseeuw [100]. This algorithm is very similar to K-means algorithm, because both are partitional algorithms, i.e. both break the datasets into groups and both work trying to minimize the error. The difference is that PAM works with medoids, that are an entity of data set that represent the group. K-means works with centroids that are artificially created representing the center of the cluster. Our input in the algorithm are 5376 or 8192 sensor positions obtained in particle swarm optimization, and the number of clusters is 21 or 32. The algorithm works with a matrix of dissimilarity, where its goal is to minimize the overall dissimilarity between the representants of each cluster and its members. The algorithm consists of two phases: the build phase and the swap phase. In the build phase, the algorithm chooses a certain number of entities to become the medoids, calculates the dissimilarity matrix and assigns every entity to its closest medoid. In a swap phase, algorithm searches in each cluster if there exists the entity of the cluster that lower the average dissimilarity coefficient. If such entities exist, then the entity that lower this coefficient the most is taken as a medoid for the cluster. If the medoid from at least one cluster has changed, then every entity is again assigned to its closest medoid. In the case of no changing of medoids, the procedure ends. In Mathematica 8.0, the »Optimize« method is based on partitioning around medoids. It starts by building a set of desired representative objects, and clustering around those, iterating until a (locally) optimal cluster is found. In our simulations, the PAM converged in less than 10 iterations in all cases. FindClusters in Mathematica treats pairs of elements as being less similar when their distances are larger and by default uses a squared Euclidian distance.

#### 4.2.4 Determination of the cluster representative sensor position

When calculating the position of cluster center as a mean value of positions of all sensors belonging to that cluster, it could likely happen that the center of the cluster does not belong to the searching space that is in this case the vest or it could even happen that the center appears inside the body. This is especially the case for clusters whose space has a high curvature, i.e.

these are the clusters under the arms extending to the front or back of the torso and around the shoulders.

Therefore, instead of using the mean point as the center of the cluster, the clustering procedure used in the partitioning takes an actual sensor in the cluster to represent its center. So, the position of the medoid, as the most centrally located object of the cluster, is taken as a position of the representative sensor of that cluster.

#### 4.2.5 Determination of the cluster representative sensor orientation

As a result of the optimization procedure, we get not only the sensor positions but also their orientations. Each cluster contains a set of sensors, i.e. a set of orientations. Here arises a question of determination of the representative orientation from a set of directions.

In the case of plane vectors, the main direction of a set of directions can be calculated by summing up the cosines and sines of all the angles and applying then the inverse tangent. But, as a result of our optimization procedures there are two difficulties: first, the obtained sensor directions are in a space and second, two directions that form an angle of  $180^\circ$  have to be treated as the same direction (SQUID sensors oriented in those two directions measure the same magnitude of magnetic flux density). A solution of this particular problem is found in exploring of a procedure of finding of the most frequent orientation within each cluster.

Sensor orientation is presented by a unit vector, completely defined by the inclination and azimuth. All the orientation vectors belonging to one cluster are put in a unit sphere (Fig. 4.5a). The head of each vector belongs to the surface of a unit sphere. The number of appearances of each orientation within a cluster is then counted and a corresponding head of each orientation vector is colored using the color scheme presented in Fig. 4.5b (no appearance of the orientation corresponds to zero and is colored blue, while the most frequent orientation within a cluster corresponds to one and is colored red). For each orientation vector, its opposite vector is counted, too. This allows for equal treatment of opposite SQUIDs orientations.

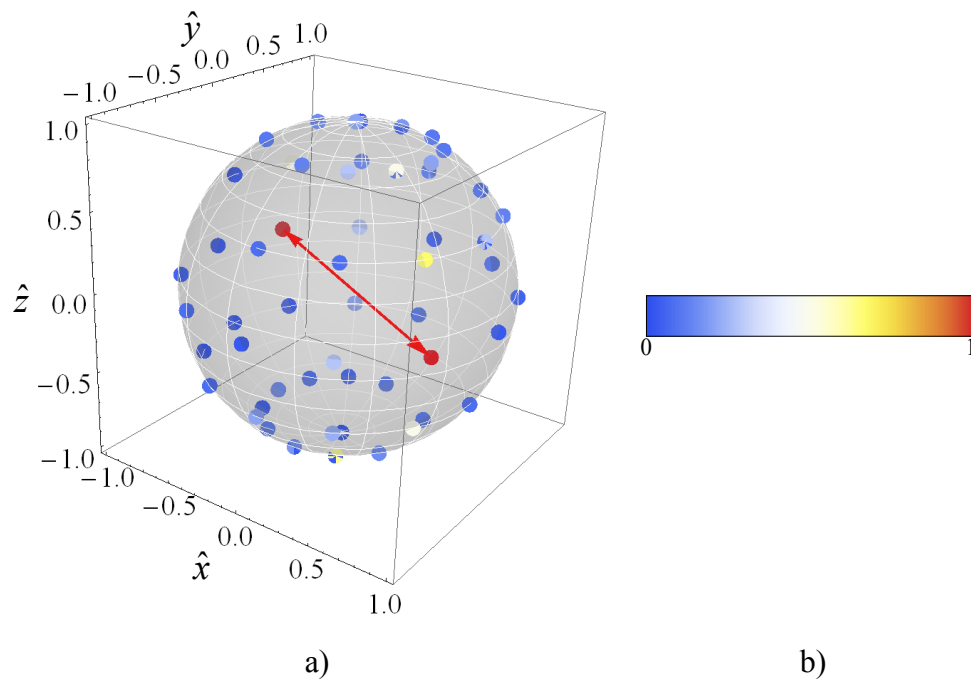


Fig. 4.5 – Representative orientation vector of the cluster (marked by red arrow) is chosen as the most frequent orientation within a cluster (a). Orientations are colored using a scale (b).

### 4.3 Results

#### 4.3.1 Sensor clusters

##### *21 sensors setup*

The results of clustering procedure described in section 4.2.3 for the 21 sensors setup are presented in Figs. 4.6 – 4.9. These results are obtained after minimization of  $CN$ ,  $Skeel$ ,  $\rho$  and  $\xi$  respectively.

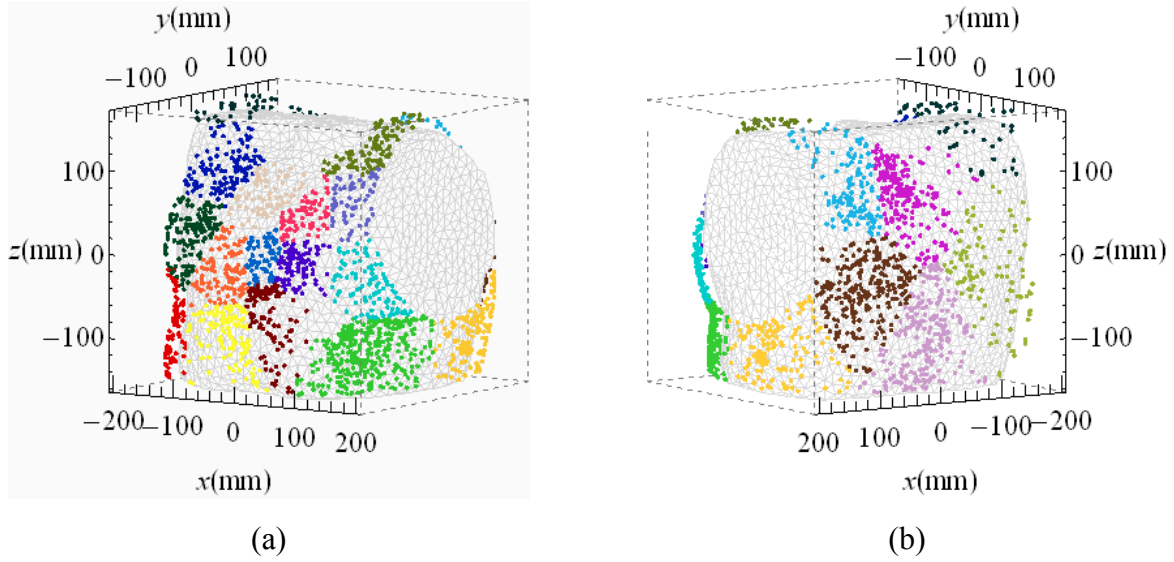


Fig. 4.6 – Color-coded sensor clusters for the 21 sensors array displayed on the triangulated torso for the  $CN$  from the front (a) and from the back (b).

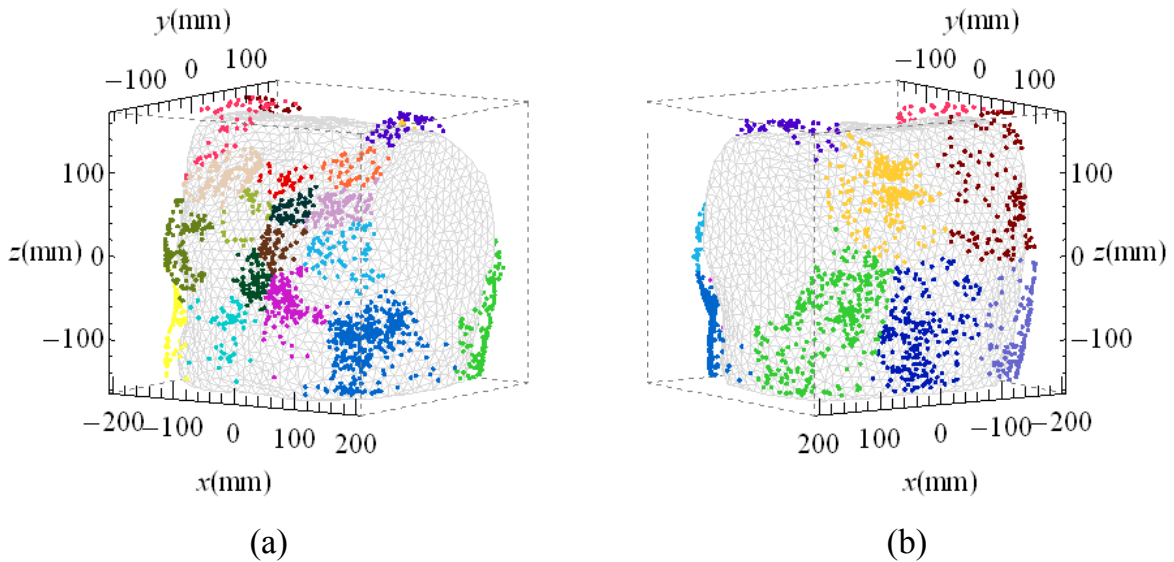


Fig. 4.7 – Color-coded sensor clusters for the 21 sensors array displayed on the triangulated torso for the  $Skeel$  from the front (a) and from the back (b).

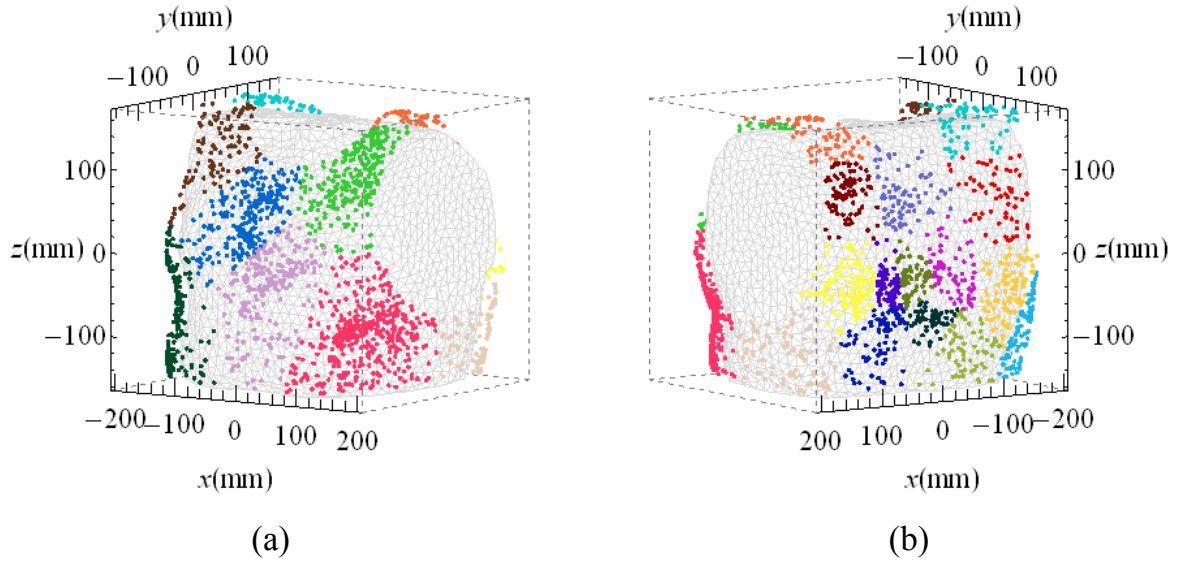


Fig. 4.8 – Color-coded sensor clusters for the 21 sensors array displayed on the triangulated torso for the  $\rho$  from the front (a) and from the back (b).

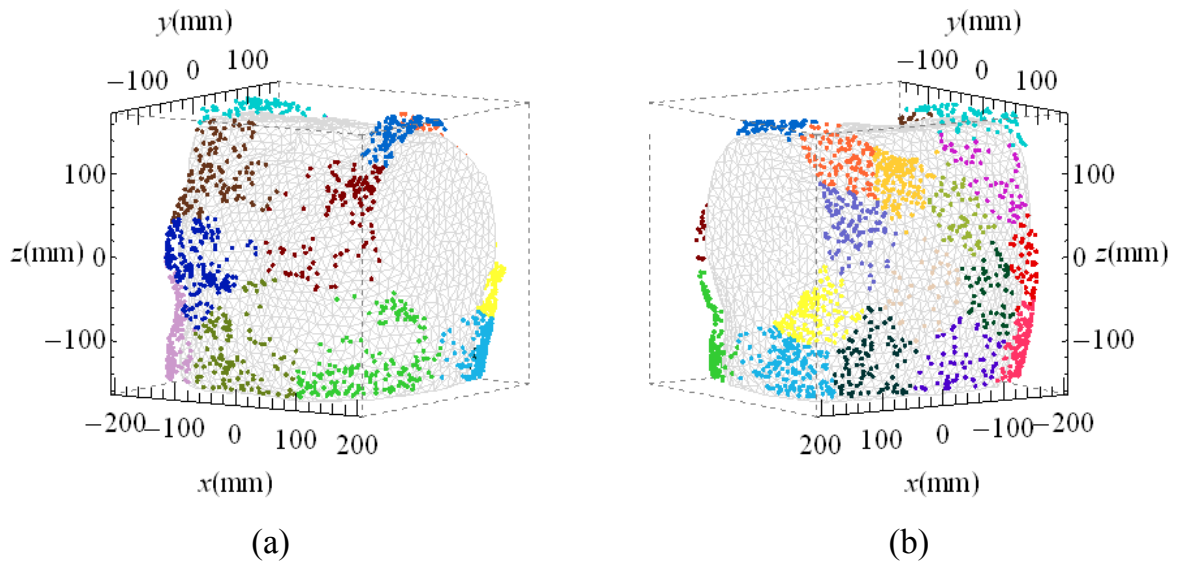


Fig. 4.9 – Color-coded sensor clusters for the 21 sensors array displayed on the triangulated torso for the  $\xi$  from the front (a) and from the back (b).



### 32 sensors setup

The results of the clustering procedure presented in the section 4.2.3 for the 32 sensors setup are presented in Figs. 4.10 – 4.13 obtained after minimization of  $CN$ ,  $Skeel$ ,  $\rho$  and  $\xi$  respectively.

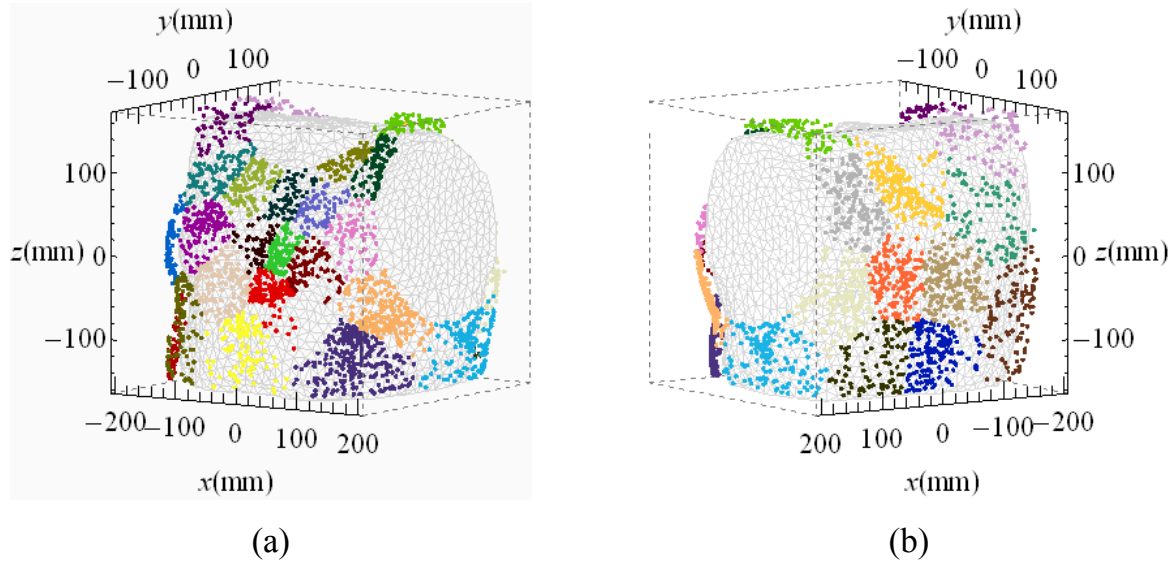


Fig. 4.10 – Color-coded sensor clusters for the 32 sensors array displayed on the triangulated torso for the  $CN$  from the front (a) and from the back (b).

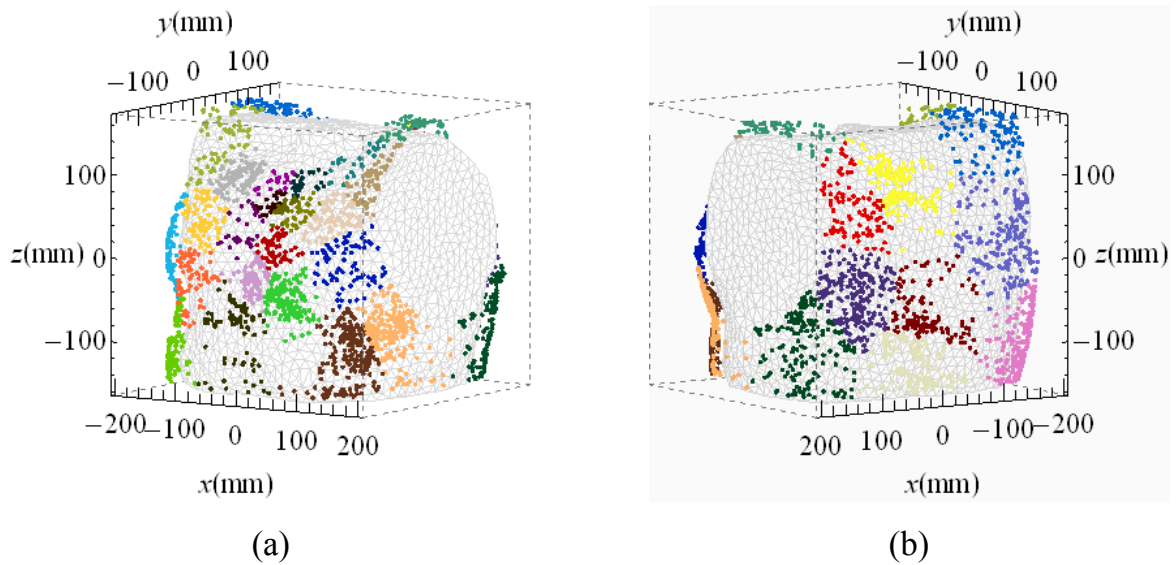


Fig. 4.11 – Color-coded sensor clusters for the 32 sensors array displayed on the triangulated torso for the  $Skeel$  from the front (a) and from the back (b).

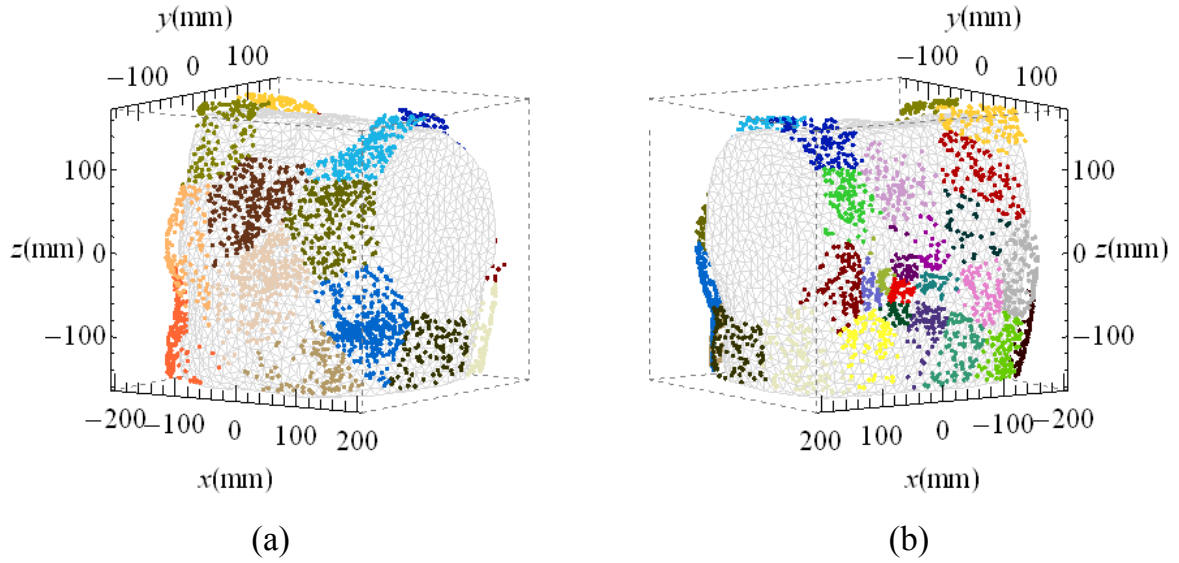


Fig. 4.12 – Color-coded sensor clusters for the 32 sensors array displayed on the triangulated torso for the  $\rho$  from the front (a) and from the back (b).

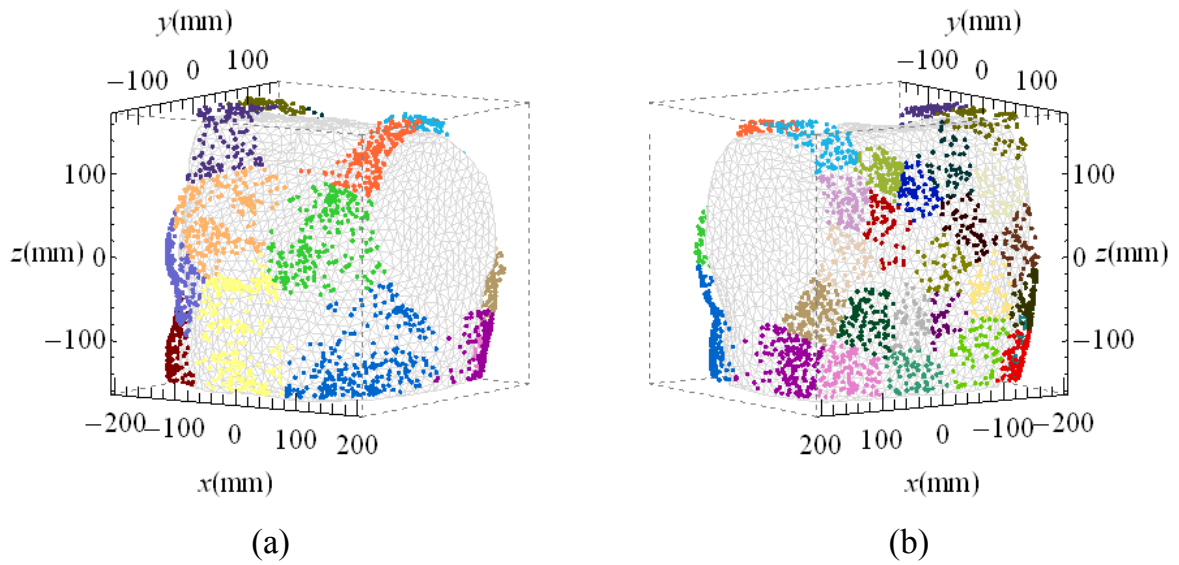


Fig. 4.13 – Color-coded sensor clusters for the 32 sensors array displayed on the triangulated torso for the  $\xi$  from the front (a) and from the back (b).

### 4.3.2 Cluster medoids

Optimized sensor set-ups consisting of 21 sensors obtained after minimization of  $CN$ ,  $Skeel$ ,  $\rho$  and  $\xi$  are presented in Figs. 4.14-4.17 respectively. Optimized sensor set-ups consisting of 32 sensors obtained after minimization of  $CN$ ,  $Skeel$ ,  $\rho$  and  $\xi$  are presented in Figs. 4.18-4.21, respectively.

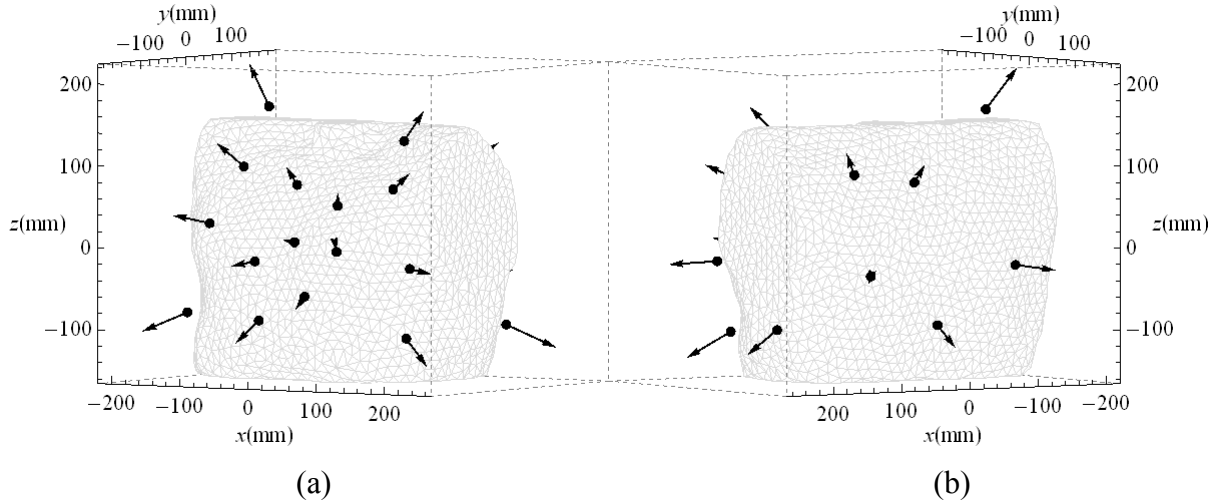


Fig. 4.14 – Optimized 21 sensors set-up obtained minimizing the  $CN$  from the front (a) and from the back (b).

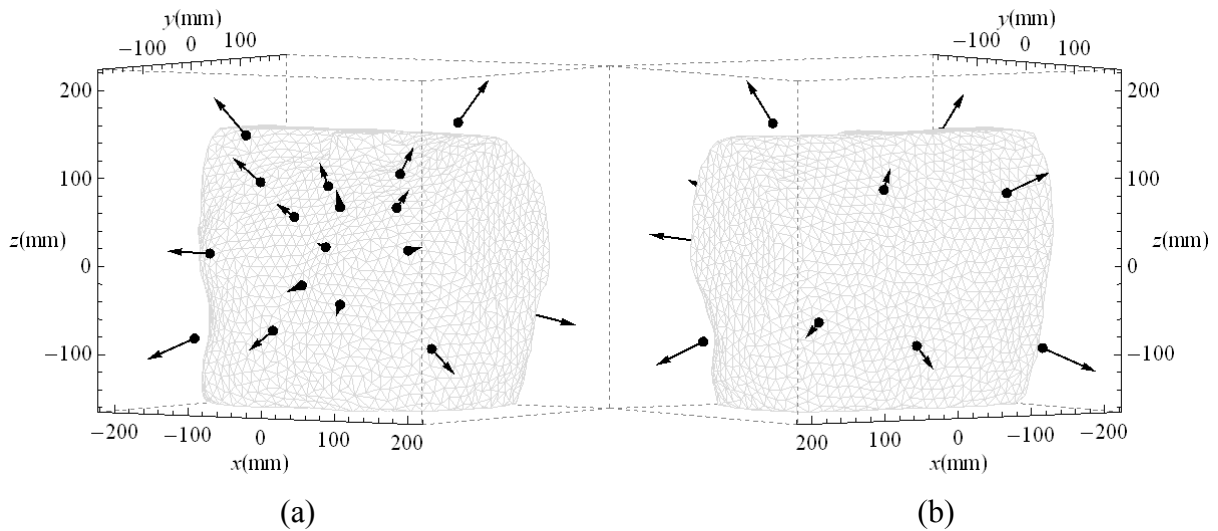


Fig. 4.15 – Optimized 21 sensors set-up obtained minimizing the  $Skeel$  from the front (a) and from the back (b).



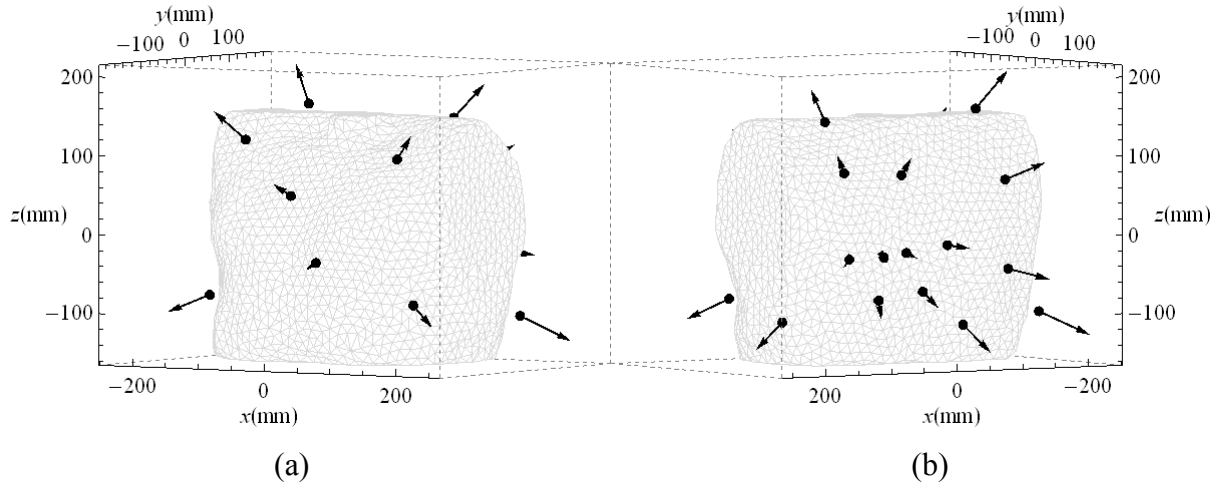


Fig. 4.16 – Optimized 21 sensors set-up obtained minimizing the  $\rho$  from the front (a) and from the back (b).

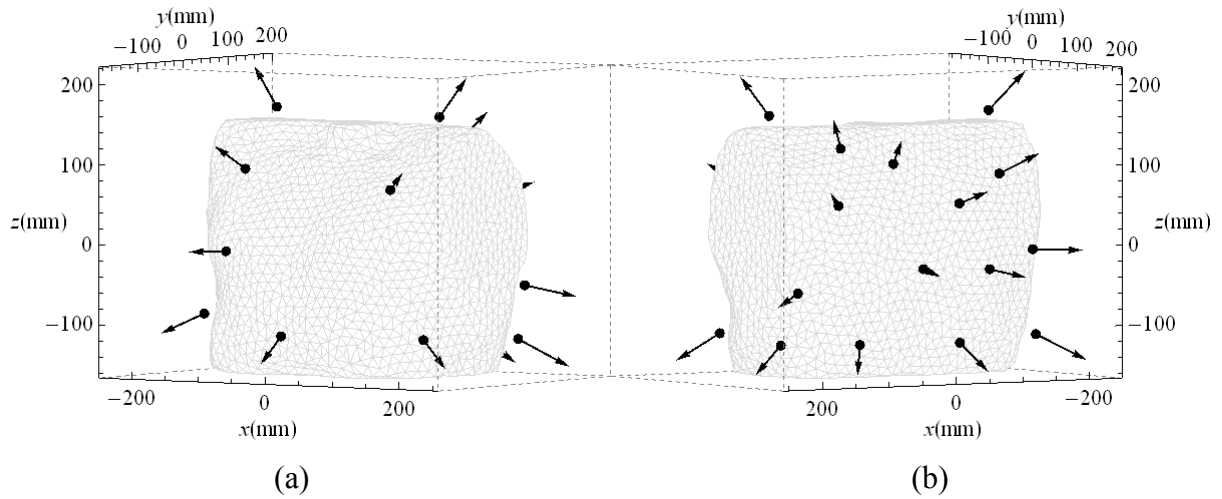


Fig. 4.17 – Optimized 21 sensors set-up obtained minimizing the  $\xi$  from the front (a) and from the back (b).

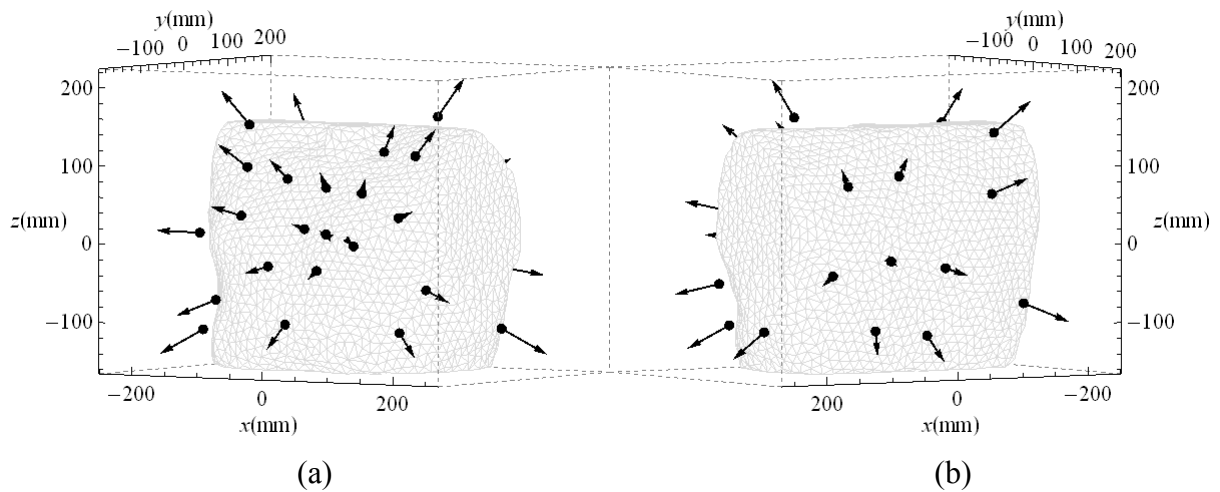


Fig. 4.18 – Optimized 32 sensors set-up obtained minimizing the  $CN$  from the front (a) and from the back (b).

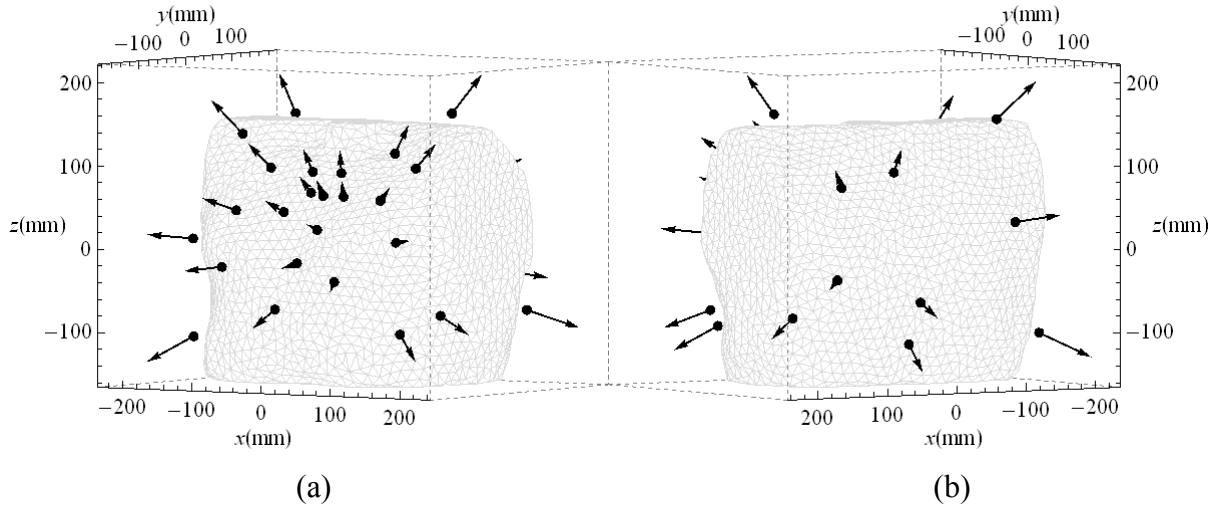


Fig. 4.19 – Optimized 32 sensors set-up obtained minimizing the *Skel* from the front (a) and from the back (b).

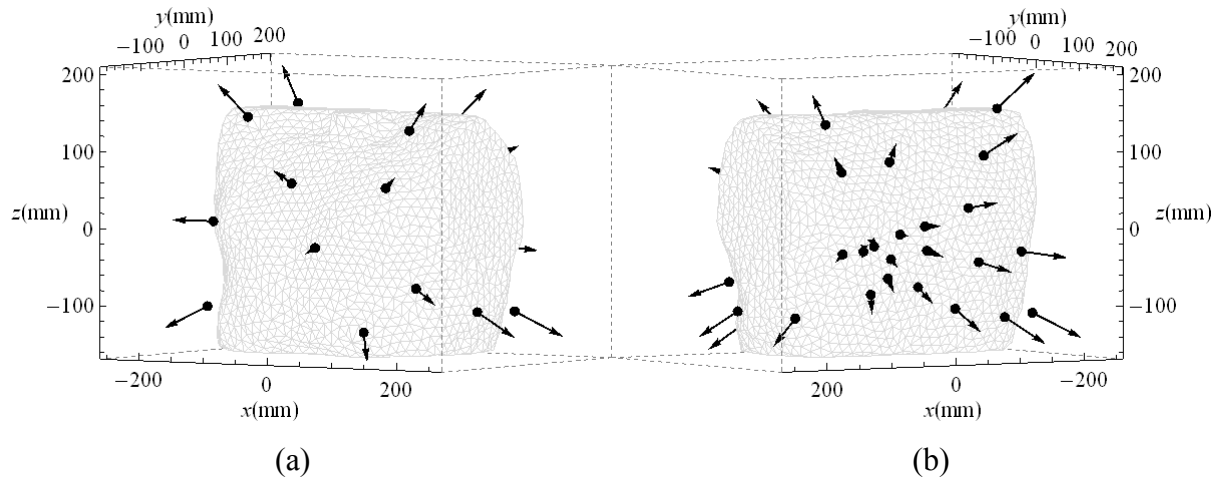


Fig. 4.20 – Optimized 32 sensors set-up obtained minimizing the  $\rho$  from the front (a) and from the back (b).

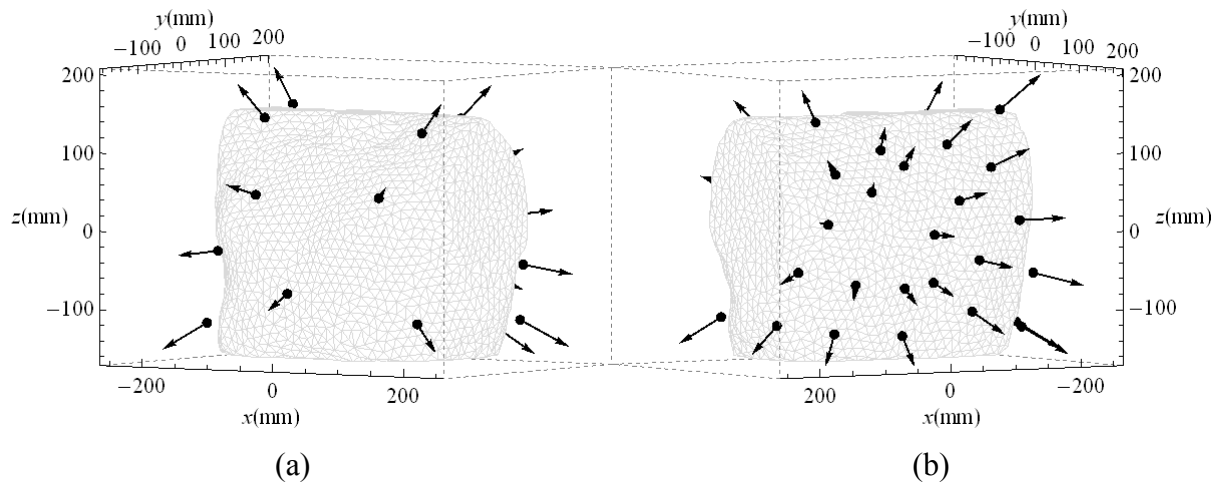


Fig. 4.21 – Optimized 32 sensors set-up obtained minimizing the  $\xi$  from the front (a) and from the back (b).

### 4.3.3 Clusters and FOMs characteristics

*Number of sensors after exclusion of edge sensors and percentage of the vest area covered by sensors*

#### *21 sensors setup*

If the applied optimization procedure were not constrained, the sensors at the edge of the vest would be outside the vest surface and inside the body. Therefore sensors at the lower part of the torso, around neck and around left and right shoulder are rejected (section 4.2.3). In 21 sensors setup, from the pooled set of 5376 optimized sensor positions, we have excluded from the further analysis 43.3%, 40.5%, 36.4% and 53.4% of sensors obtained by minimizing  $CN$ ,  $Skeel$ ,  $\rho$  and  $\xi$ , respectively. The remaining sensors had 2406, 2158, 2352 and 2140 different positions, covering 15.5%, 13.9%, 15.2% and 13.8% of vest area, respectively for  $CN$ ,  $Skeel$ ,  $\rho$  and  $\xi$ . Minimization of the figure of merit  $\rho$  provides the largest number of sensors belonging to the vest surface of interest (not belonging to any of the vest edges). The largest number of different locations is achieved minimizing the  $CN$ . Minimization of the figure of merit  $\xi$  covers the smallest surface of the vest area, while  $CN$  the largest. The corresponding data is presented in the Table 4.1.

Table 4.1. Number of excluded sensors as belonging to the edge of the vest, number of different locations and percentage of the vest area covered by sensors for 21 sensor setup and different figures of merit.

	Number of sensors when edges are excluded	Number of different locations	Percentage of the vest area [%]
$CN$	3048	2406	15.5
$Skeel$	3196	2158	13.9
$\rho$	3421	2352	15.2
$\xi$	2504	2140	13.8

#### *32 sensors setup*

From the pooled set of 8192 optimized sensor positions, we have excluded from the further analysis 47.2%, 46.9%, 40.3% and 53.3% of sensors obtained by minimizing  $CN$ ,  $Skeel$ ,  $\rho$  and  $\xi$ , respectively. Regarding the percentage of the excluded sensors, figures of merit are in the same order as in the sensor array containing 21 sensors. The remaining sensors had 3220, 2814, 3222 and 3106 different positions, covering 20.8%, 18.1%, 20.8% and 20.0% of vest area, respectively for  $CN$ ,  $Skeel$ ,  $\rho$  and  $\xi$ . Minimization of the figure of merit  $\rho$  provides the largest number of sensors belonging to the vest surface of interest (not belonging to any of the vest edges). Figure of merit  $\rho$  provides the largest number of different locations, only two more than  $CN$  does. This could likely be changed performing the larger number of runs. Minimization of the figure of merit  $Skeel$  covers the smallest surface of the vest area, while  $CN$  and  $\rho$  cover the equal largest part of the vest. The corresponding data is presented in the Table 4.2.

#### 4. Application example I: Optimization of sensor arrangements in magnetocardiography

Table 4.2. Number of excluded sensors as belonging to the edge of the vest, number of different locations and percentage of the vest area covered by sensors for 32 sensor setup and different figures of merit.

	Number of sensors when edges are excluded	Number of different locations	Percentage of the vest area [%]
<i>CN</i>	4325	3220	20.8
<i>Skeel</i>	4345	2814	18.1
$\rho$	4893	3222	20.8
$\xi$	3827	3106	20.0

##### *Median distances between sensor cluster medoids and single sensors*

##### *21 sensors setup*

Cluster members in the 21 sensor array have the median distance to their medoids 36.7 mm, 34.2 mm, 33.2 mm and 40.1 mm, respectively for the *CN*, *Skeel*,  $\rho$  and  $\xi$ . Number of sensors versus distance to their cluster medoid for the 21 sensor array is presented in Fig. 4.22.

Table 4.3 presents median and maximal distance between sensor cluster medoids and single sensors.

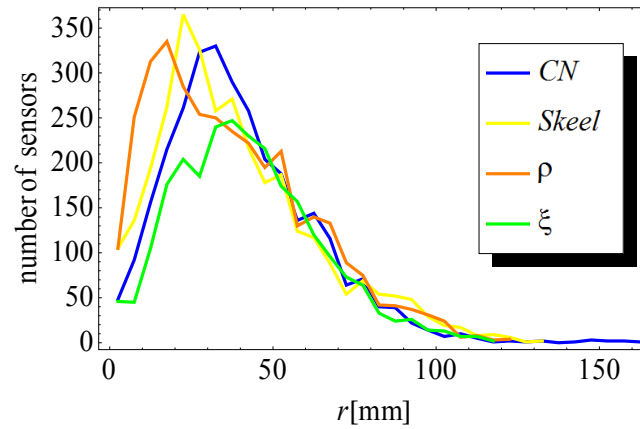


Fig. 4.22 – Number of sensors versus distance to their cluster medoid for 21 sensor array for *CN*, *Skeel*,  $\rho$  and  $\xi$ .

Table 4.3. Median and maximal distance between sensor cluster medoids and single sensors for 21 sensor setup and different figures of merit.

	Median distance between sensor cluster medoids and single sensors [mm]	Maximal distance between sensor cluster medoids and single sensors [mm]
<i>CN</i>	36.7	161.7
<i>Skeel</i>	34.2	131.4
$\rho$	33.2	123.4
$\xi$	40.1	119.3

Clusters obtained using the figure of merit  $\rho$  have the highest cluster density compared to those obtained with other figures of merit (Fig. 4.22). This figure shows that the maximal sensor distance is the largest in the case of minimization of the  $CN$  (161.7 mm as indicated in the Table 4.3). The most common distance to the respective medoid is approximately 32 mm, 23 mm, 17 mm and 37 mm for  $CN$ ,  $Skeel$ ,  $\rho$  and  $\xi$  respectively (Fig. 4.22). This indicates an average equivalent cluster diameter of 64 mm, 46 mm, 34 mm and 74 mm.

The median distance between sensor cluster medoids and single sensors is the smallest after minimization of the  $\rho$ .

### 32 sensors setup

Cluster members in the 32 sensor array have the median distances to their medoids 30.8 mm, 27.9 mm, 29.6 mm and 34.2 mm, respectively for the  $CN$ ,  $Skeel$ ,  $\rho$  and  $\xi$ . Number of sensors versus distance to their cluster medoid for 32 sensor array is presented in Fig. 4.23. Table 4.4 presents median and maximal distances between sensor cluster medoids and single sensors for 32 sensor array and different figures of merit.

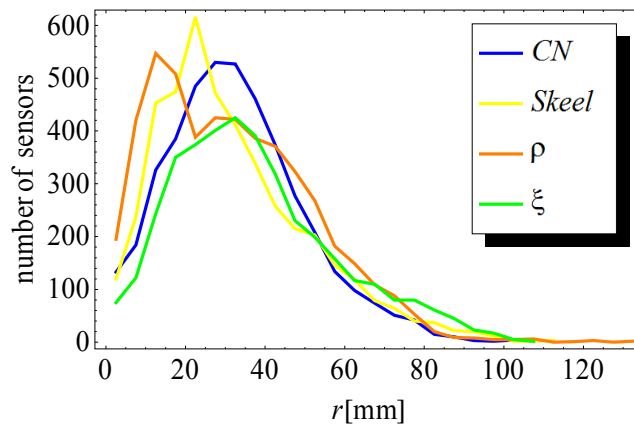


Fig. 4.23 – Number of sensors versus distance to their cluster medoid for 32 sensor array for  $CN$ ,  $Skeel$ ,  $\rho$  and  $\xi$ .

Table 4.4. Median and maximal distance between sensor cluster medoids and single sensors for 32 sensor setup and different figures of merit.

	Median distance between sensor cluster medoids and single sensors [mm]	Maximal distance between sensor cluster medoids and single sensors [mm]
$CN$	30.8	108.1
$Skeel$	27.9	110.8
$\rho$	29.6	131.3
$\xi$	34.2	108.3

Clusters obtained using the figure of merit  $\rho$  have the highest cluster density compared to those obtained with other figures of merit (Fig. 4.23). This figure shows that the maximal sensor

distance is the largest in the case of minimization of the  $\rho$  (131.3mm as indicated in the Table 4.4). The most common distance to the respective medoid is approximately 27mm, 22mm, 12mm and 32mm for  $CN$ ,  $Skeel$ ,  $\rho$  and  $\xi$  respectively (Fig. 4.23). This indicates an average equivalent cluster diameter of 54mm, 44mm, 24mm and 64mm.

The median distance between sensor cluster medoids and single sensors is the smallest after minimization of the  $Skeel$ . The smaller median of sensors distances to the respective medoids in the case of 32 sensors indicates a higher cluster density comparing to the 21 sensors setup and therefore no overpopulation with 32 sensors.

The maximal sensor distance to the medoid is smaller in case of 32 sensors compared to the case of 21 sensors, except for the  $\rho$ .

##### *Values, mean values and standard deviations of FOMs*

Since the figures of merit used as minimization functions in the particle swarm optimization process rely on different features of the lead field matrix, they have different absolute values: the numbers range from single digit to the tens of thousands. In order to show the order of the number that different figures of merit have and to show the distribution of those numbers during 256 optimization runs, the histograms of values of figures of merits are presented in Fig. 4.24.

Mean values and standard deviations of values of all FOMs obtained after particle swarm optimization process, for both 21 and 32 sensors setups, are presented in Table 4.5.

Table 4.5. Mean values and standard deviations of values of  $CN$ ,  $Skeel$ ,  $\rho$  and  $\xi$  for 21 and 32 sensors setups.

	Mean value		Standard deviation	
	21 sensors	32 sensors	21 sensors	32 sensors
$CN$	21.46	19.05	1.53	1.15
$Skeel$	26.52	26.21	1.29	1.21
$\rho$	2.53	2.51	0.056	0.054
$\xi$	24072.0	27079.6	3458.84	3291.55

On one hand, as shown in Fig. 4.24, histograms of values of  $CN$ ,  $Skeel$ ,  $\rho$  and  $\xi$  for 32 sensors seem to be more Gaussian than for 21sensors. On the other hand, the standard deviation is smaller for 32 sensors for all figures of merit (Table 4.5). This means that the different particle swarm optimization runs converge better to a set of solutions for higher number of sensors leading to a better posed optimization problem in the case of 32 sensors comparing to the setup of 21 sensors.

The mean values of  $CN$ ,  $Skeel$  and  $\rho$  are lower for 32 than 21 sensors setup.

The highest standard deviation of the figure of merit  $\xi$  in both 21 and 32 sensors setups indicates that its values are spread out over the largest range of values.

The smaller standard deviation and the more Gaussian distribution might be taken together as an indicator for the not yet existing loss of generalisability in case of 32 sensors. This would mean that there is no overpopulation with 32 sensors in these noise free simulations.

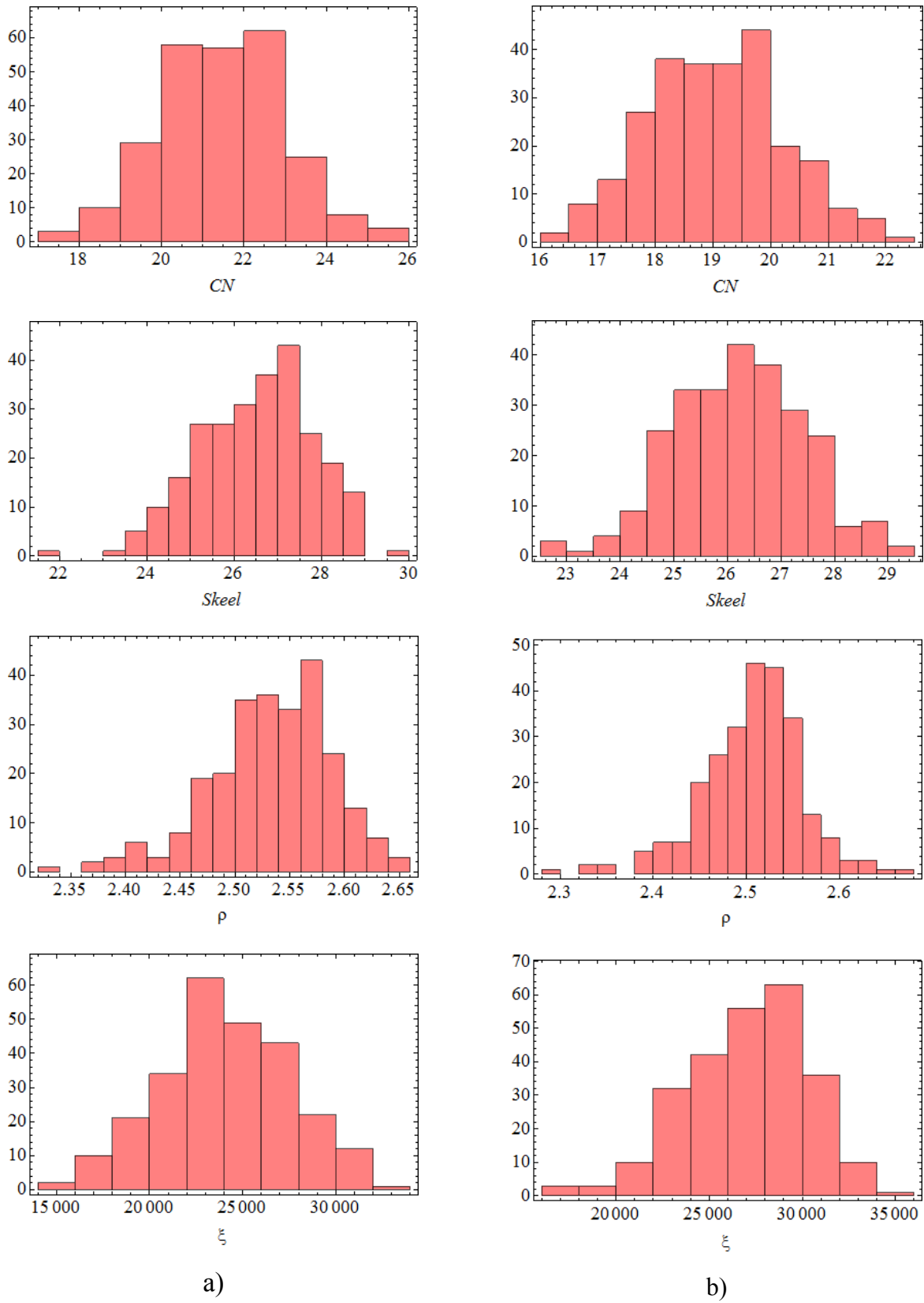


Fig. 4.24 – Values of  $CN$ ,  $Skeel$ ,  $\rho$  and  $\xi$  obtained after minimization applying particle swarm optimization for 21 sensors setup (a) and 32 sensors setup (b).

### 4.4 Discussion

Optimized sensor setups obtained after minimization of all four figures of merit show non-uniform distribution of sensors on the whole torso surface. Placement of sensors on the back of the torso but not only on the front improves the condition of the linear inverse problem, that is in this case calculation of the sources in the heart from the extracorporeal magnetic field measurements. The same finding has been obtained in [51, 84, 101]. Nalbach and Dössel in [51] optimize magnetic sensor composition maximizing its information content, i.e. minimizing the steepness of the slope of singular values of the corresponding kernel matrix. Explanations on the correlation between the steepness of the slope of singular values and the figure of merit  $\rho$  used for the optimization of sensor array in this thesis can be found in the section 2.1.4.

Different to  $\rho$  and  $\xi$ , minimization of  $CN$  and  $Skeel$  produce more sensors on the front than on the back of the torso in both the 21 and 32 sensors setups. This in on one hand in line with the findings in [51] and [101]. On the other hand  $CN$  and  $Skeel$  are better correlated to the excitation pattern exemplified by the reflection of the Wilson lead sequence.

Minimization of  $CN$  and  $Skeel$  leads to a denser package of front sensors in the area above the heart comparing to the minimization of  $\rho$  and  $\xi$ . These more densely distributed sensors above the heart likely lead to an increase in information content in [51].

While in [84] the magnetic sensors on the back of the torso are mostly positioned on its left part, optimized sensor arrays in this thesis contain magnetic sensors also on the back right side (except in the case of minimization of the  $CN$  and 21 sensor array where only one sensor is on the right side of the back of the torso). Minimization of  $CN$ ,  $Skeel$  and  $\xi$  provides more evenly distributed sensors on the back of the torso, while  $\rho$  has a higher concentration of sensors over the heart on the back side of the torso.

Based on the sampling theory, the distance of tangential magnetometers on a regular grid was estimated by Kim et al. [85]. They propose a grid spacing of 4 cm, which coincides the best with our inter-sensor distance of 46 mm and 44 mm above the torso front in the case of minimization of the  $Skeel$  for 21 and 32 sensor setups respectively.

The dominant orientations of the clusters for all four figures of merit and both 21 and 32 sensor setups exhibit a mainly radial pattern around the heart. The most frequent orientation among all the orientations of the sensors belonging to one cluster presents the representative orientation of the cluster. But, this way of determining the representative orientation has two drawbacks. The first one is regarding the difference in appearing of that orientation relative to all other belonging to the same cluster. Namely, it could happen that a very little difference determines the orientation of the representative sensor of the cluster. Furthermore, orientations of all the sensors belonging to the cluster are put into the position of the medoid of the cluster. But, positions of the sensors of one cluster cover some area of the torso. This means that an orientation vector of one sensor position is the same when put at the position of medoid with respect to the corresponding three dimensional coordinate system, but not with respect to the surface of the torso. This uncertainty is present in the cluster orientation analysis. So, one has to be aware of the possible uncertainties and therefore of the finding of mainly radial orientations of sensors around the heart.

Taking into account all the similarities/dissimilarities between the optimized setups in this thesis and also the comparison to the setups presented in [51, 84, 101], one can conclude: the “optimal” sensor selection is not unique; quite different sensor sets can perform equally well. This is in agreement with the finding of Lux et al. in [81].



# 5 APPLICATION EXAMPLE II: LORENTZ FORCE EVALUATION

## 5.1 Introduction

Non-destructive material testing and evaluation is a vast interdisciplinary field as well as a challenge due to the variety of applications. Whereas the focus of non-destructive testing (NDT) is to detect and localize anomalies within a specimen, the reconstruction of defect properties (dimensions, shape, structure, composition) and their influence on the material's usability is the focus of non-destructive evaluation (NDE). Defect identification and assessment are very important aspects of quality assurance.

Non-destructive material testing is understood as the non-invasive examination of any type of specimen without changing or altering the properties of the body under test to check whether the specimen contains anomalies. Anomalies are any type of defect or change in the material properties that can be of natural or artificial origin, influencing the usefulness or serviceability of that object [102].

Non-destructive testing has turned from a rather empirical procedure dependent on the experience of the examiners into a more quantitative measurement technique that serves to determine the influence of material anomalies on the structural health of the object [103]. To classify the existing non-destructive testing techniques according to their limitations and not only according to the employed physical phenomenon, a separation in visual, surface and volumetric methods was proposed [104]. However, often these methods have been classified as either electromagnetic or acoustic [105-111].

Recently, a new approach for non-destructive testing of conductive materials was proposed, called Lorentz force eddy current testing (LET) [12]. In contrast to the conventional eddy current testing technique, the magnetic field of a permanent magnet generates eddy currents in electrically conductive specimens, as the specimen is moved with respect to the magnet. The magnetic field caused by the eddy currents yields Lorentz forces, which try to slow down this motion. According to Newton's third axiom, the Lorentz force (LF) is exerted on the permanent magnet in the opposite direction. Material anomalies, such as changes in conductivity, defects, cracks or inclusions, distort the eddy current distribution in the object under test and, consequently, the Lorentz forces measured at the magnetic system. Thus, any defect in the conductive material produces perturbations in the Lorentz force signals. The direct relationship between changes in force and material anomalies can be used to detect defects.

Due to the fact that the computation of transient field problems including the conductor movement is still a complicated and time consuming task, reconstruction of defects in laminated conductive materials based on Lorentz force measurements remains a challenge. The effects on

the Lorentz force profile caused by a defect can be described by a subtraction of the forces acting on the permanent magnet in the defect-free system and the system containing a defect. We call the received difference of force components as the defect response signal (DRS). For the calculation of the defect response signal, we propose a new approximation method (forward solution). First, we introduce a grid of point-like current dipoles placed in the defect region. Next, we calculate the sum of Lorentz forces acting on the current dipoles. This calculated sum directly represents the defect response signal. Based on the approximation method, we are able to formulate a reconstruction algorithm (inverse problem) of a single defect in a laminated bar, i.e. to establish a kernel matrix and to apply a linear inverse scheme to estimate the unknown conductivity distribution in the region of interest (similarly to the approach given in [112]). Thus, for the first time, a method for the reconstruction of the defect geometry based on Lorentz force measurements is developed. This approach has been called Lorentz Force Evaluation (LFE). In this paper, we introduce the forward computation and the inverse solution, compare the new approach to standard finite element computations and apply finally the new technique to both simulated and measured data.

## 5.2 Methodology

### 5.2.1 Problem description

We assume that the permanent magnet described by the magnetization  $\vec{M} = M \hat{z}$  can be replaced by a single equivalent magnetic dipole with the magnetic moment  $\vec{m} = m \hat{z} = MV \hat{z}$  [113]. The dipole is located at the center of gravity (COG) of the magnet  $\vec{r}_0 = x_0 \hat{x} + y_0 \hat{y} + z_0 \hat{z}$ , where  $V$  is the volume of the magnet and  $\hat{x}$ ,  $\hat{y}$  and  $\hat{z}$  represent the unit vectors in a Cartesian coordinate system. A conductive specimen located below the magnetic dipole is moving with a constant velocity  $\vec{v} = v \hat{x}$ . The conductive specimen is approximated by a set of thin Aluminum sheets containing a single parallelepipedic defect (Fig. 5.1). Two types of parallelepipedic defects with respect to the direction of movement of the laminated conductive bar are investigated, a long defect and a wide defect as presented in Fig. 5.1.

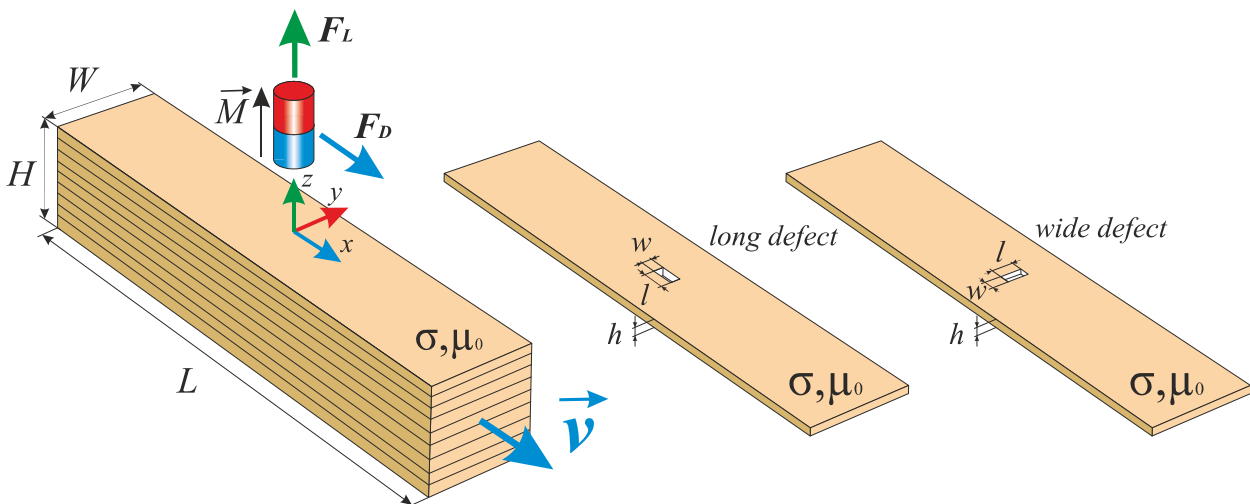


Fig. 5.1 – The laminated conductive bar - a package of thin Aluminum sheets moving with constant velocity below the permanent magnet together with a long and a wide defect used in the analysis.

*Simulation I:* The first simulation is performed for a conductive laminated bar with a long subsurface parallelepipedic defect of dimensions  $w \times h \times l = 2 \text{ mm} \times 2 \text{ mm} \times 12 \text{ mm}$ . The defect is located at the depth  $d = 2 \text{ mm}$  below the top surface of the bar and is positioned longitudinally parallel to the direction of the bar motion (Fig. 5.1). The bar is 50 mm wide ( $W$ ), 50 mm high ( $H$ ) and 250 mm long ( $L$ ), made of Aluminum with an electrical conductivity of  $\sigma = 20.41 \text{ MS/m}$ , is placed 10 mm below a magnetic dipole (magnetic moment  $\vec{m} = 3.5 \text{ Am}^2 \hat{z}$ ). The magnetic moment is equal to the equivalent magnetic moment of the permanent magnet used in the experiment (section 5.3). The bar moves with the velocity  $\vec{v} = 0.16 \text{ m/s } \hat{x}$ .

*Simulation II:* The second simulation is carried out for a wide subsurface defect of the same dimensions as the long defect ( $w \times h \times l = 2 \text{ mm} \times 2 \text{ mm} \times 12 \text{ mm}$ ) but located perpendicularly to the direction of the bar movement. Further setup parameters are the same as in the first simulation, i.e. the defect depth  $d = 2 \text{ mm}$ , the conductivity of the bar  $\sigma = 20.41 \text{ MS/m}$ , the bar size  $W \times H \times L = 50 \text{ mm} \times 50 \text{ mm} \times 250 \text{ mm}$ , the moment of the magnetic dipole  $\vec{m} = 3.5 \text{ Am}^2 \hat{z}$ , its position above the bar  $h_0 = 10 \text{ mm}$ , and the velocity of the moving bar  $\vec{v} = 0.16 \text{ m/s } \hat{x}$ .

### 5.2.2 Forward problem - approximation method

We will consider two systems, a system with and a system without defect. Lorentz forces exerted on the magnetic dipole due to induced eddy currents in the moving bar are equal to  $\vec{F}_N$  and  $\vec{F}_W$  for the defect-free system and the system with defect, respectively. Then, the influence of a defect on the Lorentz force profile can be calculated as  $\vec{F} = \vec{F}_N - \vec{F}_W$ . The subtraction  $\vec{F}$  is called the defect response signal.

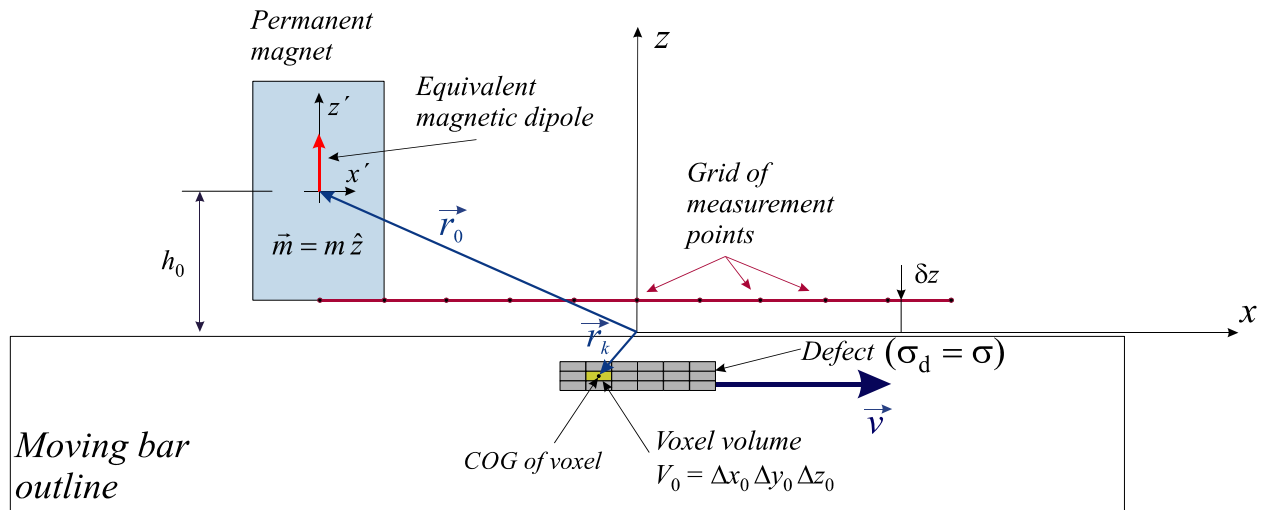


Fig. 5.2 – Modeling of DRS with a set of voxels with current dipoles (approximation method).

The DRS calculation will be restricted to the use of the weak reaction approach (WRA), i.e. the velocity of the moving bar has to be rather small. In this case, the influence of the magnetic field produced by induced eddy currents on the primary field (the field produced by the magnetic dipole) can be neglected [114]. We additionally assume that the electrical conductivity of the

defect equals  $\sigma_d = 0$ , i.e. we consider only ideal defects without eddy currents flowing inside the defect region. The eddy currents distribution in the system with defect can be modeled by superimposing the eddy currents in the system without defect and the distribution of eddy currents in the defect region with changed conductivity  $\sigma_d = \sigma$  flowing exactly in opposite direction. Thus, we can conclude that the eddy currents located in the defect region are responsible for the defect response signal  $\vec{F}$ .

In the defect region we define a uniform grid of conductive volumetric elements (voxels) with conductivity  $\sigma$  (Fig. 5.2).

Since in this study are only considered parallelepipedic defects whose walls are parallel to the walls of the bar, the voxels are small cuboids of volume  $V_0 = \Delta x_0 \Delta y_0 \Delta z_0$ . In each voxel of volume  $V_0$  and conductivity  $\sigma$  flows an induced eddy current described by a current density  $\vec{j}_k$ . Thus, the continuous distribution of eddy currents is replaced by a set of point current dipoles  $\vec{p}_k = \vec{j}_k V_0$  located at the centers of gravity of the corresponding voxels. Taking the WRA into account, the eddy current density  $\vec{j}_k$  in the  $k^{\text{th}}$  voxel of the defect region can be calculated with the help of the Ohm's law for moving conductors, i.e.  $\vec{j}_k = \sigma_k (-\nabla \phi_k + \vec{v} \times \vec{B}_k)$ , where  $\phi_k$  is an electric potential,  $\vec{B}_k$  is the magnetic flux density produced by the magnetic dipole located at  $\vec{r}_0$ :

$$\vec{B}_k = \frac{\mu_0}{4\pi} \left( \frac{3 \vec{m} (\vec{r}_k - \vec{r}_0)}{|\vec{r}_k - \vec{r}_0|^5} (\vec{r}_k - \vec{r}_0) - \frac{\vec{m}}{|\vec{r}_k - \vec{r}_0|^3} \right). \quad (5.1)$$

and  $\vec{r}_k = x_k \hat{x} + y_k \hat{y} + z_k \hat{z}$  denotes the COG of the  $k^{\text{th}}$  voxel.

To determine the electric potential  $\phi_k$ , we assume that the  $z$ -component of induced eddy currents in the conductive bar vanishes. This assumption is motivated by the fact that in the laminated bar, which is a package of conductive sheets (Fig. 5.1), the vertical conductivity  $\sigma_{zz}$  of the whole package is usually much lower than the conductivity of a single sheet. This enforces a dominant eddy currents flow in  $x-y$ -planes. Using  $j_{zk} = 0$  which results in  $\partial \phi_k / \partial z = v B_{yk}$ , we find  $\phi_k$  at the COG of the  $k^{\text{th}}$  voxel as:

$$\phi_k = -v \mu_0 m (y_k - y_0) / [4\pi((x_k - x_0)^2 + (y_k - y_0)^2 + (z_k - z_0)^2)^{3/2}]. \quad (5.2)$$

The Lorentz force exerted on all electric dipoles representing a defect is equal to

$$\vec{F}_d = \int_{V_d} \vec{j} \times \vec{B} dV \approx V_0 \sum_{k=1}^K \vec{j}_k \times \vec{B}_k = \sum_{k=1}^K \vec{p}_k \times \vec{B}_k, \quad (5.3)$$

where  $V_d$  is a defect volume,  $V_0$  is a voxel volume,  $\vec{p}_k$  is a current point dipole located in the COG of  $k^{\text{th}}$  voxel and  $K$  is the number of voxels located in the defect area.

The force equal to the Lorentz force (5.3) but of opposite directionality is exerted on the magnetic dipole representing the permanent magnet. The components of this force are given by expressions (5.4) to (5.6).

$$\vec{F}_x = \sum_{k=1}^K v \sigma_k V \left( \frac{m \mu_0}{4\pi} \right)^2 \left( 3 \frac{(y_k - y_0)^2 + (z_k - z_0)^2}{|\vec{r}_k - \vec{r}_0|^5} - \frac{2}{|\vec{r}_k - \vec{r}_0|^3} \right) \left( 3 \frac{(z_k - z_0)^2}{|\vec{r}_k - \vec{r}_0|^5} - \frac{1}{|\vec{r}_k - \vec{r}_0|^3} \right) \hat{x}, \quad (5.4)$$

$$\vec{F}_y = - \sum_{k=1}^K v \sigma_k V \left( \frac{m \mu_0}{4\pi} \right)^2 3 \frac{(x_k - x_0)(y_k - y_0)}{|\vec{r}_k - \vec{r}_0|^5} \left( 3 \frac{(z_k - z_0)^2}{|\vec{r}_k - \vec{r}_0|^5} - \frac{1}{|\vec{r}_k - \vec{r}_0|^3} \right) \hat{y}, \quad (5.5)$$

$$\vec{F}_z = - \sum_{k=1}^K v \sigma_k V \left( \frac{m \mu_0}{4\pi} \right)^2 3 \frac{(x_k - x_0)(z_k - z_0)}{|\vec{r}_k - \vec{r}_0|^5} \left( 3 \frac{(z_k - z_0)^2}{|\vec{r}_k - \vec{r}_0|^5} - \frac{2}{|\vec{r}_k - \vec{r}_0|^3} \right) \hat{z}, \quad (5.6)$$

where  $|\vec{r}_k - \vec{r}_0| = ((x_k - x_0)^2 + (y_k - y_0)^2 + (z_k - z_0)^2)^{1/2}$  is the distance between the  $k^{\text{th}}$  electric dipole and the magnetic dipole. These components present DRS.

Changing the position of the magnetic dipole  $\vec{r}_0$  according to the measurement grid points  $(\vec{P} : \{x_i, y_i, \delta z\}^T, i=1, \dots, N)$  and taking  $x_0 = x_i$  as well as  $y_0 = y_i$ , we can calculate a set of approximated Lorentz force profiles describing the forward defect response signals.

### 5.2.3 Inverse problem – reconstruction algorithm

We understand the defect reconstruction as the estimation of its size and the position of its center of gravity with respect to the coordinate system assigned to the conductive specimen. Using the idea of relation between defect response signals and the distribution of current dipoles presented in section 5.2.2, we define a region of interest (ROI) with unknown distribution of electrical conductivity where the reconstruction of the defect will be performed. In this study, the ROI is a part of the conductive bar and is defined arbitrary as a fixed cuboidal region in the vicinity of the region where the distortion of measured signals due to an artificial defect is observed. Then, a uniform mesh of volumetric elements (voxels) of constant volume ( $V = \Delta x \Delta y \Delta z$ ) is generated in the ROI (Fig. 5.3).

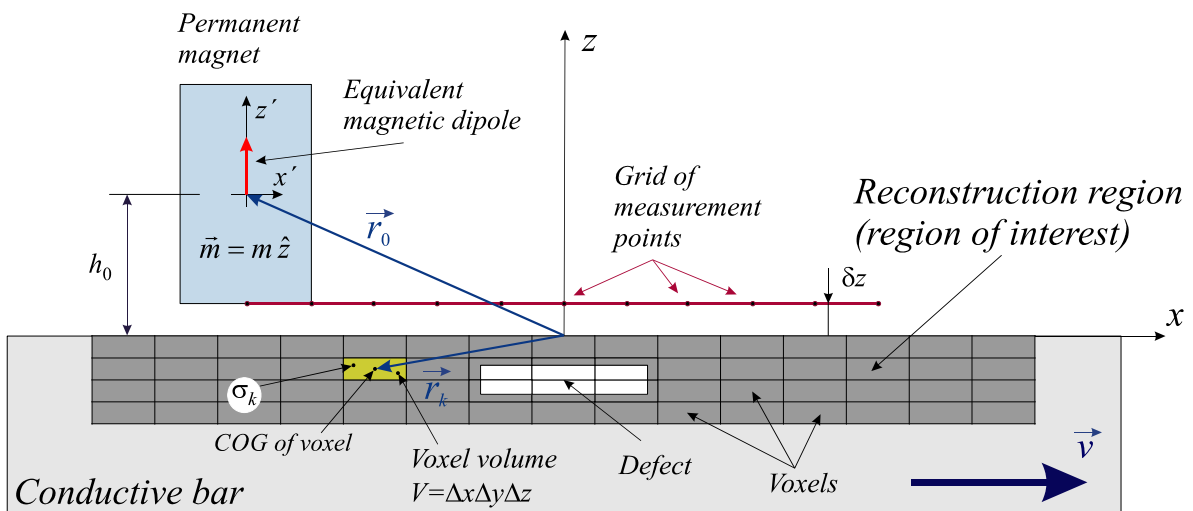


Fig. 5.3 – The region of interest – a set of volumetric elements (voxels) where the defect reconstruction algorithm is applied.

There are no restrictions for the definition of the mesh of voxels in the ROI with respect to the position of defect walls, i.e. voxels can fit or not to the real defect. Unknown constant electrical conductivities  $\sigma_k$  are prescribed to each voxel. The set of all voxel conductivities in the ROI forms a vector  $\{\sigma\} = \{\sigma_k : k = 1, \dots, K\}^T$ , where  $K$  is the total number of voxels in the region. If we would like to reconstruct a defect, we first have to find the conductivity vector  $\{\sigma\}$  in the ROI. Once  $\{\sigma\}$  is known, we apply various conductivity thresholds  $Th$  to find the truncated conductivity distribution  $\{\sigma_{Th}\}$  and to visualize the corresponding cluster of voxels which we interpret as the reconstructed defect. Calculating the weighting average of centers of gravity of voxels in the cluster, we can estimate the position of the defect, with a conductivity  $\sigma_k$  as a weighting factor. Similarly, we can find the size of the reconstructed defect.

The components of the Lorentz force (5.4)-(5.6) are linearly dependent on the conductivity  $\sigma_k$  associated with the corresponding voxel. Thus, the Lorentz force exerted on the magnetic dipole at  $N$  different positions above the conductive bar and conductivities of the  $K$  voxels from the region of interest are linearly related as:

$$[L]_{3N \times K} [\sigma_1 \ \sigma_2 \ \dots \ \sigma_K]^T_{K \times 1} = [F_{1x} \ F_{1y} \ F_{1z} \ \dots \ F_{Nx} \ F_{Ny} \ F_{Nz}]^T_{3N \times 1}, \quad (5.7)$$

where  $[L]_{3N \times K}$  is the kernel matrix. This matrix is

$$[L]_{3N \times K} = \begin{bmatrix} l_{11x} & l_{12x} & \dots & \dots & \dots & l_{1Kx} \\ l_{11y} & l_{12y} & \dots & \dots & \dots & l_{1Ky} \\ l_{11z} & l_{12z} & \dots & \dots & \dots & l_{1Kz} \\ \vdots & \vdots & & & & \vdots \\ \vdots & \vdots & & & & \vdots \\ l_{N1x} & l_{N2x} & \dots & \dots & \dots & l_{NKx} \\ l_{N1y} & l_{N2y} & \dots & \dots & \dots & l_{NKy} \\ l_{N1z} & l_{N2z} & \dots & \dots & \dots & l_{NKz} \end{bmatrix}_{3N \times K}, \quad (5.8)$$

where

$$l_{nkx} = \nu V \left( \frac{m \mu_0}{4\pi} \right)^2 \left( 3 \frac{(y_k - y_0)^2 + (z_k - z_0)^2}{|\vec{r}_k - \vec{r}_0|^5} - \frac{2}{|\vec{r}_k - \vec{r}_0|^3} \right) \left( 3 \frac{(z_k - z_0)^2}{|\vec{r}_k - \vec{r}_0|^5} - \frac{1}{|\vec{r}_k - \vec{r}_0|^3} \right), \quad (5.9)$$

$$l_{nky} = -\nu V \left( \frac{m \mu_0}{4\pi} \right)^2 3 \frac{(x_k - x_0)(y_k - y_0)}{|\vec{r}_k - \vec{r}_0|^5} \left( 3 \frac{(z_k - z_0)^2}{|\vec{r}_k - \vec{r}_0|^5} - \frac{1}{|\vec{r}_k - \vec{r}_0|^3} \right), \quad (5.10)$$

$$l_{nkz} = -\nu V \left( \frac{m \mu_0}{4\pi} \right)^2 3 \frac{(x_k - x_0)(z_k - z_0)}{|\vec{r}_k - \vec{r}_0|^5} \left( 3 \frac{(z_k - z_0)^2}{|\vec{r}_k - \vec{r}_0|^5} - \frac{2}{|\vec{r}_k - \vec{r}_0|^3} \right), \quad (5.11)$$

$k = 1, \dots, K$ ,  $n = 1, \dots, N$  and  $|\vec{r}_k - \vec{r}_n| = ((x_k - x_n)^2 + (y_k - y_n)^2 + (z_k - z_n)^2)^{1/2}$  is the distance between the COG of the  $k^{\text{th}}$  voxel and the  $n^{\text{th}}$  position of the magnetic dipole above the bar.

Equation (5.7) can be written in matrix form as:

$$[L]\{\sigma\} = \{F\}. \quad (5.12)$$

where  $\{\sigma\}$  is a vector containing unknown conductivities associated with voxels from the ROI,  $\{F\}$  is a vector of three-component Lorentz forces measured/calculated at  $N$  measurement points above the conductive bar, and  $[L]$  denotes a kernel matrix.

To find the unknown voxel conductivities, we apply the singular value decomposition of the matrix  $[L]$ :

$$[L]_{3N \times K} = [U]_{3N \times 3N} [S]_{3N \times K} [V]_{K \times K}^T, \quad (5.13)$$

where the columns of  $[U]$  and the columns of  $[V]$  are the left and right singular vectors of  $[L]$ , respectively. The diagonal entries of  $[S]$  are the singular values of the kernel matrix  $[L]$ .

The unknown voxel conductivities  $\{\sigma\}$  can be found by minimizing the difference between the forward calculated data, which is obtained after applying our approximation method, and the measured Lorentz forces at  $N$  points above the specimen. This solution is a minimum norm least squares solution and is obtained using the expression:

$$\{\sigma\} = [L]^+ \{F\}, \quad (5.14)$$

where  $[L]^+ = [V][S]^+ [U]^T$  is a pseudoinverse of the kernel matrix  $[L]$ .

Like most inverse problems, this problem suffers from a lack of stability in the solution: the solution is very sensitive to both noise and *a priori* information used in the inverse analysis. To overcome the loss of stability, we use truncated singular value decomposition (TSVD) of the kernel matrix  $[L]$  approximating it with the matrix  $[\tilde{L}]$  under the constraint that:  $rank([\tilde{L}]) = r$ , i.e. ignoring as many small singular values as necessary. The truncation level  $r$  in this study is chosen as the value which corresponds to the minimum of the normalized root mean square deviation (NRMSD) which is measure of the differences between the force signal calculated for the truncated  $\{\sigma_{Th}\}$  distribution approximating the defect and the measured signal. A variety of other methods for estimating  $r$  can be found in the literature [115-117]. They are mostly suitable for continuous, but not truncated distributions which we use in the interpretation of the reconstructed defect. By taking into account  $r$  singular values, we form the pseudoinverse matrix  $[\tilde{S}]^+$  and calculate unknown conductivities as:

$$\{\sigma\} = [V][\tilde{S}]^+ [U]^T \{F\}. \quad (5.15)$$

If the conductivity values calculated from (5.15) are negative it means that the real current density vector in the voxel is in the opposite direction with the respect to the assumed one in  $\vec{p}_k$ . Therefore, we take as a solution the absolute values of voxel conductivities obtained by (5.15). Additionally, we normalize them using the maximum conductivity found in the ROI yielding finally to a range of conductivities from 0 to 1.

When only one scanning plane with measurement data is available, one can try to solve the inverse problem in a fully three-dimensional source space (ROI). However, this reconstruction approach might require the use of high computational resources, including large memory space and long computation time. To avoid the inversion of very large kernel matrices, we split the

defect reconstruction into three steps. In *Step I*, we take the  $x$ - and  $z$ -components of the Lorentz forces (DRS) along the symmetry line of the bar (the  $y$ -component of the LF equals zero if the defect is located symmetrically in the bar) to find the depth  $z_i$  corresponding to the  $z$ -position of the intermediate plane of the defect. In this case, we use a rectangular grid of voxels distributed on  $x-z$ -plane. The density of voxels grid in the  $z$ -direction is higher than the density in the  $x$ -direction to assure a good  $z$ -localization of the intermediate plane of the defect. In *Step II*, using the same set of DRS as in *Step I* and the found  $z_i$  position of the intermediate plane, we look for the  $x$ -size of the defect. In this step, we use only voxels regularly distributed on the line  $z = z_i$ ,  $y = 0$ . In *Step III*, we use all three components of DRS measured/simulated at the scanning plane and perform the defect reconstruction on the  $x-y$ -plane using rectangular grid of voxels uniformly distributed at  $z = z_i$ .

#### 5.2.4 Reference forward solution

To obtain a reference solution for the direct problem, we apply the finite element method (FEM). The reference solution is computed for two different defects (see section 5.2.1) and serves as a benchmark for the new approximation method. To efficiently model the relative motion between the magnet and the conductor, we apply the logical expression approach (LEA), which enables fast 3D simulations on fixed computational grids [118]. Using LEA, the spatial coordinates of the moving parts are modeled with time-dependent logical expressions (LE). The shapes of the moving parts are determined on the fly by calculating the constraints given by LE and selecting the finite elements within the domains in which the logical expressions are introduced. Because we are only interested in the Lorentz force perturbations caused by defects, we use LEA to model the defect motion. In the moving defect implementation of LEA, the global coordinate system is fixed to the magnet, and LEs are used to model the motion of the defect (Fig. 5.4).

Implementation of the moving defect approach requires a definition of the moving domain within the conductor, where movement of the defect is realized. The moving domain is defined by the size of the defect ( $w \times h \times l$ ), its depth ( $d$ ), and its initial position  $X_{\text{start}}$  (Fig. 5.4). To simulate the defect motion, the electrical conductivity assigned to the moving domain is modified as  $\tilde{\sigma} = \sigma(1 - LE_c)$ , where  $LE_c$  is the logical expression used to model the parallelepipedic defect [118]:

$$\text{here: } LE_c = \begin{cases} 1, & X_{\text{start}} + vt \leq x \leq X_{\text{start}} + l + vt \\ 0, & x < X_{\text{start}} + vt \vee x > X_{\text{start}} + l + vt \end{cases} \quad (5.16)$$

Omitting displacement current and using the magnetic vector potential  $\vec{A}$  ( $\vec{B} = \nabla \times \vec{A}$ ), the following magnetic field equation applies in the reference frame associated with the permanent magnet

$$[\sigma] \left( \frac{\partial \vec{A}}{\partial t} + \nabla \phi - \vec{v} \times \nabla \times \vec{A} \right) + \nabla \times \left( \frac{1}{\mu_0} \nabla \times \vec{A} - \vec{M} \right) = 0, \quad (5.17)$$

where  $\phi$  is the electric scalar potential,  $\vec{M}$  is the magnetization vector of the permanent magnet,  $[\sigma]$  is a diagonal conductivity tensor of the conductor, and  $\mu_0$  is the permeability of the vacuum. We use the diagonal tensor  $[\sigma]$  with  $\sigma_{xx} = \sigma$ ,  $\sigma_{yy} = \sigma$  and  $\sigma_{zz} = 0$  instead of scalar conductivity  $\sigma$ , for modeling the laminated conductive bar and to force vanishing of the  $z$ -component of induced eddy currents in the conductive bar. Instead of using both potentials



$\vec{A}$  and  $\varphi$ , it is more efficient to use the modified vector potential defined as  $\vec{A}^* = \vec{A} - \int \nabla \varphi dt$ . In this case, the electric scalar potential  $\varphi$  can be excluded from (5.17), [119]. Additionally, for small velocities, the time derivative in (5.17) can be neglected. Thus, the transient problem is transformed into a quasi-static one leading to a reduced simulation time [118].

The lateral position of the permanent magnet  $\delta y$  is changing during the simulation to perform the scan of the whole area of the conductor in the  $x - y$  - plane (Fig. 5.4).

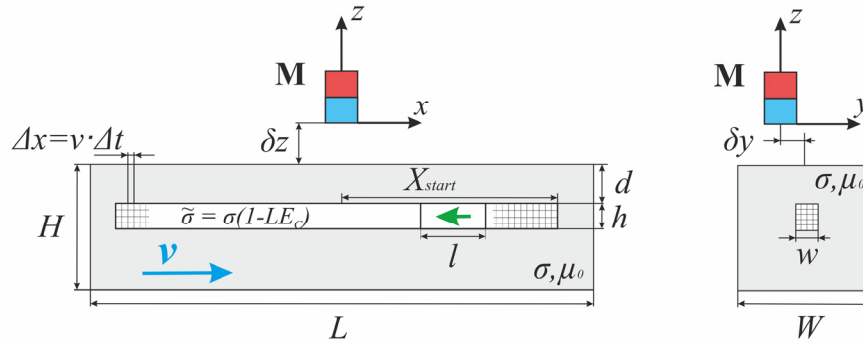


Fig. 5.4 – Implementation of the moving defect approach.  $\Delta x$  is the mesh size in the moving direction, and  $\Delta t$  is the simulation time step.

### 5.3 Experiment

For the validation of the calculations, a model experiment is considered. The permanent magnet is attached to a commercial multi-component force sensor (ME-Meßsysteme GmbH, Hennigsdorf, Germany) [120] and stays in a fixed position. The movement of the set of aluminum thin sheets mounted in a special holder is realized by a linear belt-driven drive. The experimental setup is presented in Fig. 5.5 (see [121] for details).

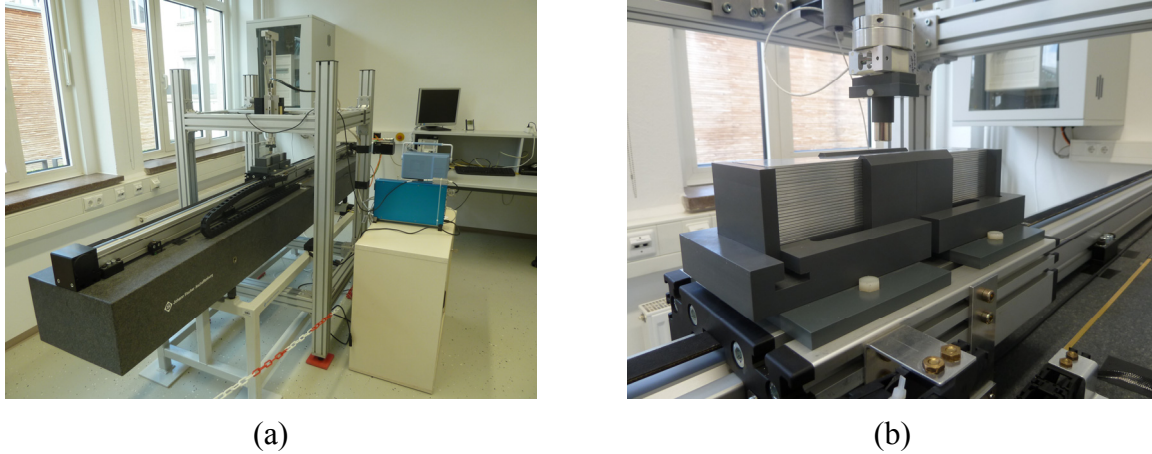


Fig. 5.5 – The experimental setup, comprised of a linear belt-driven drive, a multi-component force sensor, a package of *Al*-sheets, a *y-z*-positioning stage and a data acquisition unit (not shown) (a). The package of *Al*-sheets in the vicinity of the permanent magnet (NdFeB, Ø15mm×25 mm) attached to the multi-component force sensor (b).

The multi-component force sensor, with a measurement range of 3N in *x* – and *y* – direction and 10N in *z* – direction, works on the basis of strain gauges that indicate the deflection of the 3D deformation body caused by the acting force (Lorentz force in our case). The voltage change produced by the force sensor is recorded with a real-time PXI-system (National Instruments Corporation, Austin, Texas) at a sampling rate of 10kHz. The lift-off distance between the permanent magnet and the specimen is adjusted using a microscope table as a planar positioning stage with an accuracy of better than 50nm.

A conductive specimen of dimensions  $W \times H \times L = 50 \text{ mm} \times 50 \text{ mm} \times 250 \text{ mm}$  consists of 25 aluminum sheets with a thickness of 2 mm each. This allows us to introduce artificial defects in easy way in any of the sheet positions. The specimen moves with a constant velocity of 0.5 m/s below the permanent magnet. We place a defect of dimensions  $w \times h \times l = 2 \text{ mm} \times 2 \text{ mm} \times 12 \text{ mm}$  (long defect) in the second sheet, parallel to the direction of motion of the sheet package and with the center in the *x-y*-plane coinciding to the center of the bar surface area. The permanent magnet is positioned 1mm above the specimen. We scan the specimen for different lateral positions of the permanent magnet. The scanning area contains 39 lines in the *y* – interval  $-8 \text{ mm} \leq y \leq 8 \text{ mm}$  with 601 measurement positions per line. The concentration of measurement points along *x*-lines is much higher in the area above the defect than in the rest region (Fig. 5.6).

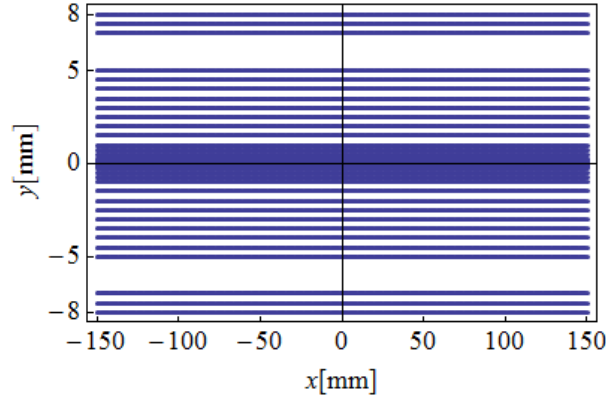


Fig. 5.6 – The scanning area  $\delta z = 1\text{ mm}$  above the specimen without a defect and containing a long subsurface defect.

## 5.4 Results

### 5.4.1 Comparison of the forward computed defect response signals

First, we have performed the comparison of the Lorentz forces calculated for the conductive laminated bar containing a long defect (*Simulation I*). The reference forward solution was obtained using FEM, as indicated in section 5.2.4. The approximated defect response signals were calculated applying our approximation method on a grid of voxels, regularly distributed in the cuboidal defect region with  $\Delta x = 1\text{ mm}$ ,  $\Delta y = 0.1\text{ mm}$  and  $\Delta z = 0.5\text{ mm}$  used as voxels densities. The scanning plane was located at  $h_0 = \delta z = 10\text{ mm}$  above the conductive bar. All three components of the LF were calculated using both methods for non-uniformly distributed points of the scanning area presented in Fig. 5.7a. The density of measurement points was chosen larger in the central part of the scanning plane than in the rest region, i.e. in the vicinity of the region where the defect was expected, to assure a good resolution of the defect response signals recording.

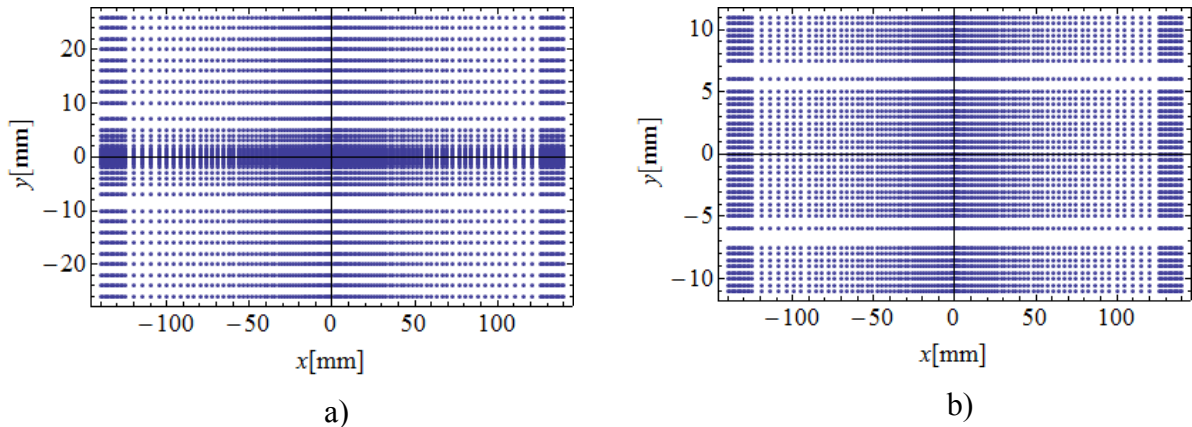


Fig. 5.7 – Scanning area at 10 mm above the conductive specimen for the long crack (a) and wide crack (b). Each dot represents one force calculation point.

Normalized reference defect response signals for the long subsurface defect (*Simulation I*) are calculated as  $\Delta F_\alpha = (F_{\alpha N} - F_{\alpha W}) / (\max(|F_{\alpha N} - F_{\alpha W}|))$ ,  $\alpha \in \{x, y, z\}$ .  $F_{\alpha N}$  and  $F_{\alpha W}$  are components of the LF calculated with the FEM for the conductive bar without and with the defect, respectively. Normalized defect response signals obtained by the approximation method

are calculated as  $\tilde{F}_\alpha = F_\alpha / \max(|F_\alpha|)$ ,  $\alpha \in \{x, y, z\}$ . Distributions of  $\Delta F_\alpha$  and  $\tilde{F}_\alpha$  along one scanning line are presented in Fig. 5.8a-c.  $\Delta F_\alpha$  and  $\tilde{F}_\alpha$ ,  $\alpha \in \{x, y, z\}$ , in the region above the long subsurface defect are presented in Fig. 5.9a-c and Fig. 5.9d-f, respectively.

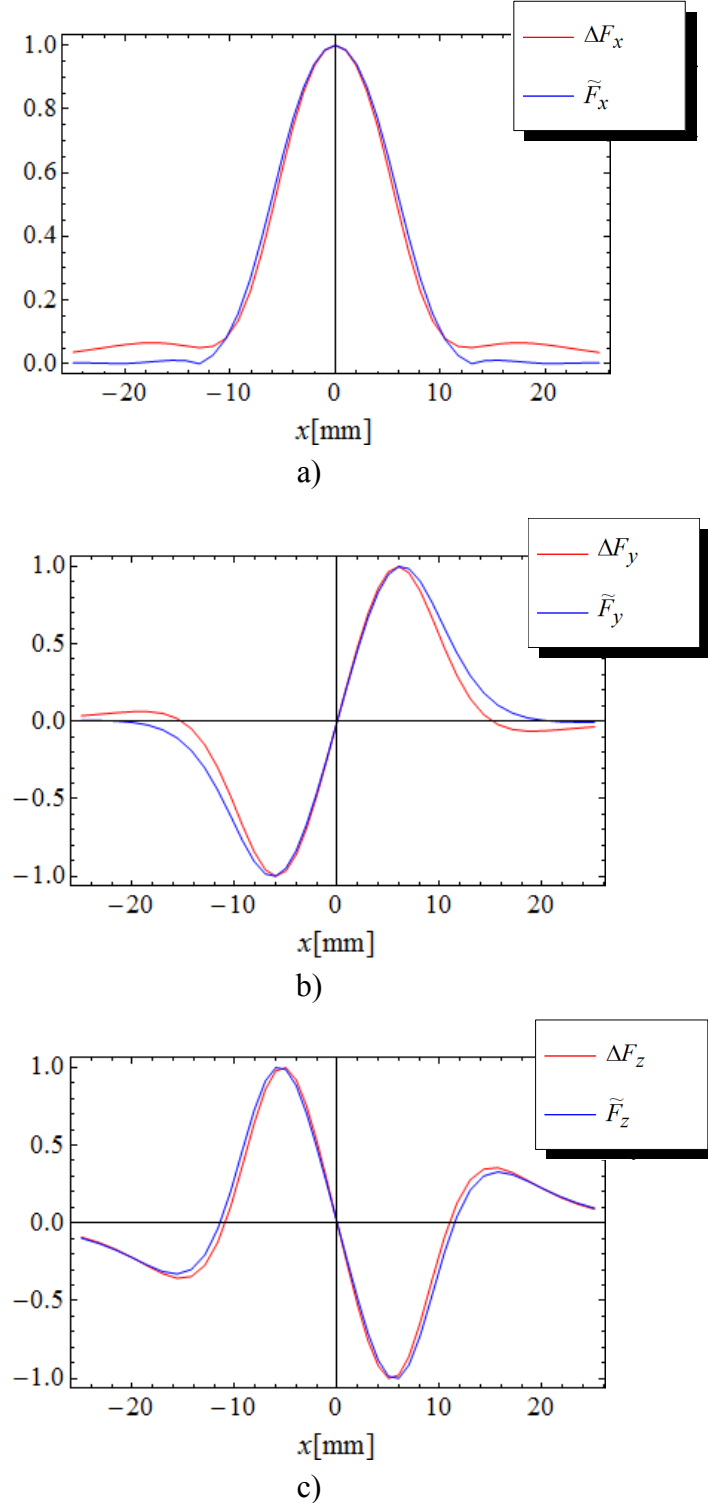


Fig. 5.8 – The distributions of the normalized subtraction of the Lorentz forces in the case of long inner defect predicted by our approximation method (blue line) and computed in COMSOL (red line) of its  $x$  component on the line  $y = 0$  of the scanning plane (a),  $y$  component on the line  $y = -1$  mm of the scanning plane (b) and  $z$  component on the line  $y = 0$  of the scanning plane (c).

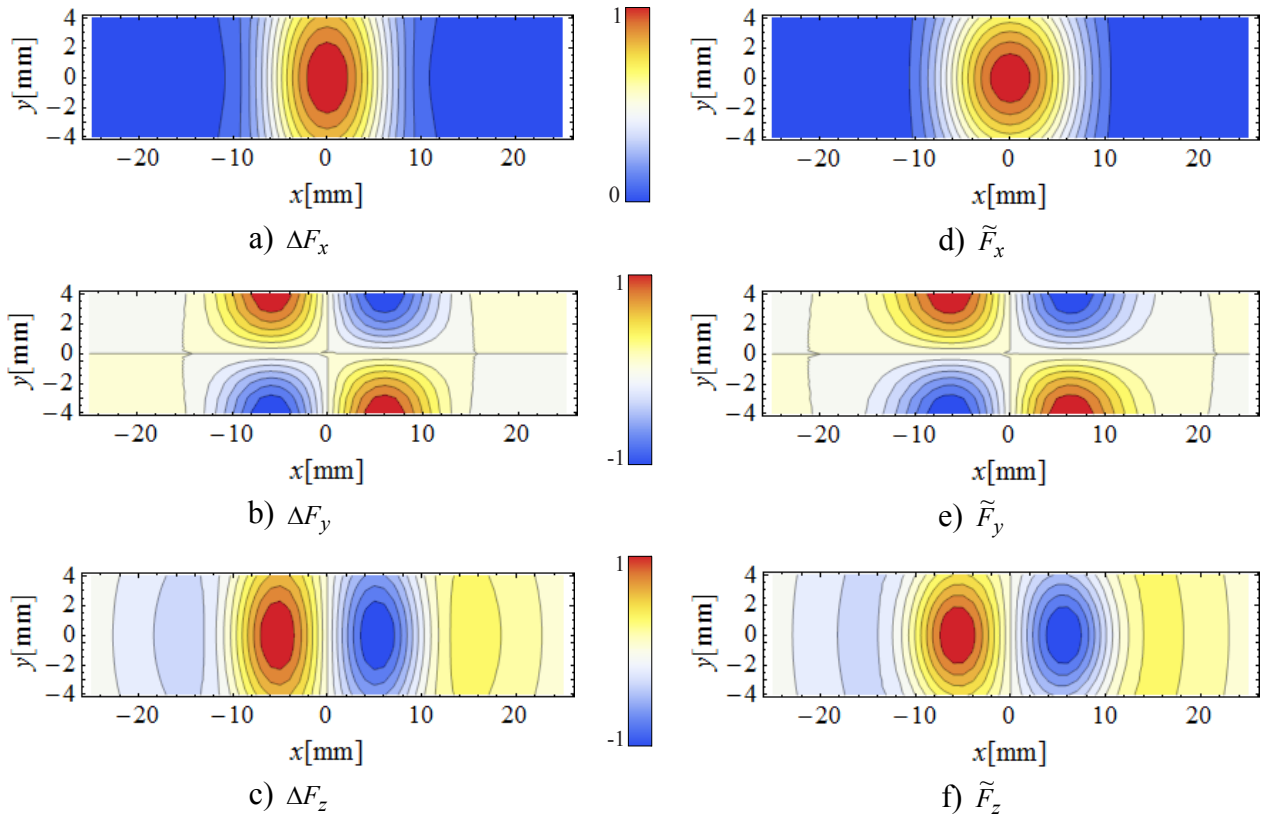


Fig. 5.9 – Simulation I - distributions of reference ( $\Delta F_\alpha$ ) and approximated ( $\tilde{F}_\alpha$ ) normalized defect response signals evoked by the long subsurface defect.

The defect response signals obtained by FEM and predicted by our method were in acceptable agreement: the normalized root-mean-square deviations across all field calculation points in the scanning area are equal to 4.8%, 2.6% and 2.6% for the  $x$ -,  $y$ - and  $z$ -components, respectively.

The second computation of the Lorentz forces was performed for the case of a wide defect (*Simulation II*). A reference solution was again obtained by FEM. The approximated defect response signals of the wide defect was simulated by applying our approximation method on a voxel grid created with density  $\Delta x = 0.1$  mm,  $\Delta y = 1$  mm, and  $\Delta z = 0.5$  mm. All three components of the LF for the FEM and the approximation method were calculated at non-uniformly distributed points of the scanning plane located at  $h_0 = \delta z = 10$  mm above the conductive bar (Fig. 5.7b). Normalized reference defect response signals of the wide defect calculated as  $\Delta F_\alpha = (F_{\alpha N} - F_{\alpha W}) / (\max(|F_{\alpha N} - F_{\alpha W}|))$ ,  $\alpha \in \{x, y, z\}$  are presented in Fig. 5.11a-c in the region above the wide defect. The distributions of the predicted DRS obtained by our approximation method, calculated using  $\tilde{F}_\alpha = F_\alpha / \max(|F_\alpha|)$ ,  $\alpha \in \{x, y, z\}$  are presented in Fig. 5.11d-f. Distributions of  $\Delta F_\alpha$  and  $\tilde{F}_\alpha$ ,  $\alpha \in \{x, y, z\}$ , along one scanning line are presented in Fig. 5.10a-c.

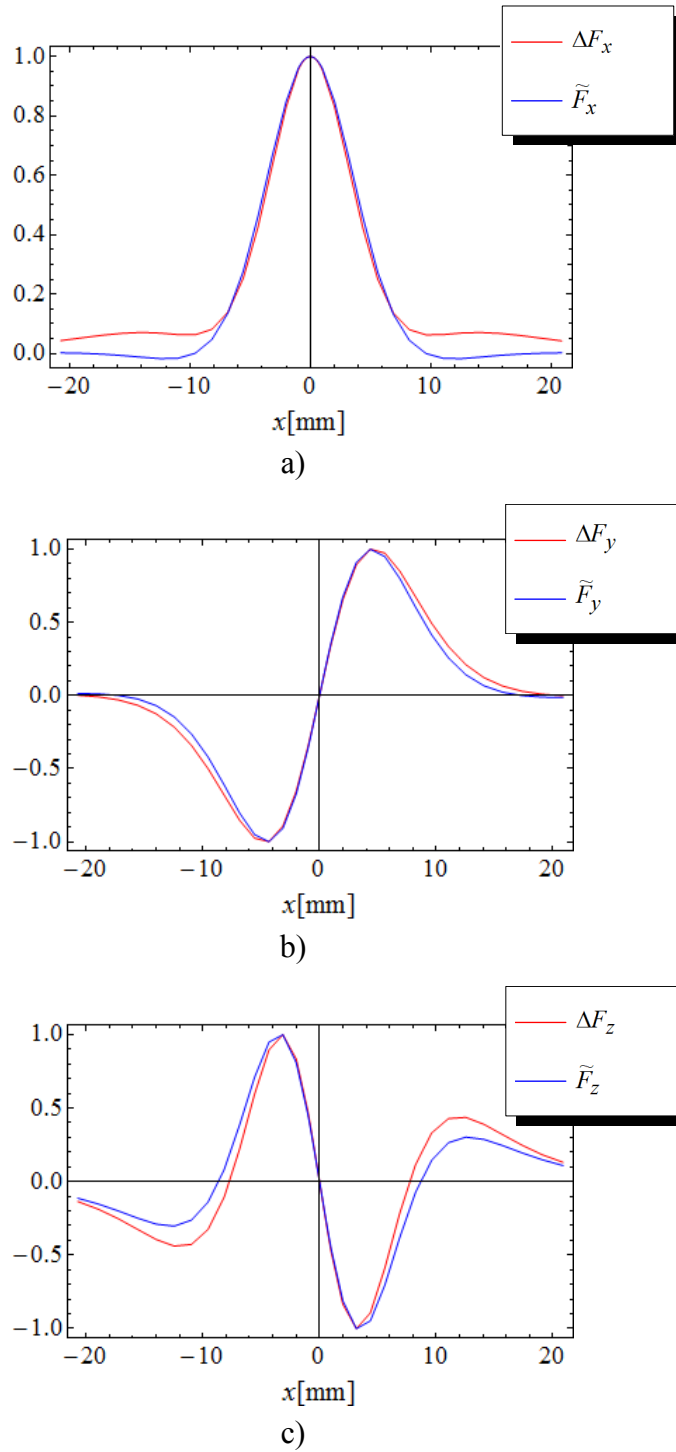


Fig. 5.10 – The distributions of the normalized subtraction of the Lorentz forces in the case of wide inner defect predicted by our approximation method (blue line) and computed in COMSOL (red line) of its  $x$  component on the line  $y = 0$  of the scanning plane (a),  $y$  component on the line  $y = -1$  mm of the scanning plane (b) and  $z$  component on the line  $y = 0$  of the scanning plane (c).

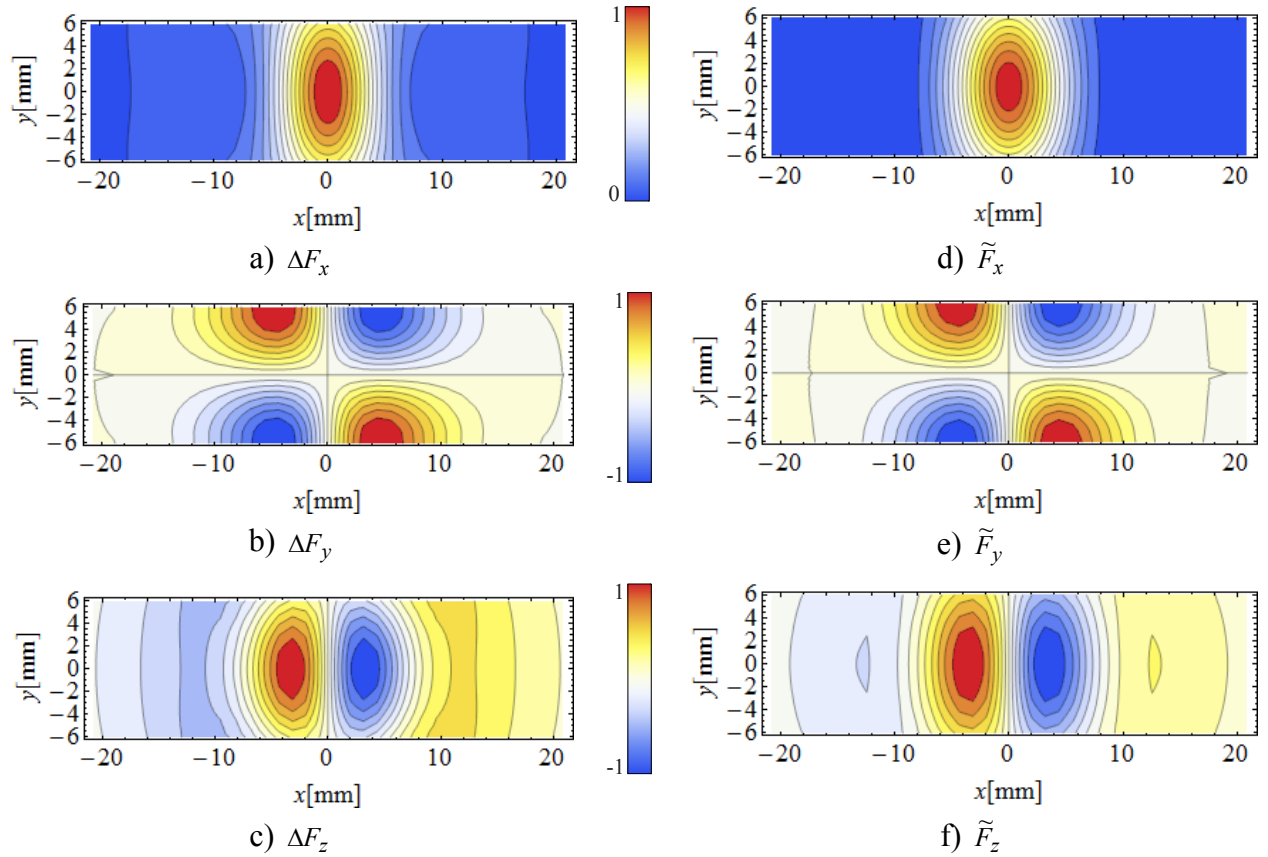


Fig. 5.11 – Simulation II - distributions of reference ( $\Delta F_\alpha$ ) and approximated ( $\tilde{F}_\alpha$ ) normalized defect response signals evoked by the wide subsurface defect.

The DRS obtained by FEM and our method are in the acceptable agreement: the normalized root-mean-square deviations across all field calculation points in the scanning area are equal to 5.9%, 1.7% and 6.7% for the  $x$ -,  $y$ - and  $z$ -components, respectively.

#### 5.4.2 Reconstruction of a simulated long subsurface defect

We use the three steps reconstruction algorithm described in section 5.2.3 to reconstruct the long subsurface defect in the conductive laminated bar.

*Step I:* The  $x$ - and  $z$ -components of the Lorentz forces along the symmetry line ( $y = 0$ ) obtained from FEM (*Simulation I*) for 65 non-uniformly distributed measurement points located in the interval  $-50 \text{ mm} \leq x \leq 50 \text{ mm}$  at  $z = 10 \text{ mm}$  above the bar, are used to define the reference forward solution.

The region of interest contains 2420 voxels in the rectangular area  $-60 \text{ mm} \leq x \leq 60 \text{ mm}$ ,  $-10 \text{ mm} \leq z \leq 0$ .

Setting threshold  $Th$  for the normalized conductivity in the ROI to 50%, we have found for the truncated singular value decomposition the truncation level equals  $r = 45$  corresponds to the minimum of the normalized root mean square deviation between DRS produced by the truncated conductivity distribution and the reference DRS. The corresponding truncated conductivity distribution  $\{\sigma_{50}\}$  is shown in Fig. 5.12. Conductivity distributions are in all figures color-coded using the scale shown in Fig. 5.12c.



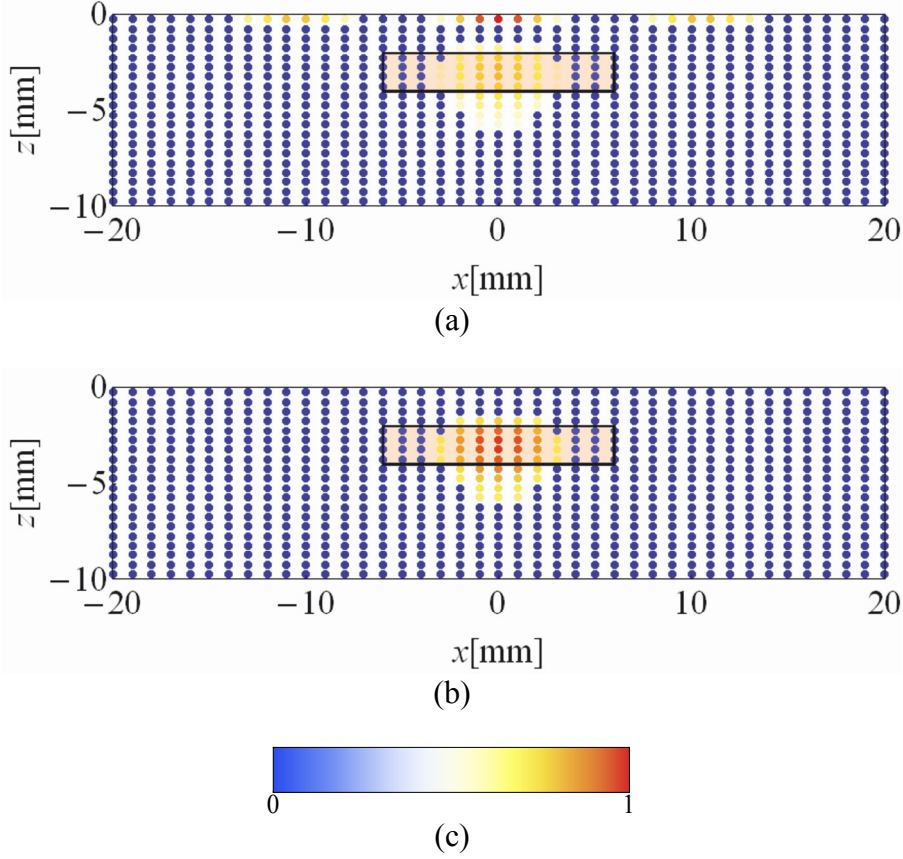


Fig. 5.12 – *Step I* – plane  $x-z$ , distribution  $\{\sigma_{50}\}$  of normalized conductivities for the long subsurface defect (conductivity threshold  $Th = 50\%$ ), spurious solution (a), filtered solution (b). Normalized conductivities are color-coded using the color scale (c).

We observe spurious solutions (artifacts) at the first line of grid of voxels (Fig. 5.12a) i.e. at the line closest to the top surface of the bar. The artifacts can be easily filtered if we use a priori information that only one subsurface defect is sought. The rescaled filtered conductivity distribution is shown in Fig. 5.12b. The cluster of voxels with a color other than blue can be interpreted as a representation of the reconstructed defect in the  $x-z$  plane. Using conductivities from the found cluster in the weighting averaging of voxels COGs, we estimated the  $z$ -position of the intermediate  $z$ -plane of the long defect as  $z_i = -2.78$  mm. This depth position is used in the next two steps.

*Step II:* We take the same DRS as in the *Step I*. At  $z_i = -2.78$  mm, we generate a uniform grid of voxels in the range  $-50 \text{ mm} \leq x \leq 50 \text{ mm}$ . The ROI consists of 200 voxels. Similarly to *Step I*, we set the threshold  $Th$  for the normalized conductivity in the ROI to 50%. The found truncation level in TSVD is equal to  $r = 8$ . Fig. 5.13 shows the truncated normalized conductivity distribution  $\{\sigma_{50}\}$ .

Taking into account only voxels with a color other than blue, the  $x$ -length of the defect is estimated as  $l_e = 11.5$  mm which is almost the length of the real defect. We did not observe any artifacts in the solution.



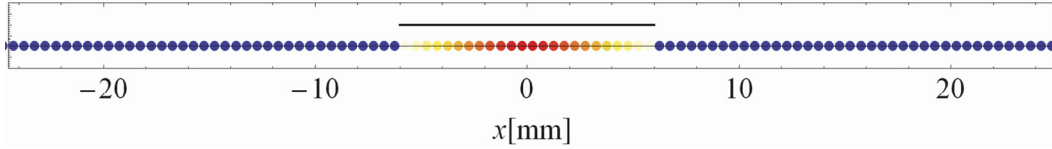


Fig. 5.13 – *Step II* – distribution  $\{\sigma_{50}\}$  of reconstructed normalized conductivities for the long subsurface defect along  $x$  – line at  $z_i = -2.78$  mm . The real defect is indicated as a black line segment.

*Step III:* All three components of the Lorentz force at  $40 \times 19$  measurement points non-uniformly distributed on the plane 10 mm above the bar in the rectangular region  $-25 \text{ mm} \leq x \leq 25 \text{ mm}$ ,  $-4 \text{ mm} \leq y \leq 4 \text{ mm}$ , are used as DRS. The grid of voxels used for the reconstruction contains 800 voxels uniformly generated in the rectangle  $-20 \text{ mm} \leq x \leq 20 \text{ mm}$ ,  $-10 \text{ mm} \leq y \leq 10 \text{ mm}$  at the depth  $z_i = -2.78$  mm . Applying the TSVD procedure with a truncation level  $r = 38$  found for the conductivity threshold  $Th = 50\%$ , a good reconstruction of the defect region in the  $x - y$  – plane at the depth of  $z_i = -2.78$  mm is provided (Fig. 5.14).

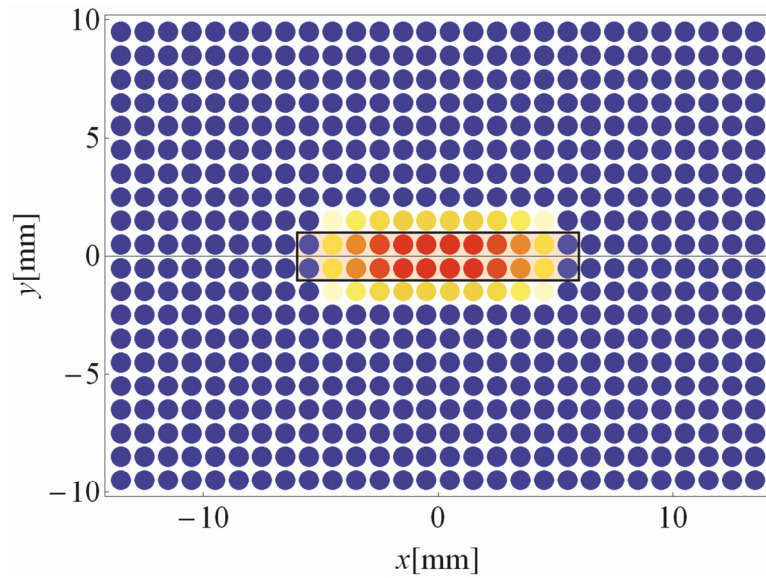


Fig. 5.14 – *Step III* – plane  $x - y$ , distribution  $\{\sigma_{50}\}$  of reconstructed normalized conductivities for the long defect at  $z_i = -2.78$  mm . The real defect is marked with the black rectangle.

The reconstruction of the defect in the  $x - y$  – plane is satisfactory, i.e. the length  $l_e$  and the width  $w_e$  of the defect have been found with an acceptable error:  $l_e = 9 \text{ mm}$ ,  $w_e = 3 \text{ mm}$ . The lateral position corresponding to the COG of the defect was precisely determined.

### 5.4.3 Reconstruction of a simulated wide subsurface defect

Reconstruction of the wide subsurface defect was performed using the same steps as in section 5.4.2.

*Step I:* The  $x$ - and  $z$ -components of the Lorentz forces along the symmetry line ( $y = 0$ ) obtained from FEM (*Simulation II*) for 65 non-uniformly distributed measurement points located in the interval  $-50 \text{ mm} \leq x \leq 50 \text{ mm}$  at  $z = 10 \text{ mm}$  above the bar are used to define the reference forward solution (normalized defect response).

The uniform grid of voxels contains 2420 voxels in the rectangular ROI  $-60 \text{ mm} \leq x \leq 60 \text{ mm}$ ,  $-10 \text{ mm} \leq z \leq 0$ , below the scanning line ( $y = 0$ ). Applying the reconstruction scheme presented in section 5.2.3 with the TSVD truncation level  $r = 33$  found for the conductivity threshold  $Th = 50\%$ , we obtain the defect shape in the  $x-z$ -plane shown in Fig. 5.15 after filtering surface artifacts.

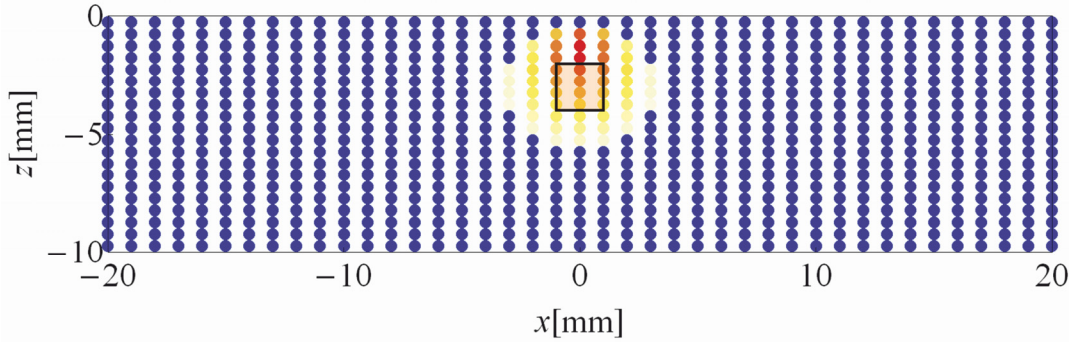


Fig. 5.15 – *Step I* – plane  $x-z$ , distribution  $Th = 50\%$  of color-coded reconstructed normalized conductivities for the wide defect - filtered solution.

Although the reconstructed conductivity  $\{\sigma_{50}\}$  smeared around the real position of the defect in the area twice larger than the real defect, the found weighted  $z_i$  position of the intermediate plane equals  $z_i = -2.11 \text{ mm}$  is in acceptable range of error.

*Step II:* We calculate the DRS at the same points as in the Step I. At the depth  $z_i = -2.11 \text{ mm}$ , in the interval  $-60 \text{ mm} \leq x \leq 60 \text{ mm}$ ,  $y = 0$ , we generate a uniform grid of 364 voxels. Applying the reconstruction scheme presented in section 5.2.3 (with the TSVD truncation level  $r = 45$  found for the conductivity threshold  $Th = 50\%$ ), the defect length of  $1.98 \text{ mm}$  in the  $x$ -direction is successfully determined (Fig. 5.16).

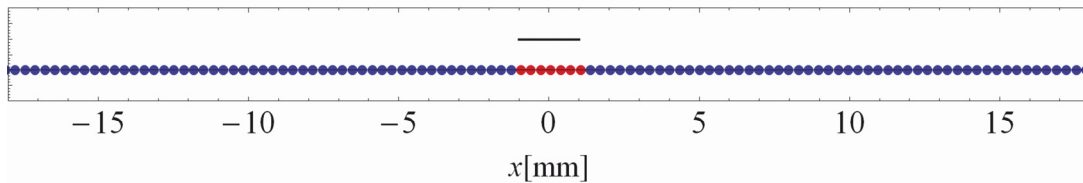


Fig. 5.16 – *Step II* – distribution  $\{\sigma_{50}\}$  of reconstructed normalized conductivities for the wide defect along  $x$ -line at  $z_i = -2.11 \text{ mm}$ . The real defect is indicated as a black line segment.

*Step III:* All three components of the Lorentz force at  $41 \times 29$  measurement points non-uniformly distributed on the plane 10 mm above the bar in the rectangular region ( $-21 \text{ mm} \leq x \leq 21 \text{ mm}$ ,  $-8.5 \text{ mm} \leq y \leq 8.5 \text{ mm}$ ) are used as DRS. The grid of voxels used in the reconstruction contains 1120 voxels uniformly generated in the rectangle  $-21 \text{ mm} \leq x \leq 21 \text{ mm}$ ,  $-14 \text{ mm} \leq y \leq 14 \text{ mm}$  at the depth  $z_i = -2.11 \text{ mm}$ .

The best reconstruction was obtained using in the TSVD procedure a truncation level  $r = 40$  corresponding to the conductivity threshold  $Th = 50\%$ . The found reconstruction of the defect in the  $x - y$ -plane is presented in Fig. 5.17.

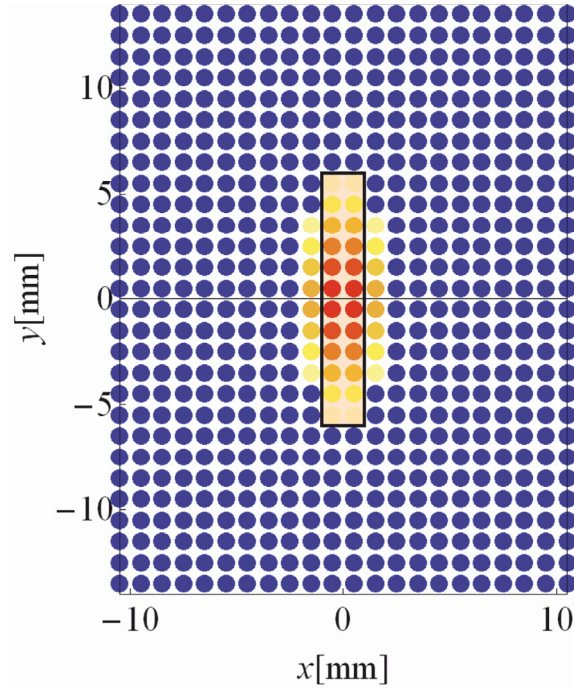


Fig. 5.17 – *Step III* – plane  $x - y$ , distribution  $\{\sigma_{50}\}$  of reconstructed normalized conductivities for the wide defect at  $z_i = -2.11 \text{ mm}$ . The real defect is marked with the black rectangle outline.

The reconstruction of the defect in the  $x - y$ -plane with  $w_e = 3 \text{ mm}$  and  $l_e = 11 \text{ mm}$  is satisfactory, with similar errors as for the long defect.

#### 5.4.4 Reconstruction of a long subsurface defect using the measurement data

The reconstruction algorithm presented in the previous sections has to be verified in the presence of noise. Therefore, we have performed reconstructions of the long subsurface defect using measurement data recorded by the system described in section 5.3.

*Step I:* As the reference forward solution we take the  $x$ - and  $z$ -components of the Lorentz forces along the symmetry line ( $y = 0$ ) at 69 uniformly distributed points in the interval  $-50 \text{ mm} \leq x \leq 50 \text{ mm}$ , 1 mm above the bar extracted from the measurement data (section 5.3). The normalized defect response signals are calculated according the following formulae:

$$\Delta F_{\alpha}(x_i, y_j) = \frac{F_{\alpha jN} - F_{\alpha W}(x_i, y_j)}{\max(|F_{xjN} - F_{xW}(x_i, y_j)|)}, \quad i = 1, \dots, N_x, \quad j = 1, \dots, N_y, \quad \alpha \in \{x, y, z\}, \quad (5.18)$$

$$F_{\alpha jN} = \frac{1}{2} (F_{\alpha N}(x_1, y_j) + F_{\alpha N}(x_{N_x}, y_j)), \quad (5.19)$$

where  $N_x$  and  $N_y$  are the numbers of measurement positions in the  $x$ - and  $y$ -direction, respectively.

The region of interest contains a grid of 2420 voxels defined in the rectangle  $(-60 \text{ mm} \leq x \leq 60 \text{ mm}, -10 \text{ mm} \leq z \leq 0)$ . The filtered truncated conductivity distribution  $\{\sigma_{85}\}$ , found for the truncated TSVD level  $r = 46$ , is shown in Fig. 5.18.

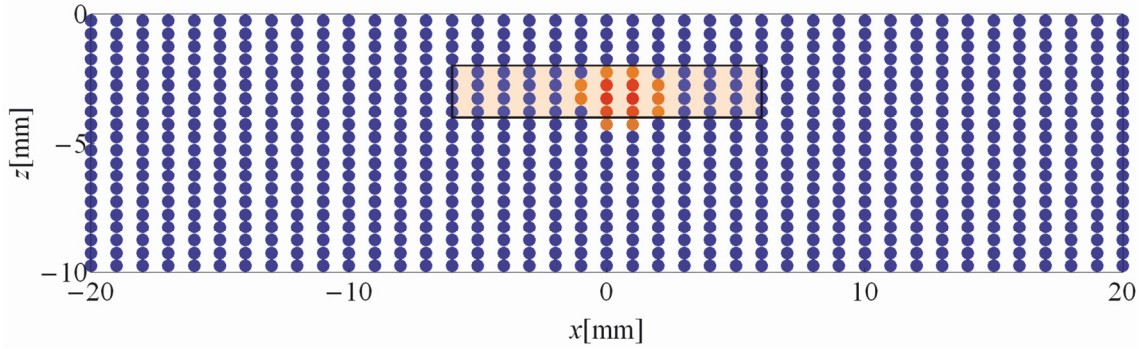


Fig. 5.18 – *Step I* – plane  $x-z$ , distribution  $\{\sigma_{85}\}$  of color-coded normalized conductivities representing the long defect reconstructed from the measurement data - filtered solution.

The distribution  $\{\sigma_{85}\}$  forms a highly concentrated cluster of voxels with high conductivities around the center of the defect. Although the  $x$ -length of the reconstructed defect is much too short, the depth of the defect represented by the position of the intermediate plane ( $z_i = -3.0 \text{ mm}$ ) is found correctly.

*Step II:* We used the same normalized DRS as in the Step I. Using estimated position of the intermediate plane,  $z_i = -3.0 \text{ mm}$ , we generate new grid of 261 regularly distributed voxels along the line:  $y = 0$ ,  $-50 \text{ mm} \leq x \leq 50 \text{ mm}$ . Applying the reconstruction scheme presented in section 5.2.3 (with a truncation value  $r = 5$  for the conductivity threshold  $Th = 85\%$ ), we obtained the defect of 12 mm length but with a center shifted about 0.5 mm to the left comparing the original position of the defect (Fig. 5.19).

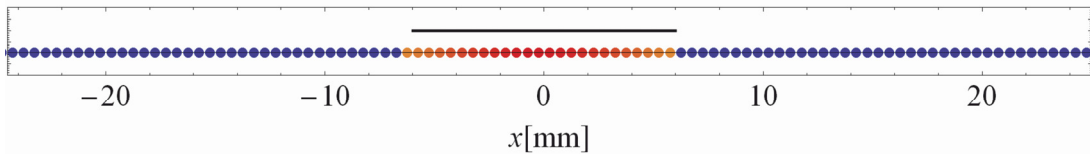


Fig. 5.19 – *Step II* – distribution  $\{\sigma_{85}\}$  of reconstructed normalized conductivities for the long defect along  $x$ -line at  $z_i = -3.0 \text{ mm}$  (measurement data). The real defect is indicated as a black line segment.

*Step III:* Here, we use as reference signals the DRS calculated according (5.18)-(5.19) for all three components of the Lorentz force at  $40 \times 81$  measurement points non-uniformly distributed on the plane 1mm above the bar in the rectangular region  $-25 \text{ mm} \leq x \leq 25 \text{ mm}$ ,  $-4 \text{ mm} \leq y \leq 4 \text{ mm}$ .

The region of interest is located at  $z_i = -3.0 \text{ mm}$  and consists of a rectangular grid of 800 voxels, uniformly distributed in the area  $-20 \text{ mm} \leq x \leq 20 \text{ mm}$ ,  $-10 \text{ mm} \leq y \leq 10 \text{ mm}$ . The TSVD procedure (with a truncation level  $r = 2$  found for the threshold  $Th = 85\%$ ) produces a defect map presented in Fig. 5.20.

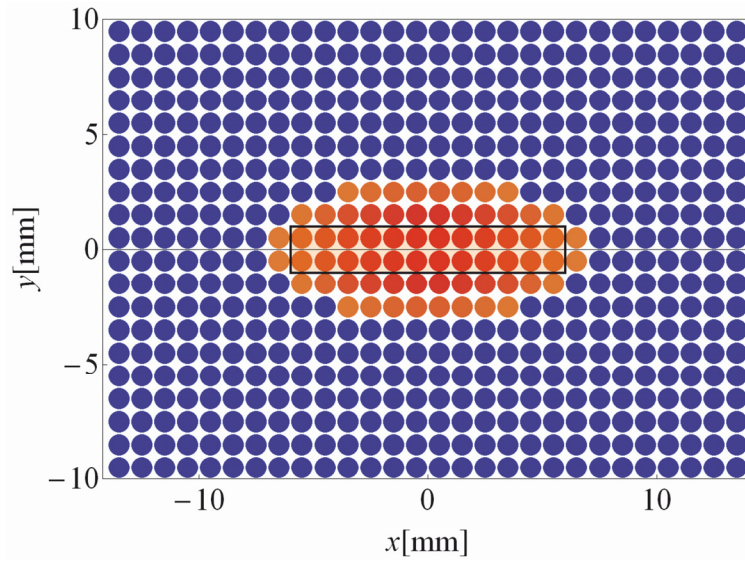


Fig. 5.20 – *Step III* – plane  $x - y$ , distribution  $\{\sigma_{85}\}$  of reconstructed normalized conductivities for the long defect at  $z_i = -3.0 \text{ mm}$  (measurement data). The real defect is marked with the black rectangle.

This step, applying the truncation level  $r = 2$ , provides a truncated conductivity distribution which is regularly smeared around the defect ( $l_e = 13 \text{ mm}$ ,  $w_e = 5 \text{ mm}$ ). The found truncation level ( $r = 2$ ) shows that the reference DRS is influenced by noise. The use of only a very few singular values in the reconstruction algorithm would enable a proper interpretation of reconstructed conductivity distribution.



### 5.5 Discussion

We have demonstrated the application of a novel fast forward method for the computation of the eddy current and magnetic field distribution in a laminated conductor which has been moving with respect to a fixed permanent magnet. This new approach has further been used to introduce a new inversion scheme for the Lorentz force evaluation based on the analysis of simulated and measured data.

The quality of defect reconstruction has been found to depend on parameters of the defect under consideration, in particular on the position of the defect with respect to the moving direction of the specimen and the signal-to-noise ratio of the data. Using a priori information of the defect (i.e. assuming only a single, subsurface defect), it was possible to find a conductivity threshold which together with an artifacts filter gave an appropriate interpretation of the estimated conductivity distributions. The corresponding truncation level used in TSVD has been determined using the minimum normalized root mean square deviation criterion calculated for the truncated conductivity distribution. This approach has been found to work more effective in our problem than for example the L-curve technique which can be found in the literature [117].

Reconstructions in the  $x-z$ -plane have been qualitatively correct, i.e. the subsurface defect has been found in the proper region. The reconstruction quality strongly depends on the position of the defect with respect to the moving direction of the bar. For long defects, we have received focal concentrations of voxels representing the defect which  $x$ -size was much smaller than the original defect length. However, the defect intermediate plane position calculated as a weighted average of voxels COGs has been estimated correctly for simulated as well as for measurement data. In contrary, for the wide defect, the estimated conductivity distribution was smeared around the original defect covering much more area than the original defect. In this case, the position of a defect intermediate plane has been determined with less accuracy and was shifted towards the surface of the bar. Generally, it is significantly harder to determine the depth of a defect than to locate its lateral position when only measurement values in one plane above the specimen are available. The reason is the difficulty to dissect the effect of depth from that of source strength. In the future, scanning in more than one plane will be performed. The other problem which should be study in details is the use of depth weighting techniques which compensate a bias toward superficial sources. They can be applied to those reconstructions where the defect is localized close to the bar surface (wide defect) to correct the positioning of the intermediate reconstruction plane.

The length of the defect in the  $x$ -direction was successfully determined (*Step II* of the reconstruction algorithm) in all three cases although the used conductivity threshold strongly depends on the noise level ( $Th = 50\%$  for simulated,  $85\%$  for measured data).

Reconstructions in the  $x-y$ -plane using simulated data (long and wide defect) were correct, fitting almost perfectly to the defect shape. For the measured data, the use of a high threshold conductivity ( $85\%$ ) combined with a small number of singular values in TSVD has produced a smeared  $x-y$ -distribution of voxels representing the long defect. This is the result of a relatively high noise in the measured signals. The noise yields a form of oscillations of DRS with amplitudes of about  $20\%$  of the useful signals. The reason for these oscillations has not been found so far.

The regions of interest (ROI) used in the reconstructions have been chosen using an information about the position of DRS in the recorded/simulated signals and their duration. The size of ROI and the density of voxels are set in arbitrary way. In the future, it is necessary to study the influence of these parameters on the quality of the reconstruction as well.

## 6 CONCLUSIONS AND OUTLOOK

Linear inverse problems arise in a wide range of applications. These problems are usually ill-conditioned, i.e. solution components are very sensitive to small changes in the initial data. The existence of a proper figure of merit is an imperative for a successful measuring of ill-conditioning of linear inverse problems. In this thesis, theoretical aspects of three existing measures of ill-conditioning are considered and two new measures are proposed.

The most widely used indicator of ill-conditioning is a condition number with a respect to the  $L_2$  norm. As a norm-wise condition measure, it gives the error bound of the worst conditioned component in the solution vector and therefore overestimates a condition of a kernel matrix. Computation of the condition number with respect to the  $L_2$  norm requires computation of the singular values of the kernel matrix of a corresponding linear inverse problem. This measure of conditioning strongly depends on the smallest singular value of a matrix.

When solving linear inverse problems, engineers and scientists are aware of changing of the condition number with respect to the  $L_2$  norm with matrix dimensions. But, it is found that the increment/decrement of the condition number with respect to the  $L_2$  norm is dependent on over- or underdetermination of the linear inverse problem. Namely, exclusion of sensors from a sensor array decreases the condition number with respect to the  $L_2$  norm only in the case of underdetermined linear inverse problem. Similarly, when the problem is overdetermined, exclusion of sources from a grid of dipoles decreases the condition number with respect to the  $L_2$  norm. Influence of changing of a number of sensors in overdetermined problems and number of sources in underdetermined problems depends on particular singular values of the corresponding kernel matrix.

Skeel condition number is the second considered measure of conditioning. When used in overdetermined linear inverse problems, it is invariant under column scaling. Row scaling of a matrix does not affect the *Skeel* condition number in underdetermined linear inverse problems. The *Skeel* condition number cannot be much larger, but can be much smaller than the condition number with respect to the  $L_2$  norm. Scaling of a matrix and reordering of linear equations in the system do not change the value of the Skeel condition number.

Reduction of the dependency on the smallest singular value and increment in the numerical stability of the evaluation comparing to the condition number with respect to the  $L_2$  norm, is achieved through the inverse average decay of singular values,  $\rho$ . A relation between  $\rho$  and the steepness of the slope of singular values is derived.  $\rho$  represents the inverse of area under the curve of singular values of a kernel matrix. The larger is the area under the curve, the smaller is

the  $\rho$  and consequently the better conditioned linear inverse problem. This measure of conditioning is not invariant under scaling.

Based on geometrical properties of rows/columns of a kernel matrix, two new error measures are developed. The first one measures dependency between rows of a kernel matrix in underdetermined linear inverse problems and is referred to as rows dependency  $RD$ . When used in overdetermined linear inverse problems, it measures a dependency between columns of a matrix and is referred to as columns dependency  $CD$ . Different from the condition number with respect to the  $L_2$  norm, computation of  $RD$  does not require singular value decomposition of a matrix. Because a size of a matrix does not influence the value of  $RD$ , this figure of merit enables comparison of kernel matrices of different sizes. We do know that the multiplication of all elements of a row by the same value influences only the norm of a row vector, but not the angles to other rows. Thus,  $RD$  is independent of row scaling. In the same way,  $CD$  is independent on column scaling. This error measure allows for selecting the most linearly independent rows and performing the estimation with these rows only. This reduces computational costs and improves a stability of linear inverse solution.

The second developed figure of merit  $\xi$  is based on the mean of the products of the lengths of the kernel matrix column vectors of an overdetermined linear inverse problem and cosines of the angles between those vectors and corresponding rows of a matrix pseudoinverse. When used in underdetermined linear inverse problems, it uses the lengths of row vectors of a kernel matrix and angles between these vectors and corresponding rows of a pseudoinverse of a kernel matrix. Different from the condition number with respect to the  $L_2$  norm, it does not predict the sensitivity on perturbations of the worst conditioned solution component. In contrast to the another proposed novel figure of merit, i.e. the dependency between rows/columns of a kernel matrix which can be computed using the data in the matrix only, calculation of the figure of merit  $\xi$  requires determination of the pseudoinverse of the kernel matrix. By a proper selection of a scaling matrix, this figure of merit can be considerably reduced.

Numerical stability, indication of the worst conditioned component or of a mean conditioning of all components, requirement for pseudoinverting of a matrix, affection by scaling or by matrix dimensions, make one of the figures of merit favorable for measuring of conditioning of the linear inverse problem.

Monoaxial sensors are usually equidistantly and in parallel arranged in sensor arrays. Random variations of sensor orientations usually increase the smallest singular value of the kernel matrix, while the largest singular value remains almost unperturbed. But, it is not always the case that random variations of monoaxial parallel sensors increase the smallest singular value and improve the condition of the linear inverse problem. Therefore, a strict mathematical condition, under which random variations of perfect in parallel sensor orientations lead to an increment of the smallest singular value of a kernel matrix, is derived. The condition relates the smallest singular value of a kernel matrix, perturbation matrix and a projection matrix onto the column/row space of a kernel matrix in over/underdetermined linear inverse problems.

When random variations of sensor orientations do not a priori lead to an increment of the smallest singular value of a kernel matrix, one could attempt to calculate the probability of getting an increment. A contribution to a better prediction of improvements in the condition of linear inverse problems for randomly varied sensor orientations and other random changes in the inverse problem setup is given through a derivation of sharper perturbation bounds in perturbation expansion of the smallest singular value. Bounds are specifically defined for over- and underdetermined linear inverse problems. Since the derivation can be applied to all singular



values of the matrix, an insight into a change not only of the condition number with respect to the  $L_2$  norm, but also of the figure of merit  $\rho$ , can be provided.

Theoretical considerations of conditioning of linear inverse problems are applied to two examples: magnetocardiography and Lorentz force eddy current testing. Optimization of 21 and 32 magnetic sensors in a vest-like sensor setup is done minimizing four different figures of merit: condition number with respect to the  $L_2$  norm,  $CN$ , *Skeel* condition number, inverse average decay of singular values  $\rho$  and a novel figure of merit  $\xi$ . Optimized sensor setups obtained after minimization all four figures of merit show non-uniform distribution of sensors on the whole torso surface. Placement of sensors on the back of the torso but not only on the front improves the condition of the linear inverse problem. Different to  $\rho$  and  $\xi$ , minimization of  $CN$  and *Skeel* produce more sensors on the front than on the back of the torso in both the 21 and 32 sensors setups. Setups obtained minimizing  $CN$  and *Skeel* are better correlated to the excitation pattern exemplified by the reflection of the Wilson lead sequence. Furthermore, minimization of  $CN$  and *Skeel* leads to a denser package of front sensors in the area above the heart comparing to the minimization of  $\rho$  and  $\xi$ . These more densely distributed sensors above the heart likely lead to an increase in information content. While in [74] the magnetic sensors on the back of the torso are mostly positioned on its left part, optimized sensor arrays in this thesis contain magnetic sensors also on the back right side. Minimization of  $CN$ , *Skeel* and  $\xi$  provides more evenly distributed sensors on the back of the torso, while  $\rho$  has a higher concentration of sensors over the heart on the back side of the torso.

The dominant orientations of the clusters for all four figures of merit and both 21 and 32 sensor setups exhibit a mainly radial pattern around the heart. Taking into account all the similarities/dissimilarities between the optimized setups in this thesis and also the comparison to the setups presented in literature, one can conclude that quite different sensor setups can perform equally well. In other words, the optimal sensor selection is not unique.

This work considers only the kernel matrix, without solving the corresponding linear inverse problem. A continuation of this work could be an insight into localization accuracy when different magnetometer arrays are used, obtained by minimizing of different figures of merit.

Based on the determination of conductivity and on a dipole model like in magnetocardiography, a new method for non-contact, non-destructive evaluation of solid conductive materials, termed Lorentz force evaluation, is introduced. Relative motion between a permanent magnet and a solid conductive specimen produces eddy currents inside the bar. When a bar has a defect, a distribution of eddy currents can be modeled as a superposition of eddy currents in the system without defect and the distribution of exactly opposite eddy currents flowing in the defect region with changed conductivity (equal to the conductivity of the bar in the case of zero conductivity of the defect). So, an influence of a defect with changed conductivity on a Lorentz force profile exerted on the magnetic dipole due to eddy currents is equal to the subtraction of the Lorentz forces coming from a defect-free system and the system with a defect. This signal is called defect response signal. A novel forward computation of the defect response signal is introduced. It employs a three-dimensional finite volume discretization and approximates a defect with an electric dipole in each voxel. Approximate solution is compared with the solutions from detailed finite element models. A difference in Lorentz force ranges between 1.7% and 6.7%, indicating a sufficient performance of the novel method.

Based on this novel forward computation, a method for the reconstruction of defect geometries based on Lorentz force measurements is developed. Method is applied in reconstruction of subsurface long and wide parallelepipedic cracks using the forward solutions from the finite

element model and of a subsurface long defect using measurement data. Solving of an inverse problem in a fully three-dimensional source space might require the use of high computational resources, including large memory space and long computation times. In order to avoid the inversion of very large kernel matrices, a defect reconstruction is split into three steps: determination of a depth of the intermediate plane of a defect, determination of the length of a defect in a moving direction of a specimen and as a third step, reconstruction in  $x-y$ -plane, parallel to the upper surface of the bar and the scanning plane as well.

Determination of the depth of the long defect was precisely determined using both measurement and data obtained by finite elements method. In the case of wide defect, a depth of its intermediate plane is slightly moved towards the surface, but still being in an acceptable range of error (less than 1mm). When determining a depth of an intermediate plane of a subsurface defect, an *a priori* knowledge has to be employed. One should know that only one defect exists in the specimen and also the type of the crack (surface/subsurface). A length of a defect in a direction of movement of a solid bar was successfully determined in all three cases. There is only a shift to the left of a center of a long defect when inverting measurement data of about 0.5mm. Reconstruction in the  $x-y$ -plane is satisfactory too. Long subsurface defect using FEM data shows an error of 1mm in  $y$ -direction and 3mm in  $x$ -direction. Wide defect has an error of just 1mm in both directions. Reconstructed conductivities in the case of long subsurface defect obtained using measurement data are regularly smeared around the defect and with an acceptable error.

Applying this novel forward and inverse methodology, Lorentz Force Evaluation can be used to reconstruct defect geometries in conductive materials. Nevertheless, application of different inversion algorithms, regularization techniques or usage of a number of permanent magnets instead of just one could improve reconstruction accuracy in Lorentz Force non-destructive technique.

## REFERENCES

- [1] F. Natterer. The mathematics of computerized tomography, Teubner, Stuttgart, 1986.
- [2] J. Hadamard. Sur les problemes aux derivees partielles et leur signification physique, Princeton University Bulletin, 13 (1902).
- [3] J. Hadamard . Lectures on the Cauchy problem in linear partial differential equations, New Haven, CT Yale University Press, 1923.
- [4] R. Courant and D. Hilbert. Methods of mathematical physics, Interscience, 2 (1962).
- [5] R. Eichardt and J. Haueisen. Influence of sensor variations on the condition of the magnetostatic linear inverse problem, IEEE Transactions on Magnetics, 46 (2010) 3449–3453.
- [6] U. Leder, J. Haueisen, M. Huck and H. Nowak. Noninvasive imaging of arrhythmogenic left-ventricular myocardium after infarction, LANCET, 352 (1998) 1825.
- [7] H. Kwon, K. Kim, YH Lee, JM Kim, KK Yu, N. Chung and YG Ko. Non-invasive magnetocardiography for the early diagnosis of coronary artery disease in patients presenting with acute chest pain, Circulation Journal, 74 (2010) 1424-1430.
- [8] A. Kandori, K. Ogata, T. Miyashita, H. Takaki, H. Kanzaki, et al. Subtraction magnetocardiogram for detecting coronary heart disease, Annals of Noninvasive Electrocardiology, 15(2010) 360-368.
- [9] D. Di Pietro Paolo, H. Mueller, M. Goernig, J. Haueisen and S. Erne. Cardiac signal extraction in patients with implantable cardioverter defibrillators, Medical Engineering & Physics, 31 (2009) 1087-1094.
- [10] G. Bison, N. Castagna, A. Hofer, P. Knowles, JL Schenker, M. Kasprzak, et al. A room temperature 19-channel magnetic field mapping device for cardiac signals, Applied Physics Letters, 95(2009) 173701.
- [11] S. Lau, R. Eichardt, L. Di Rienzo and J. Haueisen. Tabu search optimization of magnetic sensor systems for magnetocardiography, IEEE Transactions on Magnetics, 44 (2008) 1442-1445.
- [12] H. Brauer and M. Ziolkowski. Eddy current testing of metallic sheets with defects using force measurements, Serbian Journal of Electrical Engineering, 5 (2008) 11-20.
- [13] S. Chandrasekaran and I. C. F. Ipsen. On the sensitivity of solution components in linear systems of equations, SIAM Journal on Matrix Analysis and Applications, 16 (1995) 93-112.
- [14] J. Rohn. New condition numbers for matrices and linear systems, Computing, 41 (1989) 167-169.

- [15] M. Arioli, J. W. Demmel and I. S. Duff. Solving sparse linear systems with sparse backward error, *SIAM Journal on Matrix Analysis and Applications*, 10 (1989) 165-190.
- [16] D. J. Higham and N. J. Higham. Backward error and condition of structured linear systems, *SIAM Journal on Matrix Analysis and Applications*, 13 (1992) 162-175.
- [17] D. J. Higham. Condition numbers and their condition numbers, *Linear Algebra and its Applications*, 214 (1995) 193-213.
- [18] D. Chu, L. Lin, R. C. E. Tan and Y. Wei. Condition numbers and perturbation analysis for the Tikhonov regularization of discrete ill-posed problems, *Numerical Linear Algebra with Applications*, 18 (2011) 87-103.
- [19] D. Weinstein, L. Zhukov and C. Johnson, Lead-field bases for electroencephalography source imaging, *Annals of Biomedical Engineering*, 28 (2000) 1059-1064.
- [20] A. Deif. Sensitivity analysis in linear systems, Berlin-Heidelberg-New York, Springer 1986.
- [21] C. Lee, C. H. Im, K. Choi and H. Jung. Estimation of solution accuracy from leadfield matrix in magnetoencephalography, *IEEE Transactions on Magnetics*, 43 (2007) 1701-1704.
- [22] L. Rouve, L. Schmerber, O. Chadebec and A. Foggia. Optimal magnetic sensor location for spherical harmonic identification applied to radiated electrical devices, *IEEE Transactions on Magnetics*, 42 (2006) 1167-1170.
- [23] C. Lee, K. An, B. Kim, C. Im, H. Jung. Estimation of solution accuracy in magnetoencephalography by using the condition number from a leadfield matrix, *Proceedings of the World congress on Medical Physics and Biomedical Engineering*, 2006, 2710-2713.
- [24] Ch. Hafner. Post-modern electromagnetics: Using intelligent MaXwell solvers, John Wiley & Sons Ltd, Chichester, 1999.
- [25] L. El Ghaoui. Inversion error, condition number and approximate inverses of uncertain matrices, *Linear Algebra and its Applications*, 343-344 (2002) 171-193.
- [26] E. Bajalinov and A. Rácz. Scaling problems in linear-fractional programming, 28<sup>th</sup> International Conference on Information Technology Interfaces ITI 2006, June 19-22, 2006, Cavtat, Croatia, pp. 495-499.
- [27] D. R. Fulkerson and P. Wolfe. An algorithm for scaling matrices, *SIAM Review*, 4 (1962) 142-146.
- [28] A. R. Curtis and J. K. Reid. On the automatic scaling of matrices for Gaussian elimination, *Journal of the Institute of Mathematics and its Applications*, 10 (1972) 118-124.
- [29] G. H. Golub and J. M. Varah. On a characterization of the best L2-scaling of a matrix, *SIAM Journal on Numerical Analysis*, 11 (1974) 472-479.
- [30] F. L. Bauer. Optimally scaled matrices, *Numerische Mathematik*, 5 (1963) 73-87.
- [31] P. A. Businger. Matrices which can be optimally scaled, *Numerische Mathematik*, 12 (1968) 346-348.
- [32] R. Braatz and M. Morari. Minimizing the Euclidean condition number, *SIAM Journal on Control and Optimization*, 32 (1994) 1763-1768.
- [33] C. McCarthy and G. Strang. Optimal conditioning of matrices, *SIAM Journal on Numerical Analysis*, 10 (1973) 370-388.
- [34] G. A. Watson. An algorithm for optimal 2 scaling of matrices, *IMA Journal of Numerical Analysis*, 11 (1991) 481-492.
- [35] S. M. Rump. Optimal scaling for P-norms and componentwise distance to singularity, *IMA Journal of Numerical Analysis*, 23 (2003) 1-9.

- [36] G. Golub and C. Van Loan. Matrix Computations, 2<sup>nd</sup> edition, Johns Hopkins U. P., Baltimore, 1989.
- [37] G. W. Stewart. Introduction to matrix computations, Academic, New York, 1973.
- [38] G. Poole and L. Neal. Gaussian Elimination: When is scaling beneficial?, *Linear Algebra and its Applications*, 162-164 (1992) 309-324.
- [39] R. D. Skeel. Scaling for numerical stability in Gaussian elimination, *Journal of the Association for Computing Machinery*, 26 (1979) 494-526.
- [40] R. D. Skeel. Effect of equilibration on residual size for partial pivoting, *SIAM Journal on Numerical Analysis*, 18 (1981) 449-454.
- [41] G. Poole and L. Neal. A geometric analysis of Gaussian elimination, *Linear Algebra and its Applications*, 149 (1991) 249-272.
- [42] G. Forsythe and C. Moler. Computer solution of linear algebraic systems, Prentice-Hall, Englewood Cliffs, 1967.
- [43] J. R. Bunch. Equilibration of symmetric matrices in the max-norm, *Journal of the Association for Computing Machinery*, 18 (1971) 566-572.
- [44] J. W. Demmel. On condition numbers and the distance to the nearest ill-posed problem, *Numerische Mathematic*, 51 (1987) 251-289.
- [45] J. Chehab and M. Raydan. Geometrical properties of the Frobenius condition number for positive definite matrices, *Linear Algebra and its Applications*, 429 (2008) 2089-2097.
- [46] P. Tarazaga. Eigenvalue estimates for symmetric matrices, *Linear Algebra and its Applications*, 135 (1990) 171-179.
- [47] J. Demmel and N. Higham. Improved error bounds for underdetermined system solvers, *SIAM Journal on Matrix Analysis and Applications*, 14 (1993) 1-14.
- [48] R. W. Hamming. Introduction to applied numerical analysis, McGraw-Hill, New York, 1971.
- [49] C. B. Moler. Matrix computations with FORTRAN and paging, *Communications of the ACM* 15 (1972) 268-270.
- [50] R. Eichardt, D. Baumgarten, B. Petković, F. Wiekhorst, L. Trahms and J. Haueisen. Adapting source grid parameters to improve the condition of the magnetostatic linear inverse problem of estimating nanoparticle distributions, *Medical and Biological Engineering and Computing*, 50 (2012) 1081-1089.
- [51] M. Nalbach and O. Dössel. Comparison of sensor arrangements of MCG and ECG with respect to information content, *Physica C*, 372-376 (2002) 254-258.
- [52] E. Izquierdo and V. Guerra. Estimating the essential matrix by efficient linear techniques, *IEEE Transactions on Circuits and Systems for Video Technology*, 13 (2003) 925-935.
- [53] A. Björck. Numerical methods for least squares problems, in SIAM, Philadelphia, 1996.
- [54] P. Sabatier. On geophysical inverse problems and constraints, *Journal of Geophysics*, 43 (1977) 115-137.
- [55] C. Chiang and J. Chandler. An approximate equation for the condition numbers of well-scaled matrices, *Proceedings of the IAJC-IJME International Conference*, paper 036, 2008.
- [56] J. Martinez. A bound for the Moore-Penrose pseudoinverse of a matrix, *Commentationes Mathematicae Universitatis Carolinae*, 20 (1979) 357-360.
- [57] S. Chandrasekaran and I. Ipsen. Perturbation theory for the solution of systems of linear equations, Research Report YALEU/DCS/RR-866, October, 1991.

- [58] G. W. Stewart. Collinearity and least squares regression, *Statistical Science*, 2 (1987) 68-100.
- [59] B. Petković, R. Eichardt, D. Baumgarten, U. Graichen, J. Haueisen and L. Di Rienzo. Comparison of figures of merit in linear inverse problems, *International Journal of Bioelectromagnetism*, 14 (2012) 46-50.
- [60] B. Petkovic, R. Eichardt, D. Baumgarten, U. Graichen, J. Haueisen and L. Di Rienzo. Comparison of figures of merit in linear inverse problems, 8th International Symposium on Noninvasive Functional Source Imaging of the Brain and Heart and the 8th International Conference on Bioelectromagnetism - NFSI and ICBEM 2011, Banff, Alberta, Canada, CD Proceedings.
- [61] M. Hermann. *Numerische Mathematik*, Oldenbourg Wissenschaftsverlag, 2001.
- [62] M. T. Heath, A. J. Laub, C. C. Paige and R. C. Ward. Computing the singular value decomposition of a product of two matrices, *SIAM Journal on Scientific and Statistical Computing*, 7 (1986) 1147-1159.
- [63] E. G. Kogbetliantz. Solution of linear equations by diagonalization of coefficients matrix, *Quarterly of Applied Mathematics*, 13 (1995) 123-132.
- [64] B. De Moor. On the structure and geometry of the product singular value decomposition, *Linear Algebra and its Applications*, 168 (1992) 95-136.
- [65] A. George and K. D. Ikramov. Gaussian elimination is stable for the inverse of a diagonally dominant matrix, *Mathematics of Computation*, 73 (2007) 653-657.
- [66] Q. Ye. Computing singular values of diagonally dominant matrices to high relative accuracy, *Mathematics of Computation*, 77 (2008) 2195-2230.
- [67] N. J. Higham. *Accuracy and stability of numerical algorithms*, SIAM, Philadelphia, 1996.
- [68] H. Weyl. Das asymptotische Verteilungsgesetz der Eigenwert linearer partieller Differentialgleichungen, *Mathematische Annalen*, 71 (1912) 441-479.
- [69] R. A. Horn and C. R. Johnson. *Topics in atrix analysis*, Cambridge University Press, 1991.
- [70] G. Di Lena, R. I. Peluso and G. Piazza. Results on the relative perturbation of the singular values of a matrix, *BIT* 33 (1993) 647-653.
- [71] L. Mirsky. Symmetric gage functions and unitarily invariant norms, *Quarterly Journal of Mathematics*, 11 (1960) 50-59.
- [72] G. W. Stewart. A note on the perturbation of singular values, *Linear Algebra and its Applications*, 28 (1979) 213-216.
- [73] D. S. Bernstein. *Matrix Mathematics*, second ed., Princeton University Press, New Jersey, 2009.
- [74] C. Lawson and R. Hanson. *Solving least squares problems*, SIAM, Society for Industrial and Applied Mathematics, 1995.
- [75] A. Dax. On extremum properties of orthogonal quotients matrices, *Linear Algebra and its Applications*, 432 (2010) 1234-1257.
- [76] L. Trefethen and D. Bau. *Numerical linear algebra*, Society for Industrial and Applied Mathematics, Philadelphia, ISBN 978-0-89871-487-6, 2000.
- [77] M. Hämäläinen, R. Hari, R. J. Ilmoniemi, J. Knuutila and O. V. Lounasmaa. Magnetoencephalography – theory, instrumentation, and applications to noninvasive studies of the working human brain, *Reviews of Modern Physics*, 65 (1993) 413–497.
- [78] P. Hansen, M. Kringelbach and R. Salmelin. *MEG: an Introduction to Methods*, Oxford University Press, 2010.

- [79] W. Andrä and H. Nowak. Magnetism in Medicine, Wiley-VCH Verlag GmbH & Co. KGaA, Weinheim, 2007.
- [80] T. H. Sander, J. Preusser, R. Mhaskar, J. Kitching, L. Trahms and S. Knappe. Magnetoencephalography with a chip-scale atomic magnetometer, *Biomedical Optics Express*, 3 (2012) 981-990.
- [81] R. L. Lux, C. R. Smith, R. F. Wyatt and J. A. Abildskov. Limited lead selection for estimation of body-surface potential maps in electrocardiography, *IEEE Transactions on Biomedical Engineering*, 25 (1978) 270–276.
- [82] R. C. Barr, M. S. Spach and S. Herman-Giddens. Selection of the number and position of measuring locations for electrocardiography, *IEEE Transactions on Biomedical Engineering*, 18 (1971) 125–138.
- [83] D. D. Finlay, C. D. Nugent, M. P. Donnelly, R. L. Lux, P. J. McCullagh and N. D. Black. Selection of optimal recording sites for limited lead body surface potential mapping: A sequential selection based approach, *BMC Medical Informatics and Decision Making*, 6 (2006).
- [84] V. Jazbinšek, R. Hren and Z. Trontelj. Influence of limited lead selection on source localization in magnetocardiography and electrocardiography, *International Congress Series*, 1300 (2007) 492-495.
- [85] K. Kim, Y. H. Lee, H. Kwon, J.M. Kim, I. S. Kim, and Y. K. Park. Optimal sensor distribution for measuring the tangential field components in MCG, *Neurology and Clinical Neurophysiology*, 60 (2004).
- [86] L. Di Rienzo, J. Haueisen and C. M. Arturi. Three component magnetic field data: Impact on minimum norm solutions in a biomedical application, *COMPEL: International Journal for Computation and Mathematics in Electrical and Electronic Engineering*, 24 (2005) 869–881.
- [87] C. M. Arturi, L. D. Rienzo and J. Haueisen. Information content in single-component versus three-component cardiomagnetic fields, *IEEE Transactions on Magnetics*, 40 (2004) 631–634.
- [88] B. Petković, S. Lau, L. Di Rienzo and J. Haueisen. Comparison of figures of merit in the optimization of vest-like sensor arrangements for magnetocardiography, *7th International Workshop on Biosignal Interpretation, BSI 2012*, July 2-4, 2012, Como, Italy.
- [89] S. Lau, B. Petković, L. Di Rienzo and J. Haueisen, Optimizing a magnetic sensor vest for cardiac source imaging, *18th International Conference on Biomagnetism*, August 26-30, 2012, Paris, France, pp. 115-116.
- [90] S. Lau, B. Petković, L. Di Rienzo and J. Haueisen. Optimizing a magnetic sensor vest for cardiac source imaging, *46th DGBMT Annual Conference BMT 2012*, Jena, Germany, September 16-19, 2012.
- [91] B. Petković, S. Lau, J. Haueisen and L. Di Rienzo. Comparison of figures of merit for the optimization of sensor setups in magnetocardiography, *12th International Workshop on optimization and inverse problems in Electromagnetism*, September 19-21, 2012, Ghent, Belgium, pp. 120-121.
- [92] J. Haueisen, J. Schreiber, H. Brauer and T. R. Knösche. Dependence of the inverse solution accuracy in magnetocardiography on the boundary-element discretization, *IEEE Transactions on Magnetics*, 38 (2002) 1045–1048.
- [93] R. D. Pascual-Marqui, C.M. Michel and D. Lehmann. Low-resolution electromagnetic tomography - a new method for localizing electrical activity in the brain, *International Journal of Psychophysiology*, 18 (1994) 49–65.

- [94] A. D. Pascual-Marqui. Standardized low resolution brain electromagnetic tomography (sLORETA): Technical details, *Methods and Findings in Experimental and Clinical Pharmacology*, 24 (2002) 5–12.
- [95] S. Lau. Strategies for optimal design of biomagnetic sensor systems, Diploma thesis, 2007.
- [96] D. Budker and M. Romalis. Optical magnetometry, *Nature*, 3 (2007) 227–234.
- [97] J. Kennedy, R. C. Eberhart and S. Yuhui. *Swarm intelligence*, San Francisco: Morgan Kaufmann, 2001.
- [98] A. P. Engelbrecht,. *Fundamentals of swarm intelligence*, Chichester: Wiley, 2005.
- [99] SimBio Group. SimBio: A generic environment for bio-numerical simulations. online, <https://www.mrt.uni-jena.de/simbio>, accessed 15. May 2012.
- [100] L. Kaufman and P. J. Rousseeuw. Clustering by means of medoids, *Statistical data analysis based on the L1 norm*, Y. Dodge, Edition, North Holland/Elsevier, Amsterdam (1987) 405–416.
- [101] V. Jazbinšek, M. Burghoff, O. Kosch, U. Steinhoff, R. Hren, L. Trahms and Z. Trontelj. Selection of optimal recording sites in electrocardiography and magnetocardiography, NFSI Conference 2003, Chieti, Italy.
- [102] C. J. Hellier. *Handbook of nondestructive evaluation*, McGraw-Hill, 2003.
- [103] J. Achenbach. Quantitative non-destructive evaluation, *International Journal of Solids and Structures*, 37 (2000) 13-27.
- [104] T. Aastroem. From fifteen to two hundred NDT-Methods in fifty years, 17<sup>th</sup> World Conference on Nondestructive Testing, October 25-28, Shanghai, China, 2008.
- [105] D. C. Jiles. Review of magnetic methods for nondestructive evaluation, *NDT International*, 21 (1988) 311-319.
- [106] D. C. Jiles. Review of magnetic methods for nondestructive evaluation (Part 2), *NDT International*, 23 (1990) 83-92.
- [107] X. Ma. Electromagnetic NDT and condition monitoring - A personal view, 17th International Conference on Automation & Computing, ICAC 2011, Huddersfield, United Kingdom, (2011) 266-271.
- [108] R. Grimberg. Electromagnetic nondestructive evaluation: present and future, *Strojniški vestnik - Journal of Mechanical Engineering*, 57 (2011) 204-217.
- [109] G. Mook, F. Michel and J. Simonin. Electromagnetic imaging using probe arrays, *Strojniški vestnik - Journal of Mechanical Engineering*, 3 (2011) 227-236.
- [110] M. K. Lim and H. Cao. Combining multiple NDT methods to improve testing effectiveness, *Construction and Building Materials*, (2011), 1–6.
- [111] T. Heckel, H.-M. Thomas, M. Kreutzbruck and S. Ruehe. High speed non-destructive rail testing with advanced ultrasound and eddy current testing techniques, *National Seminar & Exhibition on Non-Destructive Testing (NDE 2009)*, (2009), 261-265.
- [112] J. Hauelsen, R. Unger, T. Beuker and M. E. Bellemann. Evaluation of inverse algorithms in the analysis of magnetic flux leakage data, *IEEE Transactions on Magnetics*, 38 (2002) 1481-1488.
- [113] A. Thess, E. V. Votyakov and Y. Kolesnikov. Lorentz force velocimetry, *Physical Review Letters*, 96 (2006) 164501.
- [114] M. Ziolkowski and H. Brauer. Fast computation technique of forces acting on moving permanent magnet, *IEEE Transactions on Magnetics*, 46 (2010) 2927-2930.



- [115] R. J. Hanson. A numerical method for solving Fredholm integral equations of the first kind using singular values, *SIAM Journal on Numerical Analysis*, 8 (1971) 616-622.
- [116] P. Xu. Truncated SVD methods for discrete linear ill-posed problems, *Geophysical Journal International*, 135 (1998) 505-514.
- [117] P. C. Hansen and D. P. O’Leary DP. The use of the L-curve in the regularization of discrete ill-posed problems, *SIAM Journal on Scientific Computing* 14 (1993) 1487-1503.
- [118] M. Zec, R. P. Uhlig, M. Ziolkowski and H. Brauer. Lorentz force eddy current testing: Modelling of permanent magnets in dynamic simulation using logical expressions, *IET 8th International Conference on Computation in Electromagnetics (CEM 2011)*, (2011) 1-2.
- [119] C. Emson and J. Simkin. An optimal method for 3-D eddy currents, *IEEE Transactions on Magnetics*, 19 (1983) 2450-2452.
- [120] Mehrachsen-Kraftsensor K3D40Th. <http://www.me-systeme.de/de/datasheets/k3d40.pdf>, downloaded 2012-07-10.
- [121] R. P. Uhlig, M. Zec, M. Ziolkowski, M. Brauer, H. and A. Thess. A Lorentz force sigmometry: a contactless method for electrical conductivity measurements, *Journal of Applied Physics*, 111 (2012) 094914-1 - 094914-7.

---

## List of figures

2.1 Left Riemann summation method in calculation the area under the curve of normalized singular values of a kernel matrix .....	16
2.2 Dependence of normalized measures of conditioning of a kernel matrix.....	20
2.3 Representation of normalized magnetic moments of dipoles in an assumed dipole grid, obtained by using an array of $n = 144$ sensors (a) and $n = 75$ sensors (b), color-coded using the color scale (c). Simulated dipole is placed at point (0.12 m, 0.12 m) .....	21
2.4 Classification of figures of merit.....	23
3.1 Mean values of $\Delta CN$ in logarithmic representation obtained in 100 runs (a) and $\Delta \sigma_{\max}$ and $\Delta \sigma_{\min}$ in blue and red respectively (b) for different angles of single-axis sensor directions variations about the $z$ axis .....	34
3.2 Representation of perturbation expansion (3.40) in the $\varepsilon$ – $\eta$ coordinate system. The area where we can expect the increment of the smallest singular value is hatched.....	34
3.3 The case of increasing the smallest singular value with the probability equal to one, when $\inf((I - P) \cdot E) \leq \ P \cdot E\ $ .....	35
3.4 Case of increasing the smallest singular value with the probability equal to one, in case of $\inf((I - P) \cdot E) \geq \ P \cdot E\ $ .....	36
3.5 Representation of perturbation expansion (3.40) in the $\varepsilon$ – $\eta$ coordinate system.....	37
4.1 Dipole model consisting of 13 dipoles around the left ventricle. Orientations are fitted with minimum norm, L-curve regularization and sLORETA noise normalization. The figure is taken from [95].....	47
4.2 Current density distribution at the R-peak using the 13 dipoles model presented in Fig. 4.1 The figure is taken from [95].....	48
4.3 Search sensor space containing 19759 positions on the vest. Connections to arms, neck and lower body are omitted.....	48
4.4 Rejected sensors positions: at the lower part of the torso, around neck and around left and right shoulder. These positions are marked in red.....	50

4.5 Representative orientation vector of the cluster (marked by red arrow) is chosen as the most frequent orientation within a cluster (a). Orientations are colored using a scale (b)..	51
4.6 Color-coded sensor clusters for the 21 sensors array displayed on the triangulated torso for the <i>CN</i> from the front (a) and from the back (b).....	52
4.7 Color-coded sensor clusters for the 21 sensors array displayed on the triangulated torso for the <i>Skeel</i> from the front (a) and from the back (b).....	52
4.8 Color-coded sensor clusters for the 21 sensors array displayed on the triangulated torso for the $\rho$ from the front (a) and from the back (b).....	53
4.9 Color-coded sensor clusters for the 21 sensors array displayed on the triangulated torso for the $\xi$ from the front (a) and from the back (b).....	53
4.10 Color-coded sensor clusters for the 32 sensors array displayed on the triangulated torso for the <i>CN</i> from the front (a) and from the back (b).....	54
4.11 Color-coded sensor clusters for the 32 sensors array displayed on the triangulated torso for the <i>Skeel</i> from the front (a) and from the back (b).....	54
4.12 Color-coded sensor clusters for the 32 sensors array displayed on the triangulated torso for the $\rho$ from the front (a) and from the back (b).....	55
4.13 Color-coded sensor clusters for the 32 sensors array displayed on the triangulated torso for the $\xi$ from the front (a) and from the back (b).....	55
4.14 Optimized 21 sensors set-up obtained minimizing the <i>CN</i> from the front (a) and from the back (b).....	56
4.15 Optimized 21 sensors set-up obtained minimizing the <i>Skeel</i> from the front (a) and from the back (b).....	56
4.16 Optimized 21 sensors set-up obtained minimizing the $\rho$ from the front (a) and from the back (b).....	57
4.17 Optimized 21 sensors set-up obtained minimizing the $\xi$ from the front (a) and from the back (b).....	57
4.18 Optimized 32 sensors set-up obtained minimizing the <i>CN</i> from the front (a) and from the back (b).....	57
4.19 Optimized 32 sensors set-up obtained minimizing the <i>Skeel</i> from the front (a) and from the back (b). ....	58
4.20 Optimized 32 sensors set-up obtained minimizing the $\rho$ from the front (a) and from the back (b). ....	58
4.21 Optimized 32 sensors set-up obtained minimizing the $\xi$ from the front (a) and from the back (b). ....	58

4.22 Number of sensors versus distance to their cluster medoid for 21 sensor array for $CN$ , $Skeel$ , $\rho$ and $\xi$ .....	60
4.23 Number of sensors versus distance to their cluster medoid for 32 sensor array for $CN$ , $Skeel$ , $\rho$ and $\xi$ .....	61
4.24 Values of $CN$ , $Skeel$ , $\rho$ and $\xi$ obtained after minimization applying particle swarm optimization for 21 sensors setup (a) and 32 sensors setup (b).....	63
5.1 The laminated conductive bar - a package of thin Aluminum sheets moving with constant velocity below the permanent magnet together with a long and a wide defect used in the analysis.....	66
5.2 Modeling of DRS with a set of voxels with current dipoles (approximation method)....	67
5.3 The region of interest – a set of volumetric elements (voxels) where the defect reconstruction algorithm is applied.....	69
5.4 Implementation of the moving defect approach. $\Delta x$ is the mesh size in the moving direction, and $\Delta t$ is the simulation time step.....	73
5.5 The experimental setup, comprised of a linear belt-driven drive, a multi-component force sensor, a package of Al-sheets, a y-z-positioning stage and a data acquisition unit (not shown) (a). The package of Al-sheets in the vicinity of the permanent magnet (NdFeB, Ø15mm×25 mm) attached to the multi-component force sensor (b).....	74
5.6 The scanning area $\delta z = 1\text{mm}$ above the specimen without a defect and containing a long subsurface defect.....	75
5.7 Scanning area at 10 mm above the conductive specimen for the long crack (a) and wide crack (b). Each dot represents one force calculation point.....	75
5.8 The distributions of the normalized subtraction of the Lorentz forces in the case of long inner defect predicted by our approximation method (blue line) and computed in COMSOL (red line) of its $x$ component on the line $y = 0$ of the scanning plane (a), $y$ component on the line $y = -1\text{mm}$ of the scanning plane (b) and $z$ component on the line $y = 0$ of the scanning plane (c).....	76
5.9 Simulation I - distributions of reference ( $\Delta F_\alpha$ ) and approximated ( $\tilde{F}_\alpha$ ) normalized defect response signals evoked by the long subsurface defect.....	77
5.10 The The distributions of the normalized subtraction of the Lorentz forces in the case of wide inner defect predicted by our approximation method (blue line) and computed in COMSOL (red line) of its $x$ component on the line $y = 0$ of the scanning plane (a), $y$ component on the line $y = -1\text{mm}$ of the scanning plane (b) and $z$ component on the line $y = 0$ of the scanning plane (c).....	78
5.11 Simulation II - distributions of reference ( $\Delta F_\alpha$ ) and approximated ( $\tilde{F}_\alpha$ ) normalized defect response signals evoked by the wide subsurface defect.....	79

5.12 <i>Step I</i> – plane $x - z$ , distribution $\{\sigma_{50}\}$ of normalized conductivities for the long subsurface defect (conductivity threshold $Th = 50\%$ ), spurious solution (a), filtered solution (b). Normalized conductivities are color-coded using the color scale (c).....	80
5.13 <i>Step II</i> – distribution $\{\sigma_{50}\}$ of reconstructed normalized conductivities for the long subsurface defect along $x$ – line at $z_i = -2.78$ mm . The real defect is indicated as a black line segment.....	81
5.14 <i>Step III</i> – plane $x - y$ , distribution $\{\sigma_{50}\}$ of reconstructed normalized conductivities for the long defect at $z_i = -2.78$ mm . The real defect is marked with the black rectangle outline.....	81
5.15 <i>Step I</i> – plane $x - z$ , distribution $Th = 50\%$ of color-coded reconstructed normalized conductivities for the wide defect - filtered solution .....	82
5.16 <i>Step II</i> – distribution $\{\sigma_{50}\}$ of reconstructed normalized conductivities for the wide defect along $x$ – line at $z_i = -2.11$ mm . The real defect is indicated as a black line segment.....	82
5.17 <i>Step III</i> – plane $x - y$ , distribution $\{\sigma_{50}\}$ of reconstructed normalized conductivities for the wide defect at $z_i = -2.11$ mm . The real defect is marked with the black rectangle outline.....	83
5.18 <i>Step I</i> – plane $x - z$ , distribution $\{\sigma_{85}\}$ of color-coded normalized conductivities representing the long defect reconstructed from the measurement data - filtered solution.....	84
5.19 <i>Step II</i> – distribution $\{\sigma_{85}\}$ of reconstructed normalized conductivities for the long defect along $x$ – line at $z_i = -3.0$ mm (measurement data). The real defect is indicated as a black line segment.....	84
5.20 <i>Step III</i> – plane $x - y$ , distribution $\{\sigma_{85}\}$ of reconstructed normalized conductivities for the long defect at $z_i = -3.0$ mm (measurement data). The real defect is marked with the black rectangle.....	85

**List of tables**

4.1 Number of excluded sensors as belonging to the edge of the vest, number of different locations and percentage of the vest area covered by sensors for 21 sensor setup and different figures of merit.....	59
4.2 Number of excluded sensors as belonging to the edge of the vest, number of different locations and percentage of the vest area covered by sensors for 32 sensor setup and different figures of merit.....	60
4.3 Median and maximal distance between sensor cluster medoids and single sensors for 21 sensor setup and different figures of merit.....	60
4.4 Median and maximal distance between sensor cluster medoids and single sensors for 32 sensor setup and different figures of merit.....	61
4.5 Mean values and standard deviations of values of $CN$ , $Skeel$ , $\rho$ and $\xi$ for 21 and 32 sensors setups.....	62





---

## Erklärung

Ich versichere, dass ich die vorliegende Arbeit ohne unzulässige Hilfe Dritter und ohne Benutzung anderer als der angegebenen Hilfsmittel angefertigt habe. Die aus anderen Quellen direkt oder indirekt übernommenen Daten und Konzepte sind unter Angabe der Quelle gekennzeichnet.

Bei der Auswahl und Auswertung folgenden Materials haben mir die nachstehend aufgeführten Personen in der jeweils beschriebenen Weise unentgeltlich geholfen:

1. Dipl.-Inf. Stephan Lau → Die Implementierung verschiedener Bewertungsmaße ist eine Erweiterung von Stephans Software für die Optimierung der Magnetsensoren rund um den Oberkörper [95, *Strategies for optimal design of biomagnetic sensor systems*, Diplomarbeit, 2007]. Die Analyse der Ergebnisse wurde mit meiner eigenen Software durchgeführt (Abschnitte 4.2.2-4.2.5). Die Ergebnisse sind in gemeinschaftlich erarbeiteten Vorträgen veröffentlicht [88-91] und in dieser Doktorarbeit dargestellt (Abschnitt 4.3).

Weitere Personen waren an der inhaltlich-materiellen Erstellung der vorliegenden Arbeit nicht beteiligt. Insbesondere habe ich hierfür nicht die entgeltliche Hilfe von Vermittlungs- bzw. Beratungsdiensten (Promotionsberater oder anderer Personen) in Anspruch genommen. Niemand hat von mir unmittelbar oder mittelbar geldwerte Leistungen für Arbeiten erhalten, die im Zusammenhang mit dem Inhalte der vorgelegten Dissertation stehen.

Die Arbeit wurde bisher weder im In- noch im Ausland in gleicher oder ähnlicher Form einer Prüfungsbehörde vorgelegt.

Ich bin darauf hingewiesen worden, dass die Unrichtigkeit der vorstehenden Erklärung als Täuschungsversuch angesehen wird und den erfolglosen Abbruch des Promotionsverfahrens zu Folge hat.

Ilmenau, 30.04.2013

---

Bojana Petković

